

EFFECT OF WATER-FILLED CHAMBER ON SHAPED CHARGE JET  
PENETRATION

A THESIS SUBMITTED TO  
THE GRADUATE SCHOOL OF NATURAL AND APPLIED SCIENCES  
OF  
MIDDLE EAST TECHNICAL UNIVERSITY



BY  
FUAT GÜLYAŞAR

IN PARTIAL FULFILLMENT OF THE REQUIREMENTS  
FOR  
THE DEGREE OF DOCTOR OF PHILOSOPHY  
IN  
MECHANICAL ENGINEERING

SEPTEMBER 2024



Approval of the thesis:

**EFFECT OF WATER-FILLED CHAMBER ON SHAPED CHARGE JET  
PENETRATION**

submitted by **FUAT GÜLYAŞAR** in partial fulfillment of the requirements for the degree of **Doctor of Philosophy in Mechanical Engineering, Middle East Technical University** by,

Prof. Dr. Naci Emre Altun  
Dean, **Graduate School of Natural and Applied Sciences**

Prof. Dr. Serkan Dağ  
Head of the Department, **Mechanical Engineering**

Prof. Dr. R. Orhan Yıldırım  
Supervisor, **Mechanical Engineering, METU**

**Examining Committee Members:**

Prof. Dr. Hüsnü Dal  
Mechanical Engineering, METU

Prof. Dr. R. Orhan Yıldırım  
Mechanical Engineering, METU

Prof. Dr. S. Kemal İder  
Mechanical Engineering, Çankaya University

Assoc. Prof. Dr. Mehmet Nurullah Balcı  
Mechanical Engineering, Hacettepe University

Assist. Prof. Dr. Orkun Özşahin  
Mechanical Engineering, METU

Date: 05.09.2024



**I hereby declare that all information in this document has been obtained and presented in accordance with academic rules and ethical conduct. I also declare that, as required by these rules and conduct, I have fully cited and referenced all material and results that are not original to this work.**

Name, Last name : Fuat Gülyaşar

Signature :

## ABSTRACT

### EFFECT OF WATER-FILLED CHAMBER ON SHAPED CHARGE JET PENETRATION

Gülyaşar, Fuat  
Doctor of Philosophy, Mechanical Engineering  
Supervisor : Prof. Dr. R. Orhan Yıldırım

September 2024, 124 pages

In this study, the protective capability of the water-filled cylindrical chamber against shaped charge ammunition is evaluated. The effects of the chamber parameters, such as the diameter, length, and sidewall thickness, on the penetration depth in the witness plate placed behind this chamber are investigated. The numerical FEM analyses that utilize 2D Axisymmetric Multi-Material Arbitrary Lagrangian Eulerian (ALE) method are conducted using LS-DYNA software. The stability and the particulation of the copper jet affect its penetration to steel targets. Using these analyses, the mechanism that causes the instability and the particulation of the jet while it passes through the water-filled chambers with different parameters is visually demonstrated and explained. Furthermore, tests are conducted using the critical chamber parameters that are obtained from the analyses to verify the results.

Keywords: Shaped Charge Jet, Water-Filled Structure Armor, Jet Stability, 2D Axisymmetric Multi-Material Arbitrary Lagrangian Eulerian (ALE) Algorithm

## ÖZ

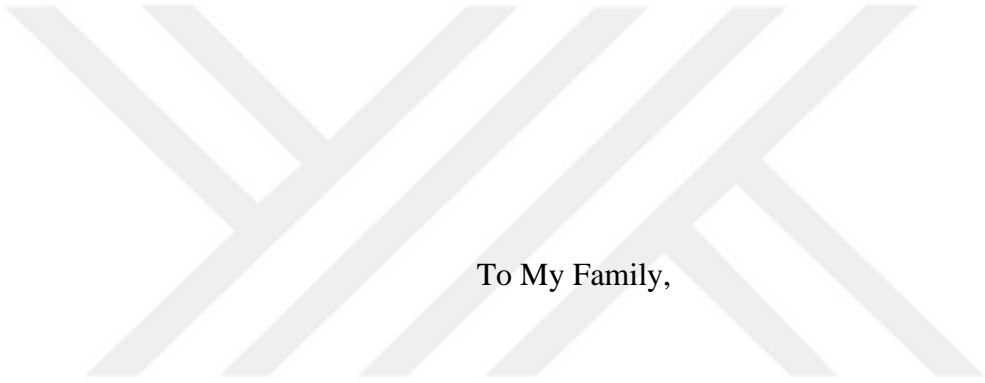
### İÇİ SU DOLU YAPILARIN ÇUKUR İMLA MÜHİMMATININ DELME DERİNLİĞİNE ETKİSİ

Gülyaşar, Fuat  
Doktora, Makina Mühendisliği  
Tez Yöneticisi: Prof. Dr. R. Orhan Yıldırım

Eylül 2024, 124 sayfa

Bu çalışmada, içi su dolu silindirik bir odanın çukur imla mühimmatına karşı koruma etkileri incelenmiştir. Bu odanın uzunluğu, çapı, duvar kalınlığı gibi parametrelerinin, hemen arkasında bulunan çelik plakadaki delme derinliğine etkileri araştırılmıştır. LS-DYNA yazılımında bulunan iki boyutlu, aksenal simetrik, çok malzemeli ALE metodu kullanılarak çarpma olayının nümerik analizi yapılmıştır. Çukur imla jetindeki kararsızlık nedeniyle meydana gelen parçalanmaların jetin çelik plakaları delmesine olumsuz etki yarattığı bilinmektedir. Bu analizler kullanılarak farklı parametrelerin, odalardan geçen jetin kararlılığını nasıl etkilediği görsel olarak gösterilip açıklanmıştır. Ayrıca, sonuçları doğrulamak için, analizlerden elde edilen kritik parametrelere göre boyutlandırılan su dolu odalar imal edilmiş ve gerçek çukur imla mühimmatları ile testleri yapılmıştır.

Anahtar Kelimeler: Çukur İmla Mühimmatı, İçi Su Dolu Zırh, Jet Kararlılığı, ALE Metodu



To My Family,

## ACKNOWLEDGMENTS

I would like to express my deepest appreciation to my supervisor, Prof. Dr. R. Orhan Yıldırım, for his valuable contributions to this research.

The experimental survey of this research was conducted with the cooperation of Mechanical and Chemical Industry Corporation (MKE) Barutçular ve Patlayıcılar Fabrikası. Special thanks to the company and all staff and members who spent their time and effort in planning and conducting the experiments.

I also have to thank my family for their support throughout my education.

## TABLE OF CONTENTS

ABSTRACT.....	v
ÖZ .....	vi
ACKNOWLEDGMENTS .....	viii
TABLE OF CONTENTS.....	ix
LIST OF TABLES .....	xii
LIST OF FIGURES .....	xiii
LIST OF ABBREVIATIONS .....	xviii
LIST OF SYMBOLS .....	xix
CHAPTERS	
1 INTRODUCTION.....	1
1.1 The Shaped Charge Concept .....	1
1.2 Shaped Charge Jet Formation .....	8
1.3 Shaped Charge Jet Penetration Models .....	14
2 LITERATURE SURVEY ON COMPUTER SIMULATION OF SHAPED CHARGE JET FORMATION AND PENETRATION .....	21
2.1 Finite Element Method, Lagrangian, Eulerian, and Arbitrary Lagrangian Eulerian (ALE) Descriptions .....	21
2.2 Smoothed Particle Hydrodynamics .....	29
2.3 Equation of State and Material Models .....	31
2.3.1 Equation of State .....	31
2.3.2 Material Models .....	36
3 LITERATURE REVIEW ON ADD-ON ARMOR SYSTEMS AND SCOPE OF THE RESEARCH .....	43

3.1	Conventional Add-on Armor Systems Used on Armored Vehicles: Explosive Reactive Armors and Non-Explosive Reactive Armors.....	43
3.2	The Mechanism of Jet Dispersion in the Liquid Filled Chamber.....	45
3.3	The Recent Research .....	46
3.4	The Scope of the Research.....	52
4	NUMERICAL ANALYSIS .....	55
4.1	The Geometry and the Parameters of the Shaped Charge .....	55
4.2	Modeling and Material Parameters .....	57
4.3	Simulation of Standalone Shaped Charge Jet Formation .....	64
5	TEST SETUP.....	67
5.1	The Design of the Test Setup.....	67
6	RESULTS AND EVALUATION .....	71
6.1	Effect of Chamber Diameter (D) on Depth of Penetration.....	72
6.2	Effect of Chamber Length (L) on Depth of Penetration.....	88
6.3	Effect of Sidewall Thickness ( $t_w$ ) on Depth of Penetration.....	93
7	CONCLUSIONS .....	99
7.1	Summary and Conclusions .....	99
7.2	Future Work.....	102
	REFERENCES .....	103
	APPENDICES .....	109
A.	The Photos of The Test Setups, Tested with Different Diameter Chambers.....	109
B.	The Photos of The Test Setups, Tested with Different Length Chambers	115
C.	The Photos of The Test Setups, Tested with Different Sidewall Thickness Chambers.....	119

D. The Photos of The Witness Targets, Tested with 64 mm Long Water-Free Chambers and without Chambers ..... 122



## LIST OF TABLES

Table 2.1 Comparisons of Lagrangian and Eulerian Methods [13] .....	26
Table 3.1 The Penetration Depths without Liquid Structure Armor [28] .....	47
Table 3.2 The Penetration Depths with Liquid-Structure Armor [28] .....	47
Table 3.3 The Penetration Depths at Different Impact Angles [29].....	50
Table 4.1 The Resultant DOP in the Witness Target with Different Element Sizes when $D=20$ mm, $L=64$ mm, and $t_w=5$ mm .....	60
Table 4.2 Mie-Gruneisen EOS Parameters of Copper Liner, Steel Casing, Upper and Lower Caps, Water, Chamber and Witness Plate [21], [39], [40] .....	62
Table 4.3 JWL EOS Parameters of RDX Explosive [41] .....	63
Table 4.4 Linear Polynomial EOS Parameters for the Air [21] .....	63
Table 4.5 Johnson Cook Flow Parameters of the Copper Liner, Steel Casing, Upper and Lower Caps, Chamber and Witness Plate [24], [42].....	64
Table 4.6 Johnson Cook Fracture Parameters of the Copper Liner, Chamber and Witness Plate [43] .....	64
Table 6.1 Effect of Chamber Diameter and Length on Penetration Depth Simulation Results .....	71
Table 6.2 Effect of Chamber Diameter and Length on Penetration Depth Test Results.....	72
Table 6.3 Effect of Sidewall Thickness on Penetration Depth when the Diameter (D) is 20 mm, and the Chamber Length (L) is 64 mm.....	93

## LIST OF FIGURES

Figure 1.1. The Lined Cavity Effect [2].....	2
Figure 1.2 Comparison of the Effects of Hollow Cavity (Lined & Unlined) Charges and No Cavity Charge (Flat End) on Steel Targets .....	2
Figure 1.3 The Schematic View and Components of a Shaped Charge [3], [4].....	3
Figure 1.4 The Nomenclature of the Dimensions of a Shaped Charge; CD: Charge Diameter, WD: Warhead Diameter, LD: Liner Diameter [1].....	3
Figure 1.5 The Collapse of Shaped Charge with a Conical Liner and Jet Formation [1], [5].....	5
Figure 1.6 Jet Penetration [1].....	5
Figure 1.7 M72 LAW, 66 mm Weapon System and Its Ammunition [6], [7].....	6
Figure 1.8 RPG-7 Antitank Ammunition and Schematic View of its Cross Section [7].....	7
Figure 1.9 Cutting Metal Pipes with a Flexible Linear Shaped Charge [8].....	7
Figure 1.10 Cutting Thick Block of Steel with a Linear Shaped Charge [9].....	7
Figure 1.11 Canopy Fracturing of a Military Aircraft with a Flexible Linear Shaped Charge for the Ejection of the Pilot Seat (RH Side), The Schematic View of the Linear Shaped Charge that is Installed on the Canopy Window (LH Side) [10] ...	8
Figure 1.12 Linear Velocity Distribution for the Open-Faced Sandwich Configuration [1] .....	9
Figure 1.13 Direction of Metal Projection by a Grazing Detonation Wave [1].....	10
Figure 1.14 Geometry of the Collapse Process (Birkoff et al. 1948) [1].....	11
Figure 1.15 The Collapse Process for a Variable Collapse Velocity Liner (Pugh et al. 1952) [1] .....	12
Figure 1.16 The Schematic Diagram Shows the Necking Instability of Shaped Charge Jets [1] .....	14
Figure 1.17 Jet Penetration [11].....	15

Figure 1.18 Jet Penetration with a Coordinate System Moving at the Penetration Velocity U [11] .....	15
Figure 1.19 Phase Diagram of Rod Penetration According to One-Dimensional Theory (Chou and Flis 1986) [11] .....	20
Figure 2.1 Deformation in Lagrangian System [1] .....	22
Figure 2.2 An Example of a Rezoned Calculation. (a)Mesh before Rezoning. (b)Mesh after Rezoning [1] .....	23
Figure 2.3 Penetration Calculation with Eroding Slide Lines at 25 $\mu$ s After Impact [1]. .....	24
Figure 2.4 Deformation in Eulerian System [1] .....	25
Figure 2.5 Examples of Lagrange, Euler, ALE and SPH Simulations [16]. .....	31
Figure 2.6 Johnson-Cook Models of Various Metals Derived from True Stress-True Strain Curves [24] .....	38
Figure 2.7 The Relationship between $\ln(\sigma - A)$ and $\ln \epsilon$ [25]. .....	39
Figure 2.8 The Relationship between $\frac{\sigma_y}{(A + B\epsilon^{p^n})}$ and $\ln \epsilon^*$ [25] .....	40
Figure 2.9 The Relationship between $\ln [1 - \frac{\sigma_y}{(A + B\epsilon^{p^n})}]$ and $\ln T^*$ [25] .....	41
Figure 3.1 The X-ray Pictures of the Shaped Charged Jet Disturbance by Explosive Reactive Armor at Different Impact Angles [27] .....	44
Figure 3.2 The Numerical Simulation of the Disturbance of the Shaped Charged Jet by Explosive Reactive Armor [23] .....	44
Figure 3.3 Steps of Penetration of the Shaped Charge Jet through a Liquid-Filled Structure [28] .....	45
Figure 3.4 The Design of the Liquid-Filled Structure Armor [24]. .....	46
Figure 3.5 The Schematic Representation of the Liquid-Filled Structure, Shaped Charge Jet Penetration Experiment [28] .....	47
Figure 3.6 The Schematic Representation of Liquid Filled Structure, Shaped Charge Jet Penetration Experiment [29] .....	48

Figure 3.7 The Schematic of the Propagation Path of the Shock Wave (LH Side), The Representation of Liquid-Filled Structure Shaped Charge Jet Penetration Experiment [29].	49
Figure 3.8 Penetration Channel Geometry of the Shaped Charge Jet Under Different Impact Angles [29]	50
Figure 3.9 Schematic View of Shock Wave Propagation in the Diesel Fuel (LH Side), Air-tight Diesel Fuel Filled Structure (Middle), Experimental Setup (RH Side) [30]	51
Figure 3.10 The Depth of Penetration – Chamber Radius Graph [30]	51
Figure 3.11 The Schematic View of the Experimental Setup	53
Figure 4.1 The Cross Section of M85 Bomblet [31]	55
Figure 4.2 The Simplified 3D Model Geometry of the Shaped Charge	56
Figure 4.3 The Dimensions of the Setup: The Munition is at the LH Side, the Water-filled Chamber is in the Middle, the Target is at the RH Side	57
Figure 4.4 2D Axisymmetric ALE FEM Model	58
Figure 4.5 Element Size vs DOP when $D=20$ mm, $L=64$ mm, and $t_w=5$ mm	60
Figure 4.6 The Formation of SC Jet; Copper is Shown in Red, Steel Casing and Target Material is Dark Grey, and Explosive/Detonation Products are Shown in Turquoise	65
Figure 4.7 The Velocity Gradient (m/s) of the Jet in Axial Direction; The Jet Tip Velocity Reaches up to 9.3 km/s	65
Figure 5.1 The Design of the Test Setup	68
Figure 5.2 Test Setups that Represent the Cases without Chamber (LH Side), with Chamber w/o Water (RH Side)	69
Figure 5.3 Test Setups with $\varnothing 50$ mm Diameter and 64 mm Length Chamber (LH Side), with $\varnothing 20$ mm Diameter and 64 mm Length Chamber (RH Side)	69
Figure 6.1 Depth of Penetration vs Diameter (D) Graph when the Chamber Length (L) is 64 mm and the Sidewall Thickness ( $t_w$ ) is 5 mm	73
Figure 6.2 Test Setups with $\varnothing 10, 20, 35, 50$ mm Diameter Chambers (LH Side Picture), $\varnothing 10$ Diameter, 15 mm Sidewall Chamber and a $\varnothing 70$ mm Diameter	

Chamber (RH Side Picture) from Left to Right, Respectively with a Standard 5 mm Sidewall Thickness (Except Mentioned) and 64 mm Length .....	74
Figure 6.3 Test Results with Different Diameters; $\varnothing$ 10 mm, 20 mm, 35 mm and 50 mm, the DOP of the Witness Targets (the Height of the Machined Targets from the Bottom) are 62 mm, 48 mm, 75.5 mm, 98 mm from Left to Right, Respectively .....	75
Figure 6.4 Test Results with Different Diameters; $\varnothing$ 10 mm (15 mm sidewall thickness), 20 mm, 50 mm and 70 mm, the DOP of the Witness Targets (the Height of the Machined Target from the Bottom) are 55 mm, 48 mm, 55.3 mm, 75 mm from Left to Right, Respectively .....	76
Figure 6.5 The Jet Velocity Distribution (m/s) and the Disturbances Created on Jets Leaving $D=43$ mm (Upper), $D=35$ mm (Middle) and $D=27$ mm (Lower) Chambers.....	78
Figure 6.6 Test Specimens and Witness Plates for $D=10$ mm Chamber Diameter, $t_w=5$ mm Sidewall Thickness (LH Side), $t_w=15$ mm (RH Side) .....	79
Figure 6.7 The Reflecting Pressure Waves (GPa) in Water at 27, 28 $\mu$ s after Detonation when the Chamber Diameters $D=50$ (Upper Figure), 20 mm (Lower Figure) .....	80
Figure 6.8 The Difference of Jet Particulations between 20 mm (Lower Figure) and 50 mm (Upper Figure) Diameter Chambers ( $L=64$ mm) at Instance $t=38\mu$ s after the Start of Detonation .....	81
Figure 6.9 The Difference of Pressure Distributions in Water between 20 mm (Upper Figure) and 10 mm (Middle and Lower Figure) Diameter Chambers at $t=24\mu$ s.....	83
Figure 6.10 The Difference of Pressure Distributions in Water between 20 mm (Upper Figure) and 10 mm (Middle and Lower Figure) Diameter Chambers at $t=24\mu$ s (Same as Figure 6.9. However, High Pressure Regions are Masked) .....	84
Figure 6.11 The Difference of Exit Holes between $D=10$ mm, $t_w=15$ mm (LH side Specimen in Each Picture) and $D=20$ mm, $t_w=5$ mm (RH Side Specimen in Each Picture) Diameter Chambers from two Different Angles .....	85

Figure 6.12 The Difference of Jet Tip Scatter after Leaving 20 mm (Upper Figure ) and 10 mm (Middle and Lower Figure) Diameter Chambers at $t=33\mu\text{s}$ .....	86
Figure 6.13 The Difference of Jet Particulation after Leaving 10 mm (Middle and Lower Figure ) and 20 mm (Upper Figure) Diameter Chambers at $t=36\mu\text{s}$ .....	87
Figure 6.14 The Depth of Penetration vs Length when the Diameter is 20 mm and Sidewall Thickness is 5 mm .....	89
Figure 6.15 Test Setups with Different Length Chambers; 32 mm, 48 mm and 88 mm from Left to Right, Respectively with a Standard 5 mm Sidewall Thickness and $\text{Ø}20$ mm Diameter .....	90
Figure 6.16 Test Results with Different Length Chambers; 32 mm, 48 mm, 64 mm and 88 mm, the DOP of the Witness Targets are 57 mm, 63 mm, 45 mm, 57,7 mm from Left to Right, Respectively .....	91
Figure 6.17 The Jet that is Leaving the Chamber of Different Lengths, $L= 64$ mm and 88 mm at $t=35\mu\text{s}$ .....	92
Figure 6.18 The Depth of Penetration vs Sidewall Thickness ( $D=20$ mm and $L=64$ mm).....	94
Figure 6.19 Test Setups with Different Sidewall Thickness Chambers; 1.5, 3, 7.5, and 10 mm from Left to Right, Respectively with a Standard 64 mm Length and $\text{Ø}20$ mm Diameter .....	94
Figure 6.20 Test Results with Different Sidewall Thickness Chambers; 1.5, 3, 5, 7.5, and 10 mm, the DOP of the Witness Targets are 83, 68, 54, 42.8, and 43 mm from Left to Right, Respectively .....	95
Figure 6.21 The Difference of Pressure Distributions (GPa) in Water between 1.5 mm (Upper Figure), 3 mm (Middle Figure), and 5 mm (Lower Figure) Sidewall Thicknesses at $t=28\mu\text{s}$ ( $D=20$ mm and $L=64$ mm) .....	97
Figure 6.22 The Difference of Jet Particulation and Disturbances between 1.5, 3 and 5 mm Sidewall Thicknesses at $t=33\mu\text{s}$ ( $D=20$ mm and $L=64$ mm).....	98

## LIST OF ABBREVIATIONS

ALE	:Arbitrary Lagrangian Eulerian
CD	:Charge Diameter
CAD	:Computer Aided Design
CFL	:Courant-Friedrichs-Lewy
DOP	:Depth of Penetration
EOS	:Equation of State
ERA	:Explosive Reactive Armor
FEM	:Finite Element Method
HEAT	:High Explosive Antitank Warhead
HE	:High Explosive
JWL	:Jones-Wilkins-Lee
LAW	:Lightweight Antitank Weapon
LD	:Liner Diameter
LH	:Left-Hand
MMALE	:Multi-Material Arbitrary Lagrangian Eulerian
NERA	:Non-explosive Reactive Armor
RH	:Right-Hand
RHA	:Rolled-Homogenous Armor
RDX	:Research Department Explosive or Royal Demolition Explosive
RTV2	:Room Temperature Vulcanizing Silicone (made of two components)
RPG	:Ruchnaya Protivotankovaya Granata; Hand-Held Antitank Grenade
SC	:Shaped Charge
SO	:Standoff
SPH	:Smoothed Particle Hydrodynamics
TSSFAC	:Time Step Scale Factor
WD	:Warhead Diameter
w/o	:Without

## LIST OF SYMBOLS

A	:JWL EOS material parameter
B	:JWL EOS material parameter
b	:First order volume correction to $\gamma_0$
$C_0$	:Speed of sound at given material
$C_{1,2,3,4,5,6}$	:Linear polynomial EOS parameters
D	:Chamber diameter
$D_{1,2,3,4,5}$	:Johnson-Cook fracture parameters
E	:Internal energy per unit mass at initial state
L	:Length of the liquid chamber
P	:Depth of penetration
$R_1$	:JWL EOS material parameter
S	:Standoff distance between chamber and munition
$S_1$	:Standoff distance between witness plate and munition
$S_{1,2,3}$	:Mie-Gruneisen EOS fitting parameters
$T^*$	:Relative temperature
$t_p$	:Upper plate thickness
$t_b$	:Bottom plate thickness
$t_w$	:Sidewall thickness
V	:Relative volume ( $V/V_0$ )
$\gamma$	:Gruneisen gamma, ratio of specific heats ( $c_p/c_v$ )
$\gamma_0$	:Gruneisen gamma at ambient conditions
$\epsilon$	:Internal energy per unit volume
$\rho$	:Density
$\rho_j$	:Jet density
$\rho_t$	:Target density
$\omega$	:JWL EOS material parameter

$\bar{\epsilon}^p$  :Effective plastic strain

$\dot{\epsilon}^*$  :Effective plastic strain rate



# CHAPTER 1

## INTRODUCTION

### 1.1 The Shaped Charge Concept

A cylinder of explosive with a hollow cavity at one end and a detonator at the other end is called a hollow charge (Figure 1.1a). The hollow cavity, which can be hemispherical or conical, directs the gaseous detonation products to concentrate their energy along the central axis opposite the cavity. This concentration of detonation products results in an intense, localized force. When this force is applied to a metal plate, it can produce a deeper cavity compared to a cylinder of explosive without a hollow cavity (Figure 1.2). This effect, known as the Munroe effect in the United States and the United Kingdom and the von Foerster or Neumann effect in Europe [1], is a fundamental principle in the design of shaped charge munitions.

The directional penetration effect is evident when a hollow charge is detonated in contact with a steel plate, as illustrated in Figure 1.1a. This effect is produced by the erosion caused by high-pressure, high-velocity gases. An advanced version of this concept, known as the lined charge, leads to a significantly deeper crater when the hollow cavity is lined with a thin metallic or glass cone, as shown in Figure 1.1b. Additionally, the penetration depth increases when the lined cavity charge is positioned at a distance from the target block, referred to as the standoff distance (SO), as depicted in Figure 1.1c.

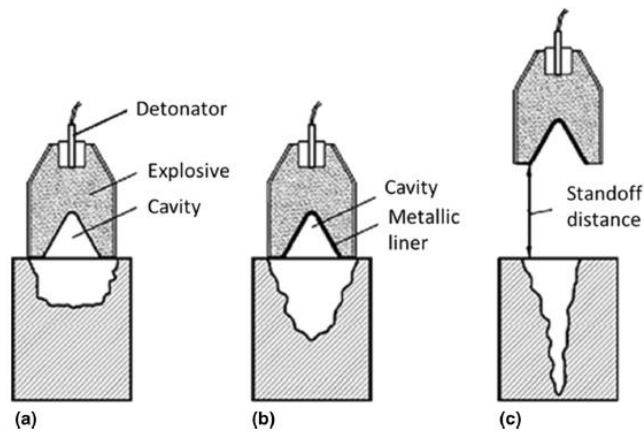


Figure 1.1. The Lined Cavity Effect [2]

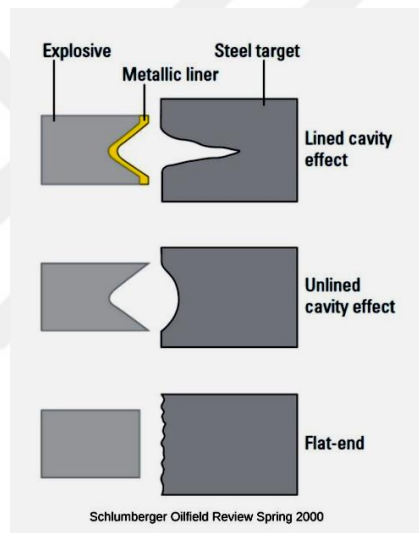


Figure 1.2 Comparison of the Effects of Hollow Cavity (Lined & Unlined) Charges and No Cavity Charge (Flat End) on Steel Targets

Figure 1.3 illustrates a typical shaped charge configuration, which generally consists of a high explosive, a concave metal cone known as the liner, and a casing made of steel or aluminum [3]. As shown in Figure 1.4, the liner diameter (LD) refers to the outer diameter of the liner. This liner is enclosed within a cylindrical explosive billet, with a charge diameter (CD). The outer diameter of the casing is referred to as the warhead diameter (WD) [1].

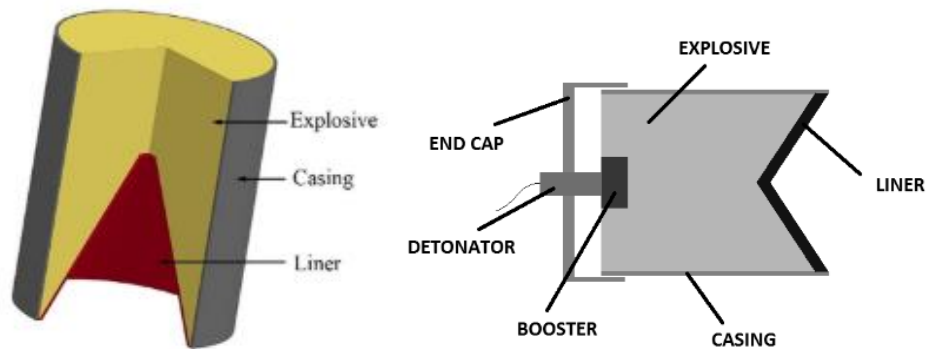


Figure 1.3 The Schematic View and Components of a Shaped Charge [3], [4]

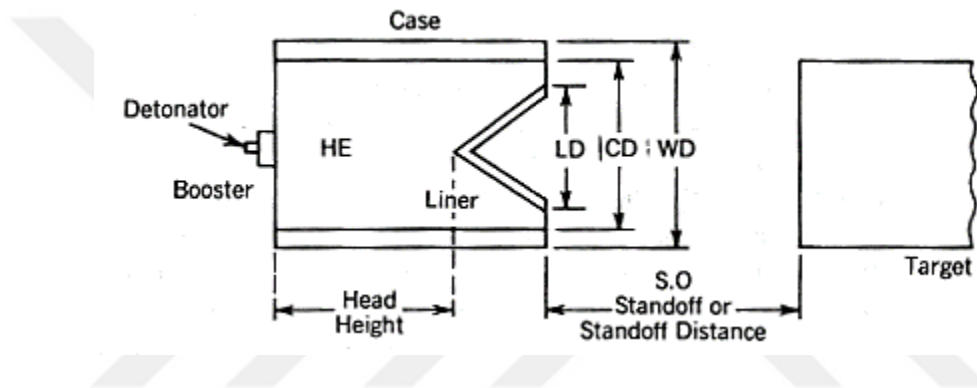


Figure 1.4 The Nomenclature of the Dimensions of a Shaped Charge; CD: Charge Diameter, WD: Warhead Diameter, LD: Liner Diameter [1]

The deformation of the liner with the detonation of explosive generates a highly destructive jet. Upon detonation, a spherical shock wave propagates outward from the initiation point, moving at extremely high velocities, typically around 8 km/s. As this high-pressure shock wave engulfs the lined cavity, the liner material is rapidly accelerated, which causes the cone to collapse.

As illustrated in Figure 1.5, for a typical conical liner, the liner material undergoes severe distortion over very short time intervals, with strain rates ranging from  $10^4$ - $10^7$ /s. Maximum strains exceeding 10 mm/mm are achieved due to the enormous hydrodynamic pressures, with peak pressures around 200 GPa and an average decay to approximately 20 GPa. The collapse of the conical liner material along the centerline drives a portion of the liner to flow as a jet, where the tip velocity can

exceed 10 km/s while the tail moves at around 3 km/s. Due to the velocity gradient, the jet elongates until it fractures into a column of "jagged" particles.

When this highly energetic jet impacts a metal plate, it forms a deep cavity, as shown in Figure 1.6, surpassing the effect of a hollow charge without a liner. The metal plate experiences peak pressures ranging from 100 to 200 GPa, which decay to an average of 10 to 20 GPa. Average temperatures in the plate are 20-50% of the melt temperature, with average strains between 0.1 and 0.5. Localized temperatures and strains at the jet tip can be even higher. The penetration occurs at strain rates of  $10^6$ - $10^7$ /s. The resulting cavity in the metal plate is attributed to the tremendous pressure exerted by the jet on the armor rather than thermal effects. The target material is displaced, with no change in mass, excluding any impact ejecta or spall from the rear surface of the target. The cavity becomes even deeper when this explosive charge, which contains the liner, is positioned at a distance from the plate, called the standoff distance [1].

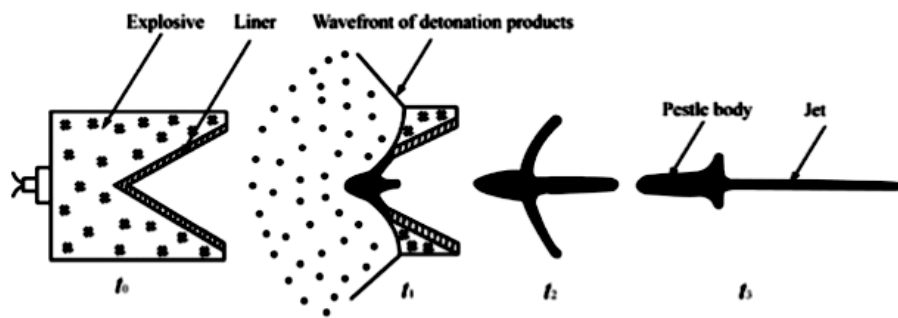
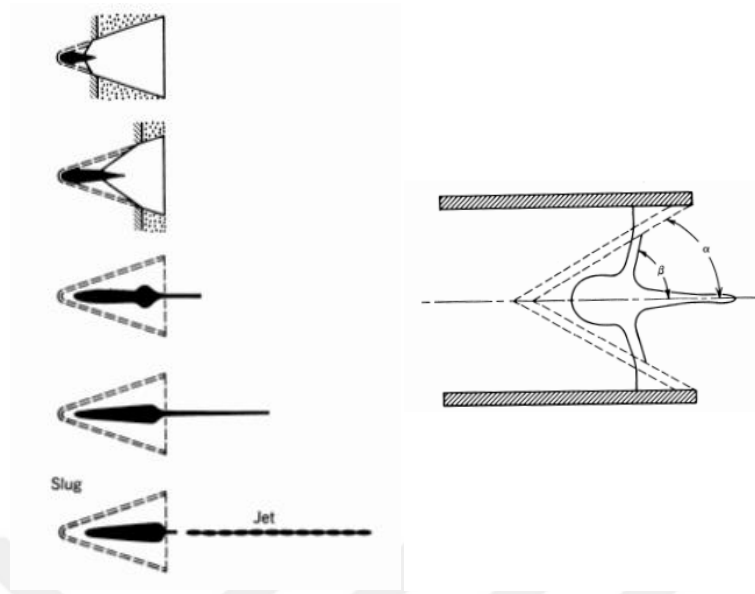


Figure 1.5 The Collapse of Shaped Charge with a Conical Liner and Jet Formation

[1], [5]

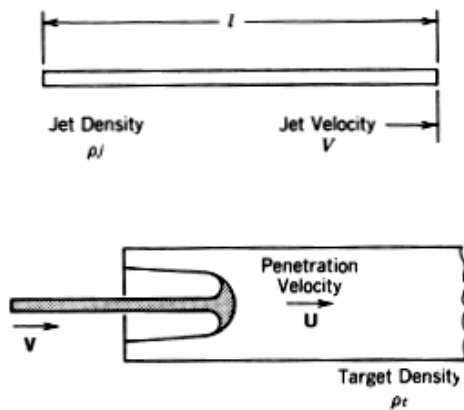


Figure 1.6 Jet Penetration [1]

The shaped charges are used in the weapon industry, such as high explosive antitank warheads (HEAT) and antiaircraft warheads such as LAW, RPG, and Javelin, which have different designs. However, the basic principle of the warhead, which is placed at the tip of the ammunition, is the same. The LAW weapon and the cross-section of the rocket are shown in Figure 1.7, and a schematic view of the RPG-7 shaped charge warhead is shown in Figure 1.8. The shaped charges are also used in the mining and construction to break rocks and collapse buildings. The linear shaped charges are used for cutting metal pipes (Figure 1.9) and concrete columns/steel structures (Figure 1.10) for demolition and even for breaking the canopy window before the ejection of the pilot seat in military aviation (Figure 1.11).

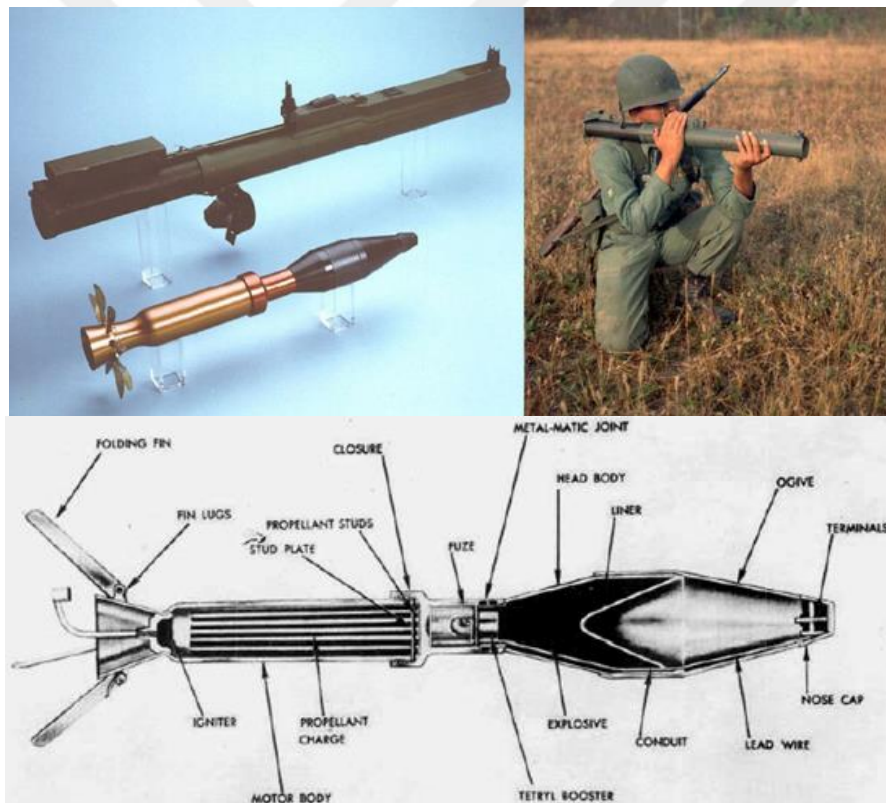


Figure 1.7 M72 LAW, 66 mm Weapon System and Its Ammunition [6], [7]

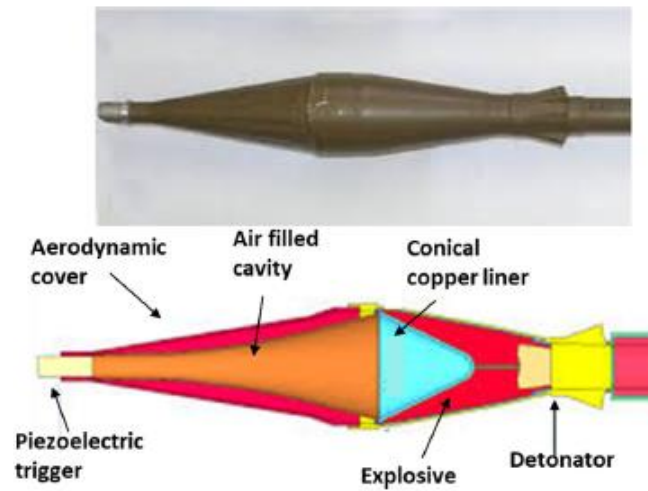


Figure 1.8 RPG-7 Antitank Ammunition and Schematic View of its Cross Section [7]



Figure 1.9 Cutting Metal Pipes with a Flexible Linear Shaped Charge [8]



Figure 1.10 Cutting Thick Block of Steel with a Linear Shaped Charge [9]

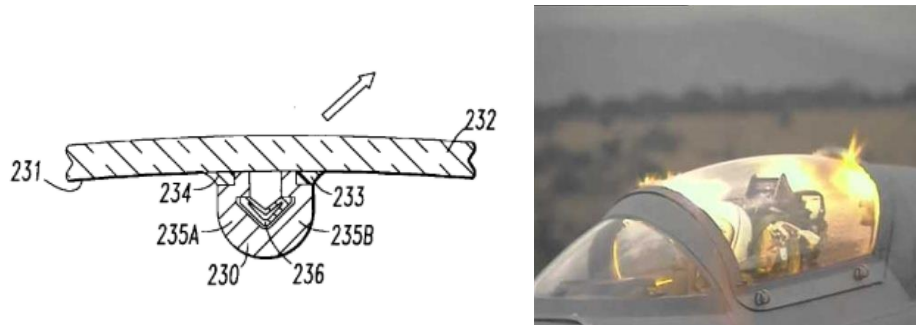


Figure 1.11 Canopy Fracturing of a Military Aircraft with a Flexible Linear Shaped Charge for the Ejection of the Pilot Seat (RH Side), The Schematical View of the Linear Shaped Charge that is Installed on the Canopy Window (LH Side) [10]

## 1.2 Shaped Charge Jet Formation

The theories governing the metal velocities after detonation of contacting explosive are investigated to understand the formation of the shaped charge jets. The most fundamental ones are the Gurney and Taylor expressions.

**The Gurney model (1943, 1947)** provides algebraic relationships for estimating the velocity imparted to a metal in contact with a detonating explosive, assuming the detonation wave strikes the metal perpendicularly. This model is based on the principles of momentum and energy conservation.

Figure 1.12 illustrates the application of the Gurney model to an open-faced sandwich. It consists of a slab of explosive confined by a metal on one side only [1].

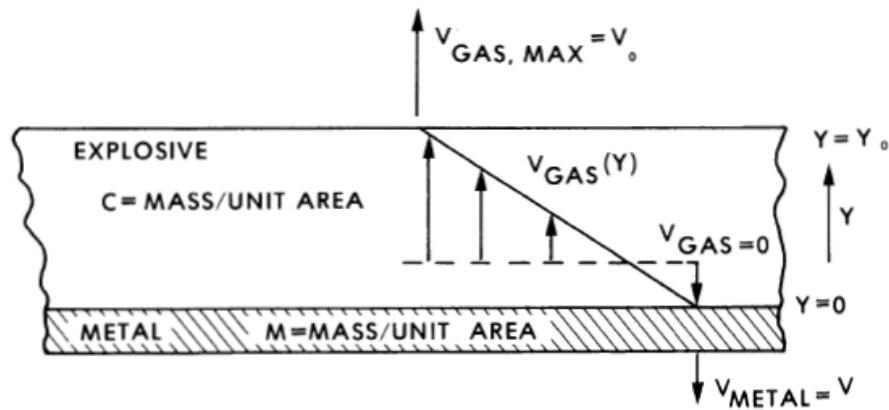


Figure 1.12 Linear Velocity Distribution for the Open-Faced Sandwich Configuration [1]

If the velocity distribution is assumed to be linear, the velocity distribution in the y-axis is as follows:

$$V_{\text{gas}}(Y) = (V_0 + V) \frac{Y}{Y_0} - V \quad (1)$$

$$CE = \frac{1}{2} MV^2 + \frac{1}{2} \rho_e \int_0^{Y_0} \left[ (V_0 + V) \frac{Y}{Y_0} - V \right]^2 dY \quad (2)$$

$$0 = -MV + \rho_e \int_0^{Y_0} \left[ (V_0 + V) \frac{Y}{Y_0} - V \right]^2 dY \quad (3)$$

$$C = Y_0 \rho_e$$

E = Specific explosive kinetic energy or the Gurney energy

M =  $\rho_m t$ ;  $\rho_m$  is the density of the metal and t is the metal thickness.

$$V = \sqrt{2E} \left[ \frac{\left(1 + 2\frac{M}{C}\right)^3 + 1}{6\left(1 + \frac{M}{C}\right)} + \frac{M}{C} \right]^{-\frac{1}{2}} \quad (4)$$

Gurney equations assume that the metal moves perpendicular to its surface, which is accurate when the detonation wave strikes the metal at normal incidence. However, in the case of a shaped charge detonation, the detonation wave impacts the metal plate at a grazing incidence. This grazing incidence is addressed by an alternative model known as the Taylor angle approximation (1941) [1].

**Taylor approximation**, illustrated in Figure 1.13, models the scenario where the detonation wave strikes the metal plate at a parallel incidence. In this model, the plate is deflected at an angle  $\theta$  from its original position. It is assumed that the metal achieves its final velocity instantaneously. Consequently, the metal plate is considered to undergo pure rotational motion without any shear, reduction in thickness, or change in length. Thus,  $\overline{OP} = \overline{OP}'$  in Figure 1.13 [1].

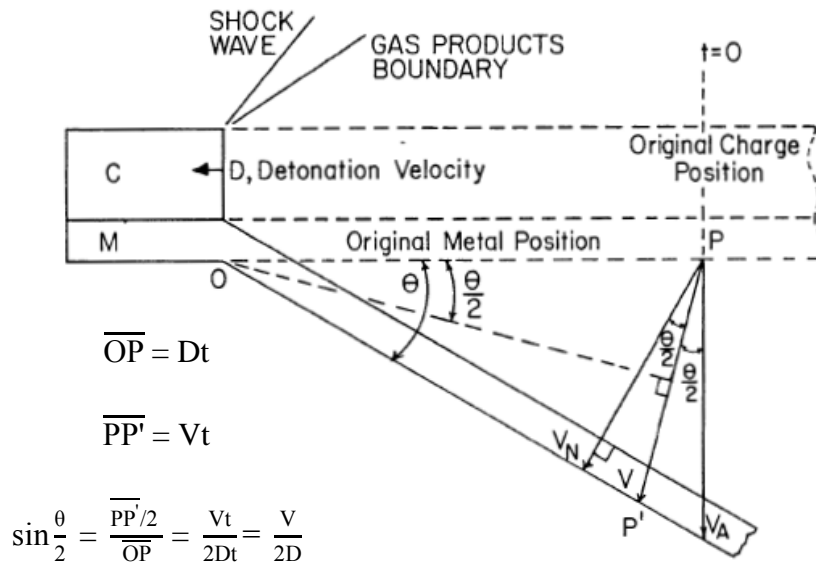


Figure 1.13 Direction of Metal Projection by a Grazing Detonation Wave [1]

**Birkhoff et al. (1948)** developed the first theory regarding the formation of conical-shaped charge jets as shown in Figure 1.14. Their model assumes that the detonation wave generates such immense pressures during the collapse process that the material strength of the liner can be neglected. The liner is treated as an inviscid, incompressible fluid, and the conical liner is modeled as a wedge. A steady-state collapse model is applied, and it is assumed that the liner elements are instantaneously accelerated to their final collapse velocity [1].

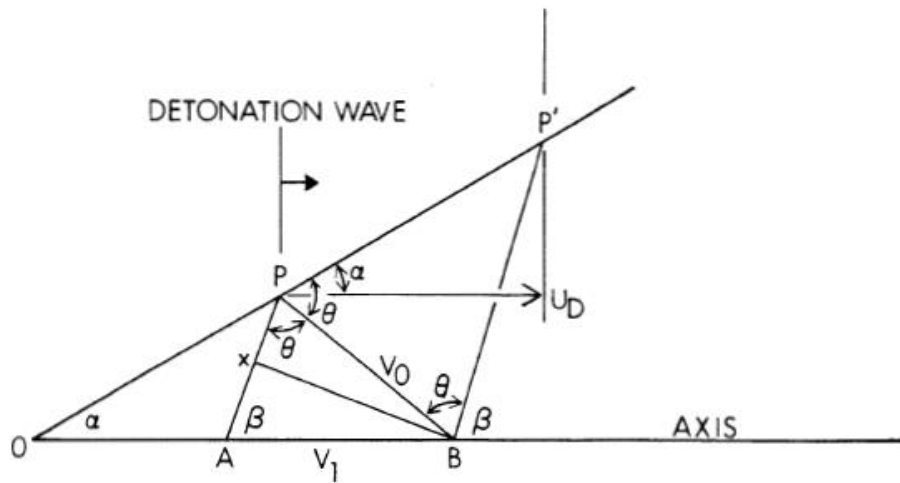


Figure 1.14 Geometry of the Collapse Process (Birkoff et al. 1948) [1]

**The PER theory (1952)** introduces the concept of a variable collapse velocity for the walls of the conical (or wedge) liner, rather than a constant collapse velocity. This approach significantly enhances the accuracy of steady-state theory results. In this model, the collapse velocity decreases from the apex to the base of the cone due to the decreasing thickness of the explosive. Figure 1.15 illustrates the impact of these velocity variations. Figure 1.15 also shows that a decreasing collapse velocity leads to a greater  $\beta$ . As the detonation wave propagates from point P to point Q along the conical surface APQ, the liner element initially at P collapses to point J. Meanwhile, the liner element initially at P' starts collapsing later, collapses more slowly than the element at P, and reaches point M at the same time that the

element at P reaches J. If both elements had identical collapse velocities, the element at P' would have reached point N by the time the element at P reached J. Consequently, if the collapse velocity were constant, the surface would maintain a conical shape, with QNJ forming a straight line. However, because P' collapses more slowly than P, the liner achieves a non-conical contour, as depicted by QMJ in Figure 1.15. Thus, the angle  $\beta$  in this scenario is greater than  $\beta^+$ , which represents the steady-state case. This model assumes that material strength effects are neglected, and each liner element is thin and does not interact with neighboring elements in the context of the hydrodynamic assumption [1].

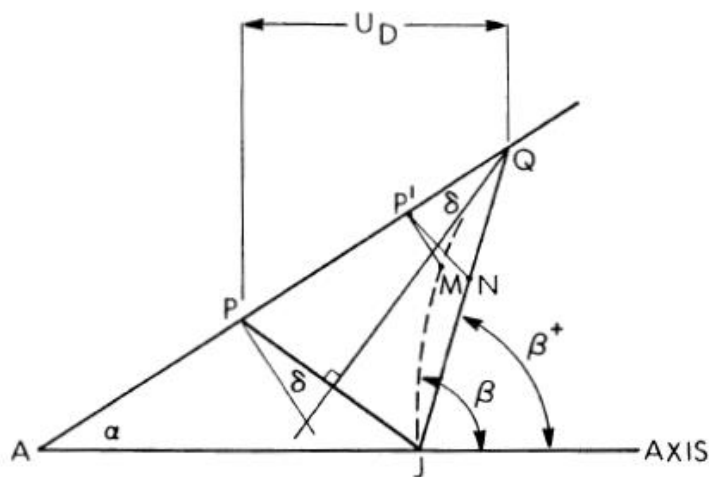


Figure 1.15 The Collapse Process for a Variable Collapse Velocity Liner (Pugh et al. 1952) [1]

A typical shaped charge jet exhibits a high tip velocity and a lower tail velocity due to the decrease in collapse velocity of the liner from the tip to the base. This velocity gradient causes the jet to stretch, particularly at large standoff distances. The length of the jet, which directly correlates with its penetration capability, is constrained by the eventual fragmentation of the jet into segments or particles. Once the jet breaks into particles, its penetration capability diminishes

significantly. Therefore, understanding the jet breakup phenomena is crucial for assessing its impact on penetration depth.

In one-dimensional analytical modeling of jet breakup phenomena, a method analogous to that used in studying liquid jet stability is employed. An initial disturbance is introduced into the jet flow, and if this disturbance amplifies, the jet becomes unstable and begins to neck. This is similar to the behavior observed in a liquid jet, such as water flowing from a faucet, which initially maintains a constant diameter but eventually develops waves and necks before breaking into droplets. While surface tension governs the stability of liquid jets, the primary factors for shaped charge jets are material strength and inertia forces. An analytical model considering these factors was developed by **Chou and Flis (1986)** [1].

Figure 1.16 illustrates a stretching jet with a wavy surface resulting from an initial disturbance. Initially, the amplitude of this wave is very small. Consider a small element within the jet, bounded by surfaces 1 and 2. Section 2 is closer to the neck of the jet, where the average axial stress is higher than at section 1 ( $\sigma_2 > \sigma_1$ ) due to stress concentration effects. It is known that stress near the neck is inversely proportional to the radius of curvature. Thus, a smaller wavelength of the disturbance leads to a greater difference in stress between sections 2 and 1. The area at section 1 is larger, and the net surface force acting on this element can be described as follows:

$$F = \sigma_2 A_2 - \sigma_1 A_1 \quad (5)$$

Despite having a smaller area than Section 1, Section 2 experiences higher flow stress due to stress concentration. If the forces acting at sections 1 and 2, which are the product of stress and area, at Section 1 ( $\sigma_1 A_1$ ) exceeds that at Section 2 ( $\sigma_2 A_2$ ), the jet becomes unstable, causing the neck to get thinner (Chou & Flis, 1986) [1]. If the force is positive, it pulls the element toward the neck, leading to its healing and thus stabilizing the jet. Conversely, if the force is negative, the element moves

away from the neck, increasing the amplitude of the disturbance and causing the jet to become unstable [1].

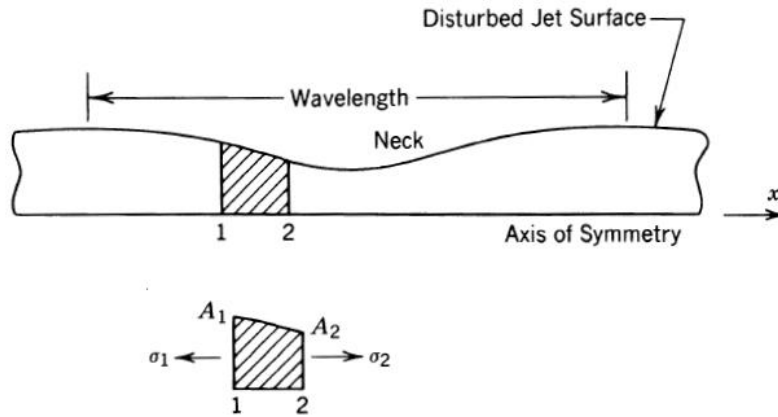


Figure 1.16 The Schematic Diagram Shows the Necking Instability of Shaped Charge Jets [1]

### 1.3 Shaped Charge Jet Penetration Models

Early analytical models of penetration, dating back to the 1940s, depended on the Bernoulli principle. Subsequently, empirical factors were introduced to account for jet particulation. Over time, models began to incorporate non-uniform-velocity (stretching) jets. Some researchers expanded these models to include considerations for jet and target strength effects, compressibility, jet drift, particle dispersion, and particle tumbling. Despite these advancements, many of these models continued to be primarily based on the Bernoulli principle or rod-type penetration models. Additionally, some models incorporated transient effects through one-dimensional conservation of mass and momentum, without relying on rod models or the Bernoulli concept [11].

**Birkhoff et al. (1948) and Hill et al. (1944)** developed a simplified penetration theory based on the hydrodynamic principles of clashing jets. Given the hypervelocity of the jet, the pressures generated upon impact with the target are

significantly higher than the yield strength of the materials involved. Therefore, as an initial approximation, the strengths and viscosities of both the jet and target materials can be disregarded, utilizing the hydrodynamic assumption of incompressible, inviscid fluid flow.

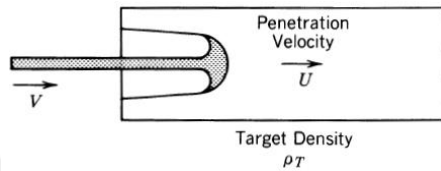
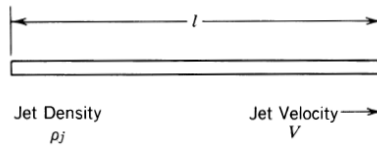


Figure 1.17 Jet Penetration [11]

Consider a shaped charge jet with length  $l$ , density  $\rho_j$ , and velocity  $V$  penetrating a semi-infinite, monolithic target with density  $\rho_T$ . The penetration velocity of the jet into the target is  $U$ , as depicted in Figure 1.17.

The analysis of penetration becomes more straightforward when observed from a coordinate system that moves with the penetration velocity  $U$ , as illustrated in Figure 1.18. In this reference frame, the profile of the hole remains stationary, the jet advances to the right at a relative velocity of  $V - U$ , and the target recedes to the left at velocity  $U$ .

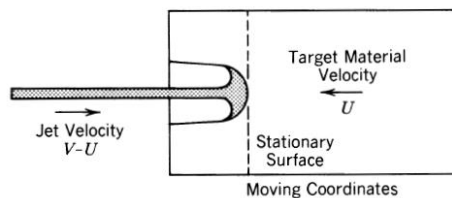


Figure 1.18 Jet Penetration with a Coordinate System Moving at the Penetration Velocity  $U$  [11]

The pressure on both sides of the interface between the jet and the target must be equal. In this steady-state system of coordinates, Bernoulli's equation can be applied along the axial streamline. Consequently, the equation takes the form:

$$\frac{1}{2}\rho_j(V - U)^2 = \frac{1}{2}\rho_T U^2 \quad (6)$$

Figure 1.18 illustrates the jet being eroded as it penetrates the target, with the assumption that a steady state is achieved instantaneously. Penetration continues until the rear of the jet impacts the target. At this point, the total penetration depth  $P$  is given by the product of the penetration velocity  $U$  and the penetration time. Therefore:

$$P = U \frac{l}{V - U} \text{ or } P = l \left( \frac{\rho_j}{\rho_T} \right)^{1/2} \quad (7)$$

Equation 7 shows that penetration depth is independent of the jet velocity. However, the rate at which the jet erodes and its final stretched length are influenced by the jet velocity through the parameter  $l$ . It is important to note that for real jets,  $l$  varies with time before the impact due to the jet stretching.

Several limitations exist with this simplified theory. Firstly, after the final jet particle impacts the target and the jet is fully consumed, the residual inertia of the penetrator can cause the hole to continue growing in depth (and width). This additional growth in penetration depth is known as secondary penetration or afterflow. The depth of the crater at the point when the jet has completely consumed is referred to as the primary penetration depth.

When the jet is fragmented into separate particles, that do not interfere with each other, these particles maintain their initial velocity ( $V - U$ ) and cross-sectional area ( $A$ ) until they impact the target. The particles are assumed to remain perfectly aligned with the penetration axis without tumbling, spreading, or diverging.

During the impact, the dynamic pressure produced by a jet particle can be approximated by dividing the total force exerted by the jet by the jet's total cross-sectional area. According to Evans (1950), the total force, depending on the change of momentum, is  $\rho_j A(V - U)^2$  and the average pressure on the impact surface  $\rho_j(V - U)^2$ . Equating this pressure to the pressure in the target material at the point of impact by using Bernoulli's equation, yields,

$$\rho_j(V - U)^2 = \frac{1}{2} \rho_T U^2 \quad (8)$$

Comparison with Equation 6 leads to

$$\lambda \rho_j(V - U)^2 = \rho_T U^2 \quad (9)$$

where  $\lambda$  adjusts the contribution of the jet's particulated nature to the penetration depth. It is considered to be 1 for a continuous jet and 2 for the jets that are fully particulated. When jets are partially particulated or become particulated during the penetration process, the value of  $\lambda$  lies between 1 and 2.  $\rho_j$  is then the average jet density considering the gaps between particles. Then, from Equation 7, the ideal primary penetration becomes:

$$P = l \left( \frac{\lambda \rho_j}{\rho_T} \right)^{1/2} \quad (10)$$

This simplified theory does not account for several important factors, including jet velocity gradients, jet-target interactions, jet alignment, shock physics, compressibility effects, aerodynamic drag, variable-area jets, transient effects, and the specific properties of the jet and target materials. For more comprehensive insights into penetration theory and secondary penetration, one can refer to the

work of Pack and Evans (1951) and Eichelberger (1956), which offer additional information [1].

**Pack and Evans** highlighted the significance of target material strength on jet penetration. To incorporate this factor into the model, they proposed modifying Equation 7 by introducing a semi-empirical correction factor. This correction accounts for the effects of material strength on penetration depth. The revised equation can be expressed as:

$$P = \left( \frac{\rho_j}{\rho_T} \right)^{1/2} l \left( 1 - \frac{\alpha Y}{\rho_j V^2} \right) \quad (11)$$

where  $Y$  is the target material yield strength, and  $\alpha$  is a constant obtained by experiments. They demonstrated that for steel, the correction term  $\alpha Y / \rho_j V^2$  can be as large as 0.3. This indicates that the effect of material strength can reduce the penetration depth by up to 30%

Significant advancements were achieved when **Eichelberger (1956)** conducted measurements of penetration-time. He confirmed that the hydrodynamic formula (Equation 6) accurately predicts penetration for early times and short standoffs, where the jet maintains a high velocity and remains unbroken. However, he found that when the jet breaks up, the parameter  $\lambda$  in Equation 9 should be less than one if  $\rho_j$  is considered as the original density of the liner. Additionally, he noted that the strengths of both the jet and the target become crucial at lower jet speeds.

Eichelberger proposed an updated formula to account for these factors:

$$\lambda \rho_j (V - U)^2 = \rho_T U^2 + 2\sigma \quad (12)$$

the term  $\sigma$  is defined as:  $\sigma = \sigma_t - \sigma_j$  where  $\sigma_t$  and  $\sigma_j$  represent the resistance to plastic deformation for the target and jet, respectively. These strength terms are typically considered to be one to three times the static uniaxial yield stress,

accounting for strain rate effects and the state of non-uniaxial stress at the yield site in the target material [11].

**Christman and Gehring (1966)** developed a model that accounts for both the primary and secondary phases of penetration. Their model aligns with experimental data for jet velocities ranging from 2.0 to 6.7 km/s. The dimensionless penetration depth into semi-infinite metal targets can be expressed as:

$$\frac{P}{L} = \left(1 - \frac{D}{L}\right) \left(\frac{\rho_j}{\rho_T}\right)^{1/2} + 2.42 \frac{D}{L} \left(\frac{\rho_j}{\rho_T}\right)^{2/3} \left(\frac{\rho_T V^2}{B_{\max}}\right)^{1/3} \quad (13)$$

This model divides the effect of the two distinct phases. The primary (or hydrodynamic) phase of penetration is represented by the first term. This term accounts for the initial penetration, where the effective length of the penetrator is reduced by one rod diameter. This reduction reflects the portion of the penetrator, which is assumed to contribute to the secondary phase of penetration which is represented by the second term. The model incorporates the Brinell hardness of the target ( $B_{\max}$ ), which influences the secondary phase of penetration. As a result, the model allows for a final penetration depth that can exceed predictions made by one-dimensional hydrodynamic theory alone [11].

**Tate** considered two types of impact scenarios based on the relationship between the strengths of the penetrator ( $\sigma_p$ ) and the target ( $\sigma_t$ ):

1. Hard Penetrator, Soft Target ( $\sigma_p > \sigma_t$ ): In this case, the penetration process occurs in two stages:
  - Initial Stage: At sufficiently high impact velocities, both the penetrator and the target flow hydrodynamically.
  - Subsequent Stage: As the penetrator decelerates, it eventually ceases to flow and starts to penetrate the target as a rigid body.
2. Soft Penetrator, Hard Target ( $\sigma_p < \sigma_t$ ): This scenario, which is of most interest, also occurs in two stages:

- Initial Stage: Both materials behave hydrodynamically upon impact.
- Subsequent Stage: Once the penetrator decelerates below a critical velocity, the target stops flowing, leading to a stop in penetration, while the penetrator continues to deform.

For both scenarios, if the impact velocity does not exceed a critical value (as calculated from Equation 12), the initial stage of purely hydrodynamic behavior will be absent. These phenomena are summarized in the phase diagram shown in Figure 1.19 [11].

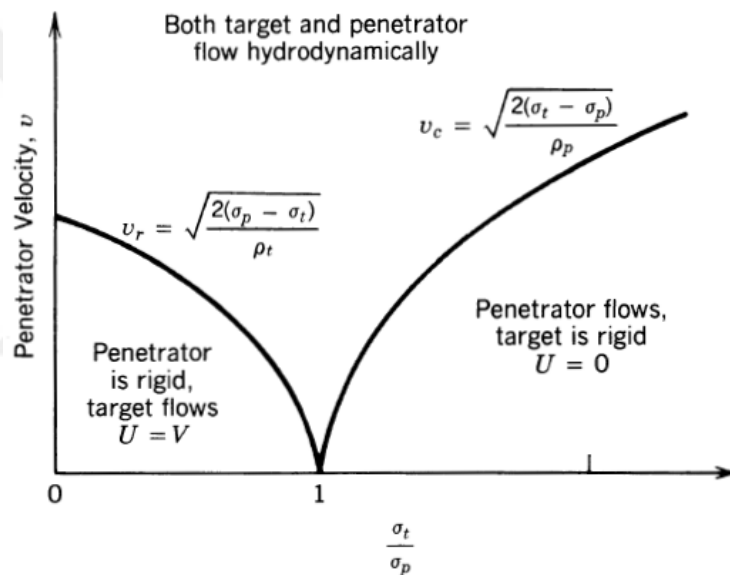


Figure 1.19 Phase Diagram of Rod Penetration According to One-Dimensional Theory (Chou and Flis 1986) [11]

## CHAPTER 2

### LITERATURE SURVEY ON COMPUTER SIMULATION OF SHAPED CHARGE JET FORMATION AND PENETRATION

#### 2.1 Finite Element Method, Lagrangian, Eulerian, and Arbitrary Lagrangian Eulerian (ALE) Descriptions

In this study, the shaped charge formation and impact case is simulated using the Finite Element Method (FEM). As a brief explanation, in this method, a continuum with infinite degrees of freedom is approximated by a finite degree of freedom system that closely mirrors the characteristics of the original model. The governing equations of this approximated model are solved exactly, which is why this approach is often referred to as providing an exact solution to approximate problems. The continuum is divided into discrete regions to perform the computations. These regions are assumed to interact only at a finite number of points, known as nodes. The displacements at these nodal points are treated as the unknowns in the problem. This approach simplifies the problem by reducing it to a system of finite degrees of freedom while still accurately representing the essential dynamics of the original continuum. The strains, stresses, and nodal forces can be obtained from the displacements. The discretization mentioned can be made with respect to different descriptions, such as Eulerian and Lagrangian.

**In Lagrangian method**, the computational grid is embedded in the material and deforms along with it (Figure 2.1). This approach tracks the motion of fixed mass elements, making it particularly accurate for monitoring material interfaces in multi-material problems, provided that material deformations are minimal. However, in impact problems where large distortions occur, several issues below arise:

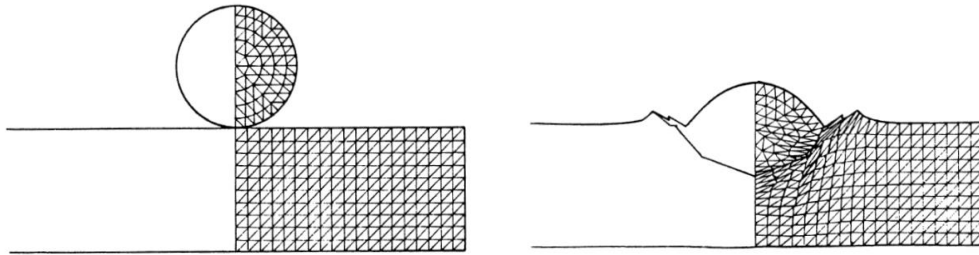


Figure 2.1 Deformation in Lagrangian System [1]

**Time Step and Computational Cost:** The time step in wave propagation codes is determined by the smallest dimension of the elements. Significant mesh distortions reduce element volume, which in turn decreases the time step. This results in excessively long computation times and high CPU costs, as the time step approaches zero and truncation errors increase.

**Element Inversion:** Four-node quadrilateral elements can become inverted, leading to calculations of negative volumes and masses. This inversion invalidates the results and requires either restarting the computation or implementing corrective measures.

**Constitutive Equation Errors:** Highly distorted elements can lead to inaccuracies in the calculation of constitutive equations, resulting in significant errors.

These problems highlight the challenges of using the Lagrangian method in scenarios with substantial material deformation, making it less suitable for problems with extreme distortion.

Two techniques are commonly employed to address issues with mesh distortions in Lagrangian simulations as stated below:

**Rezoning:** When the mesh becomes too distorted and the time step becomes excessively small (according to a user-defined criterion), a restart file is created. A new, undistorted grid is then superimposed on the existing distorted mesh. This method conserves mass, momentum, energy, and the constitutive equations. While

rezoning allows the simulation to proceed, it does involve additional computational costs (Figure 2.2).

**Erosion:** This technique is effective for problems with highly localized distortions, such as rod and jet penetration scenarios. Despite its name, "erosion" does not relate to material failure in metallurgy. Instead, it refers to a bookkeeping method for dynamically redefining sliding interfaces. When elements on an interface fail, these distorted elements are removed from the calculation (Figure 2.3). This method approximates energy conservation, as the internal energy of the failed elements cannot be tracked.

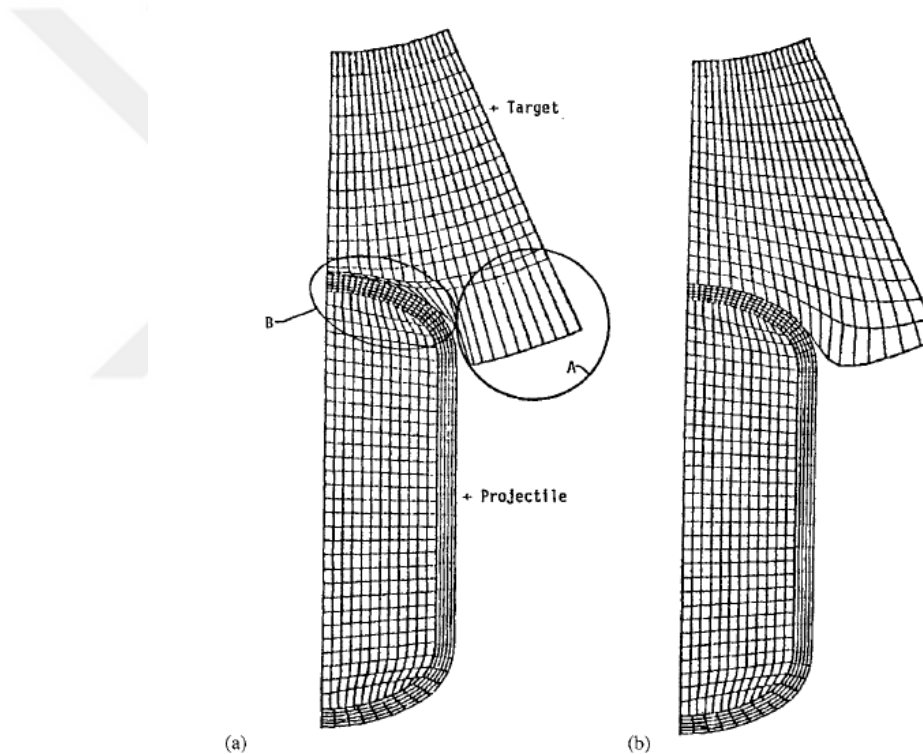


Figure 2.2 An Example of a Rezoned Calculation. (a) Mesh before Rezoning.  
(b) Mesh after Rezoning [1]

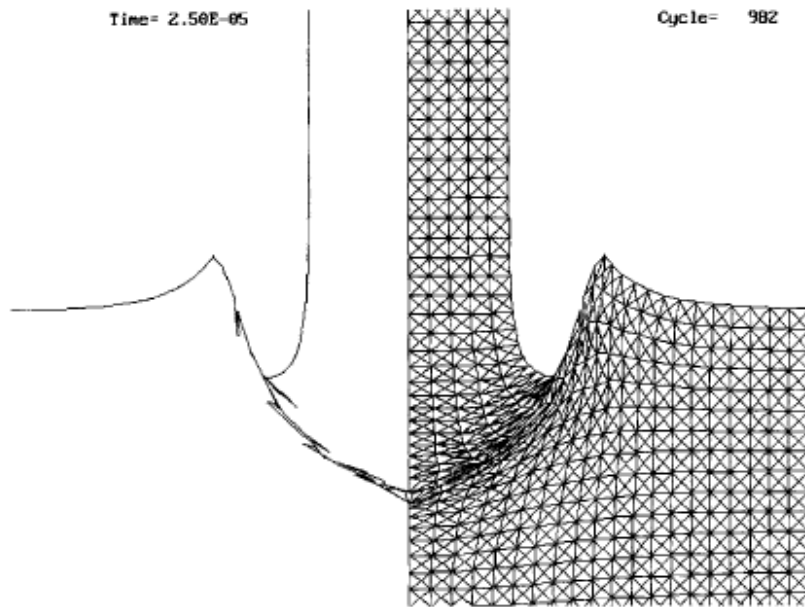


Figure 2.3 Penetration Calculation with Eroding Slide Lines at 25  $\mu$ s after Impact  
[1]

In **Eulerian method**, a fixed grid mesh is used, through which mass flows. This method can handle large deformations more easily because the grid remains constant while the material moves through it. However, tracking material interfaces and calculating mass, momentum, and energy flux across zone boundaries can be challenging. For surface-to-surface interactions, it is crucial to identify different materials to accurately calculate pressures in cells containing multiple materials. This task is complex for Eulerian codes, which are primarily designed for large flow problems and often struggle with solving contact problems and material interfaces without additional Lagrangian features.

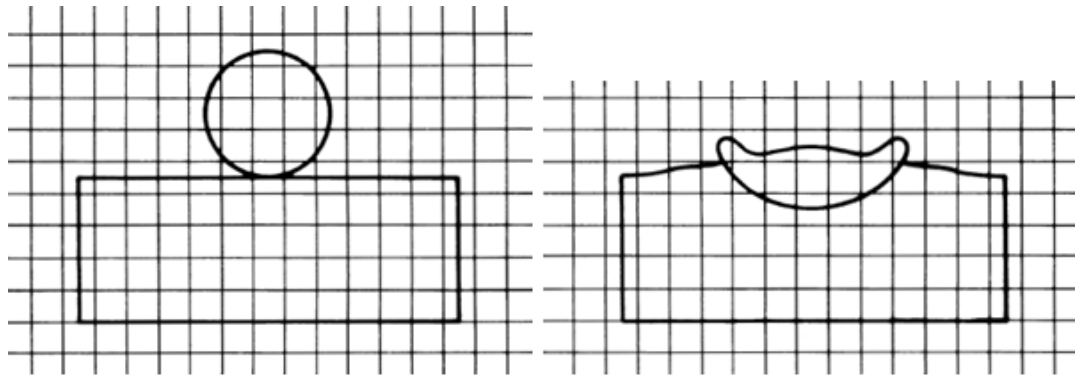


Figure 2.4 Deformation in Eulerian System [1]

Conversely, Lagrangian methods involve a grid that is embedded in the material and deforms along with it. These codes track the flow of individual masses directly, making them conceptually more straightforward for problems involving material and structural interfaces. They do not require transport algorithms, which simplifies computations and provides more accurate time histories and material interface details. However, Lagrangian methods face difficulties with large distortions, as the grid can become highly distorted over time.

Eulerian codes primarily address problems involving hypervelocity impacts, where pressures are much higher than material strength, treating the material as a fluid. These codes perform well in modeling early stages of impact and crater formation but are less effective when material strength was considered [12].

Eulerian and Lagrangian methods each have their own strengths and limitations, as summarized in Table 2.1. Eulerian codes are adept at handling large distortions due to their fixed grid mesh, which facilitates the tracking of material flow through the grid. However, accurately treating material interfaces and boundaries and calculating fluxes can be challenging, especially in scenarios involving significant contact.

Table 2.1 Comparisons of Lagrangian and Eulerian Methods [13]

	<b>Lagrangian Method</b>	<b>Eulerian Method</b>
Grid	Attached on the moving material	Fixed in the space
Track	Movement of any point on materials	Mass, momentum and energy flux across grid nodes and mesh cell boundary
Time history	Easy to obtain time-history data at a point attached on materials	Difficult to obtain time history data at a point attached on materials
Moving boundary and interface	Easy to track	Difficult to track
Irregular geometry	Easy to model	Difficult to model with good accuracy
Large deformation	Difficult to handle	Easy to handle

In contrast, Lagrangian codes excel at tracking interfaces and material flows because the grid deforms along with the material. This approach simplifies the process of determining time histories and material interfaces, making it conceptually straightforward and computationally efficient. Nevertheless, Lagrangian methods struggle with large distortions due to the deformation of the grid.

**The Arbitrary Lagrangian-Eulerian (ALE)** method was developed to address these challenges. ALE combines the benefits of both approaches, allowing for an arbitrary mix of Lagrangian and Eulerian descriptions based on user-defined mesh movements. The ALE method utilizes rezoning techniques similar to those in Lagrangian methods to minimize mesh distortion by allowing the mesh to move independently of the materials.

In practice, ALE starts with Lagrangian motion at each time step, and then proceeds to a rezoning stage. During this stage, the mesh can either remain unchanged (pure Lagrangian), revert to its original shape (Eulerian), or be adjusted to a more advantageous configuration that blends elements of both approaches. This flexibility helps to optimize computational efficiency by localizing intense calculations to areas with significant distortions.

ALE codes often feature automatic rezoning, which improves accuracy compared to user-defined methods and allows for better computational optimization. This capability also enables the treatment of some portions of the system with Eulerian methods and others with Lagrangian methods, particularly useful in multimaterial problems where large distortions are confined to specific regions [12].

The governing equations of ALE are as follows [13], [14]:

**i. Conservation of Mass (Continuity Equation):**

The ALE formulation modifies the standard continuity equation to account for the motion of the computational grid. The continuity equation is given as:

$$\frac{\partial \rho}{\partial t} + \rho \operatorname{div}(\vec{v}) + (\vec{v} - \vec{w}) \operatorname{grad}(\rho) = 0 \quad (14)$$

Where:

$\rho$  = fluid density

$\vec{v}$  = material velocity

$\vec{w}$  = mesh (grid) velocity

$\vec{v} - \vec{w}$  = relative velocity between the material and the grid

## ii. Conservation of Momentum

In the ALE framework, the momentum equation is expressed as:

$$\rho \frac{\partial \vec{v}}{\partial t} + \rho(\vec{v} - \vec{w}) \text{grad}(\vec{v}) = \text{div}(\sigma) + \vec{f} \quad (15)$$

Where:

$\sigma$  = Cauchy stress tensor

$\vec{f}$  = Body forces per unit volume (e.g., gravity)

## iii. Conservation of Energy

The energy equation in ALE takes the form:

$$\rho \frac{\partial e}{\partial t} + \rho(\vec{v} - \vec{w}) \text{grad}(e) = \sigma : \text{grad}(\vec{v}) + \vec{f} \cdot \vec{v} \quad (16)$$

$e$  = Total energy per unit mass

$\vec{v}$  and  $\vec{w}$  are the fluid and mesh velocities, respectively, and they can differ. The mesh motion can be independent of the material motion. This is the main characteristic of ALE formulation. If  $\vec{v} = \vec{w}$ , Equations 14, 15, and 16 give the lagrangian formulation. When  $\vec{w} = 0$ , the stationary mesh condition gives a pure Eulerian formulation.

The conservation of mass, momentum, and energy equations may be written in more compact forms, such as:

$$\frac{\partial \rho}{\partial t} + \text{div}(\rho \vec{v}) = 0 \quad (17)$$

$$\frac{\partial \rho \vec{v}}{\partial t} + \text{div}(\rho \vec{v} \otimes \vec{v}) = \text{div}(\sigma) + \vec{f} \quad (18)$$

$$\frac{\partial (\rho e)}{\partial t} + \text{div}(e \vec{v}) = \sigma : \text{grad}(\vec{v}) + \vec{f} \cdot \vec{v} \quad (19)$$

Equations 17, 18, and 19 can have the following form:

$$\frac{\partial \Phi}{\partial t} + \text{div}(\Phi) = S \quad (20)$$

$$\text{Where } \Phi = \begin{bmatrix} \rho \\ \rho \vec{v} \\ \rho e \end{bmatrix}, \quad \Phi = \begin{bmatrix} \rho \vec{v} \\ \rho \vec{v} \otimes \vec{v} \\ e \vec{v} \end{bmatrix}, \quad \text{and } S = \begin{bmatrix} 0 \\ \text{div}(\sigma) + \vec{f} \\ \sigma : \text{grad}(\vec{v}) + \vec{f} \cdot \vec{v} \end{bmatrix}$$

Equation 20 is solved in 2 steps by the split approach: first, a Lagrangian cycle and then an advection cycle.

During the Lagrangian cycle a finite element code solves the following equation:

$$\frac{\partial \Phi}{\partial t} = S \quad (21)$$

During the advection cycle, the mesh is taken back to its original position. The finite element method solves the lagrangian solution on the new position of mesh by solving the following transport equation [13], [14]:

$$\frac{\partial \Phi}{\partial t} + \text{div}(\Phi) = 0 \quad (22)$$

## 2.2 Smoothed Particle Hydrodynamics

All the discussed methods—Eulerian, Lagrangian, and ALE—use a computational grid to provide structure and order. In contrast, the Smoothed Particle Hydrodynamics (SPH) technique operates without an underlying grid [12]. Instead, SPH represents the state of a system using a set of particles, each with individual material properties, which move according to the governing conservation equations. Initially developed to tackle astrophysical problems in three-dimensional open space, SPH has unique characteristics that offer certain advantages over traditional grid-based numerical methods [15].

The SPH method, a mesh-free, Lagrangian particle approach, has notable benefits:

1. **Mesh-Free Computation:** The absence of a mesh allows SPH to handle large deformations and separations more easily.
2. **Lagrangian Formulation:** SPH's Lagrangian nature links it directly to standard finite-element Lagrange formulations. This connection means that both elastic and very large deformations, including material failure, can be computed using a single method. This is beneficial for solving both structural dynamics and wave propagation problems [12].

The term "Smoothed Particle Hydrodynamics" encapsulates the method's core features:

- **Smoothed:** Refers to the technique of approximating properties by averaging over neighboring particles to ensure numerical stability.
- **Particle:** Indicates that the system is represented by discrete particles rather than a continuous mesh.
- **Hydrodynamics:** Highlights its application to hydrodynamic problems, where materials under hypervelocity impacts behave like fluids. In such cases, the kinetic energy of the system can cause extreme deformation and even fragmentation of materials.

SPH is particularly effective in scenarios like hypervelocity impacts and penetration, where materials undergo significant deformation and may fragment. Traditional grid-based methods may struggle with these extreme conditions, but SPH handles them well. However, this method struggles in cases where material strength can not be neglected. An example of an impact simulation conducted with these methods are shown in Figure 2.5 [15], [16].

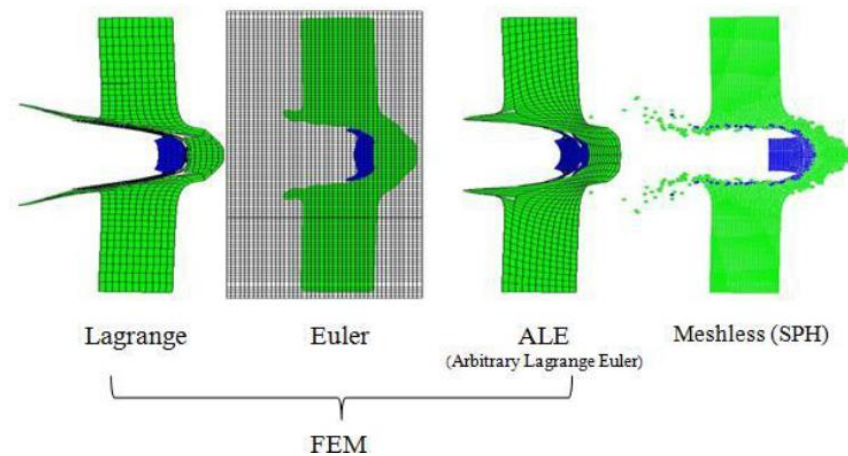


Figure 2.5 Examples of Lagrange, Euler, ALE and SPH Simulations [16]

## 2.3 Equation of State and Material Models

### 2.3.1 Equation of State

In a high-velocity impact or explosion, the pressures generated in a solid, which exceed material strength more than 10 times, lead to shock wave formation. Under this condition, the solid is considered as a compressible fluid. Its behavior is described by an equation of state (EOS). The EOS is the relationship between pressure, density, and internal energy. It can be considered as a constitutive model for materials under shock loading [12].

The problem that is to be solved is as follows: given material at an initial pressure  $P_0$ , temperature  $T_0$ , and energy  $E_0$ , what is the resulting pressure  $P(v)$ , temperature  $T(v)$ , and energy  $E(v)$  when the material is subjected to shock compression causing a reduction from an initial specific volume  $v_0$  to a specific volume  $v < v_0$  [17] ?

### 2.3.1.1 Mie-Gruneisen

Mie-Gruneisen EOS is used mainly for solid materials such as copper, steel, and aluminum [12]. The articles [18] and [19] claim that Mie-Gruneisen EOS is also applicable for water. The general form is

$$P - P_H = \gamma\rho(E - E_H) \quad (23)$$

where  $P$  and  $E$  are the pressure and internal energy in the material at the state of interest, subscript  $H$  refers to the Hugoniot state (A reference state used to obtain empirical equations between  $P$  and  $\rho$ ) obtained from experiments. The remaining parameters,  $\gamma$ , and  $\rho$ , are the Gruneisen gamma and the shock-compressed density, respectively. The Gruneisen gamma can take many forms, and for the present application, gamma is defined by:

$$\gamma = \frac{\gamma_0 + b\mu}{1 + \mu} \quad (24)$$

where  $\gamma_0$  is the value of the Gruneisen gamma at ambient conditions, “ $b$ ” is the first-order volume correction to  $\gamma_0$ , and  $\mu$  is a measure of the compression,  $\mu = \rho/\rho_0 - 1$ . Rearranging Equation 23 with the insertion of the definition of  $\mu$  and recognizing that  $E_H = \frac{1}{2}P_H\left(\frac{1}{\rho_0} - \frac{1}{\rho}\right)$  gives:

$$P = P_H\left(1 - \frac{\gamma\mu}{2}\right) + \gamma\rho E \quad (25)$$

Equation 25 can be further expanded using the conservation of momentum relation,  $P_H = \rho_0 U_s u_p$ , assuming that the initial pressure  $P_0$  is negligible. The conservation of momentum equation introduces two new parameters: the shock velocity  $U_s$  and the material (or particle) velocity  $u_p$ . The shock velocity represented in the cubic form is given by:

$$U_s = C_0 + S_1 u_p + S_2 \left( \frac{u_p}{U_s} \right) u_p + S_3 \left( \frac{u_p}{U_s} \right)^2 u_p \quad (26)$$

where  $C_0$  is the bulk sound speed of the material at ambient conditions, and the parameters  $S_1$ ,  $S_2$ , and  $S_3$  are fitting parameters determined from the measured Hugoniot. (A third order curve is fitted to the points that are obtained from experiments. The fitting parameters are the constants of the different order unknowns.) To determine  $S_{1,2,3}$ , one must use the conservation of mass equation,  $\rho_0 U_s = \rho(U_s - u_p)$ , rearranged in the following manner:

$$u_p = U_s \left( 1 - \frac{1}{1+\mu} \right) \quad \text{or} \quad \frac{u_p}{U_s} = \left( 1 - \frac{1}{1+\mu} \right) \quad (27)$$

which, when substituted in to Equation 26, results in a function for  $U_s$  in terms of compression:

$$U_s = \frac{C_0}{\left[ 1 - S_1 \left( 1 - \frac{1}{1+\mu} \right) - S_2 \left( 1 - \frac{1}{1+\mu} \right)^2 - S_3 \left( 1 - \frac{1}{1+\mu} \right)^3 \right]} \quad (28)$$

When Equation 27 is substituted back into Equation 25 through the conservation of momentum relation, this gives:

$$P = \underbrace{\rho_0 U_s^2}_{a} \underbrace{\left( 1 - \frac{1}{1+\mu} \right) \left( 1 - \frac{\gamma\mu}{2} \right)}_b + \underbrace{\gamma\rho E}_c \quad (29)$$

which must be further manipulated to achieve the desired form of the Mie-Gruneisen EOS. Beginning with segment (a) of Equation 29, one arrives at:

$$\rho_0 U_s^2 = \frac{\rho_0 C_0^2}{\left[1 - S_1 \left(1 - \frac{1}{1+\mu}\right) - S_2 \left(1 - \frac{1}{1+\mu}\right)^2 - S_3 \left(1 - \frac{1}{1+\mu}\right)^3\right]^2} \quad (30)$$

Distributing segment (b) results in:

$$\left[1 - \frac{\gamma\mu}{2} - \frac{1}{1+\mu} + \frac{\gamma\mu}{2(1+\mu)}\right] \quad (31)$$

Substitution of Equation 24 and the definition of  $\mu$  into segment (c) gives:

$$[\gamma_0 + b\mu]\rho_0 E \text{ or } [\gamma_0 + b\mu]\epsilon \quad (32)$$

noting that  $\epsilon = E \rho_0$  is the energy per initial unit volume ( $V_0 = 1/\rho_0$ ). Substituting Equations 30, 31, and 32 into Equation 29 yields:

$$P = \frac{\rho_0 C_0^2 \left[1 - \frac{\gamma\mu}{2} - \frac{1}{1+\mu} + \frac{\gamma\mu}{2(1+\mu)}\right]}{\underbrace{\left[1 - S_1 \left(1 - \frac{1}{1+\mu}\right) - S_2 \left(1 - \frac{1}{1+\mu}\right)^2 - S_3 \left(1 - \frac{1}{1+\mu}\right)^3\right]^2}_d} + [\gamma_0 + b\mu]\epsilon \quad (33)$$

Multiplying both the numerator and denominator of the segment (d) in Equation 30 by  $(1 + \mu)^2 / (1 + \mu)^2$  results in the Mie-Gruneisen EOS in the desired form:

$$P = \frac{\rho_0 C_0^2 \mu \left[1 + \left(1 - \frac{\gamma_0}{2}\right)\mu - \frac{b}{2}\mu^2\right]}{\left[1 - (S_1 - 1)\mu - S_2 \frac{\mu^2}{1+\mu} - S_3 \frac{\mu^3}{1+\mu}\right]^2} + [\gamma_0 + b\mu]\epsilon \quad (34)$$

Equation 25 is the form of the Mie-Gruneisen EOS that describes the response of a material under compression. In tension, the EOS takes a much simpler form:

$$P = \rho_0 C_0^2 \mu + \gamma_0 \epsilon \quad (35)$$

The Mie-Gruneisen EOS assumes that materials do not undergo phase changes, meaning that if a material starts as a solid, it remains a solid under the Mie-Gruneisen EOS. Alternative EOS models must be used for situations where materials transition from solid to liquid or gas due to increased temperature and pressure. These include the Tillotson, Gray, and Los Alamos EOS, which can account for phase transitions [20].

### 2.3.1.2 Jones-Wilkins-Lee (JWL) for Explosives

The equation describing the relationship between pressure, density, and temperature of explosive products is known as the Equation of State (EOS) of the explosive. A widely used form is the Jones-Wilkins-Lee (JWL) EOS. This equation, given in Equation 36, effectively characterizes the pressure-volume-energy behavior of detonation products in metal acceleration applications. In the JWL EOS,  $A$ ,  $B$ ,  $R_1$ ,  $R_2$ , and  $\omega$  are constants determined through experimental data,  $E$  represents the initial internal energy per unit mass, and  $V$  is the relative volume ( $V/V_0$ ).

$$P = A \left(1 - \frac{\omega}{R_1 V}\right) e^{-R_1 V} + B \left(1 - \frac{\omega}{R_2 V}\right) e^{-R_2 V} + \frac{\omega E}{V} \quad (36)$$

### 2.3.1.3 Linear Polynomial

$$P = C_0 + C_1 \mu + C_2 \mu^2 + C_3 \mu^3 + (C_4 + C_5 \mu + C_6 \mu^2) E \quad (37)$$

The linear polynomial equation of state may be used to model gases [21], [22]. This may be achieved for the air, by setting  $C_0=C_1=C_2=C_3=C_6=0$  and  $C_4=C_5=\gamma-1$ , where  $\gamma$  is the ratio of specific heats.

## 2.3.2 Material Models

### 2.3.2.1 Johnson-Cook Model

Johnson-Cook model is a function of Von Mises tensile flow stress with respect to strain hardening, strain rate hardening, and thermal softening. Johnson-Cook's formulation of the flow stress is expressed by

$$\sigma = (A + B\bar{\epsilon}^{pn}) (1 + C \ln \dot{\epsilon}^*) (1 - T^{*m}) \quad (38)$$

where A, B, C, n, and m are material constants.  $\bar{\epsilon}^p$  is the effective plastic strain, and  $\dot{\epsilon}^*$  is the effective plastic strain rate. Relative temperature is given by

$$T^* = (T - T_{\text{room}})(T_{\text{melt}} - T_{\text{room}}) \quad (39)$$

The strain at fracture is given by

$$\epsilon_f = [D_1 + D_2 \exp(D_3 \sigma^*)] [1 + D_4 \ln(\dot{\epsilon}^*)] [1 + D_5 T^*] \quad (40)$$

where  $D_1$ ,  $D_2$ ,  $D_3$ ,  $D_4$  and  $D_5$  are material constants.  $\sigma^* = \frac{P}{\bar{\sigma}}$  is the ratio of pressure divided by the Von Mises equivalent stress,  $\bar{\sigma} = [(3/2)s_{ij}s_{ij}]^{\frac{1}{2}}$ . Note that  $s_{ij}$  is the deviator stress tensor.

The fracture occurs when the damage parameter  $D = \Sigma(\Delta\bar{\epsilon}^p/\epsilon_f)$  reaches the value of 1 [23].

Johnson-Cook is a plasticity model derived from true stress-true strain curves of the materials at different strain rates and temperatures, as shown in Figure 2.6. True stress is a function of true strain containing elastic and plastic strain. However, Johnson-Cook is the function of equivalent plastic strain. It neglects elastic strain since it is developed to deal with excessive deformation problems at high strain rates and temperatures due to impulsive loading, such as high-velocity impact and explosive detonation [24]. In such cases, true strain can reach over 2 until ductile materials fracture. In contrast, elastic strain is usually less than 0.01 at the fracture of the steels which is less than 1% of the total strain. (Considering that the steel materials have approximately 200 GPa modulus of elasticity, and as an example, 4340 steel, a high strength material, and is used in the research of G.R Johnson & W.H. Cook, fails approximately at 1400 MPa tensile stress [24]. The ratio of true stress/elasticity modulus gives the elastic strain). Thus, the strain and deformation caused by elastic deformations are neglected. As shown in Figure 2.6, due to the large values of true tensile strains, the elastic region of the curve is so close to the y-axis that this region is not visible at this scale. Johnson-Cook plastic flow curves are developed to start from the yield point at the reference strain rate and temperature by neglecting this elastic region.

It is possible to obtain Johnson-Cook parameters from true stress- true strain curves as explained by Murugesan & Jung, 2019 [25]:

**Determination of material constants, B and n:** It is assumed that the strain rate and temperature are at the reference state. Since, the second and third terms in Equation 38 become equal to unity at low strain rates and at room temperature, it takes the following form:

$$\sigma = (A + B\bar{\epsilon}^{p^n}) \quad (41)$$

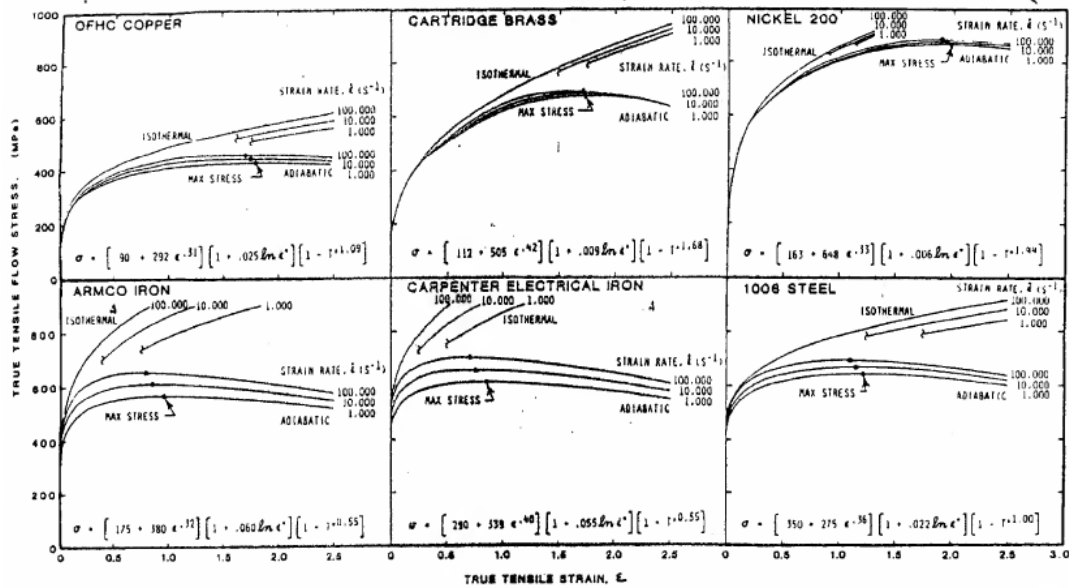


Figure 2.6 Johnson-Cook Models of Various Metals Derived from True Stress-True Strain Curves [24]

By taking natural logarithm of both sides of Equation 41:

$$\ln(\sigma - A) = n \ln \dot{\epsilon} + \ln B \quad (42)$$

By substituting the true stress and strain values that are obtained from tests into Equation 42, the linear relationship between  $\ln(\sigma - A)$  and  $\ln \dot{\epsilon}$  was drawn, and then the first-order regression is applied to fit the data points as depicted in Figure 2.7. Here,  $n$  is the slope of this linear curve, and  $\ln B$  is the value where it cuts the y-axis.

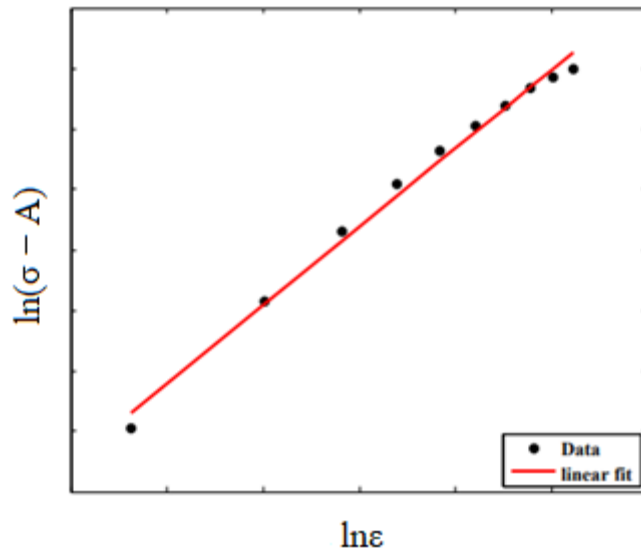


Figure 2.7 The Relationship between  $\ln(\sigma - A)$  and  $\ln\epsilon$  [25]

**Determination of material constant, C:** Having determined the constants A and n, this time only the temperature is assumed to be at the reference state. Thus,

$$\sigma = (A + B\bar{\epsilon}^{p^n}) (1 + C \ln \dot{\epsilon}^*) \quad (43)$$

Then,

$$\frac{\sigma}{(A + B\bar{\epsilon}^{p^n})} = (1 + C \ln \dot{\epsilon}^*) \quad (44)$$

The slope of the linear regression of datapoints gives the value of C, as shown in Figure 2.8.

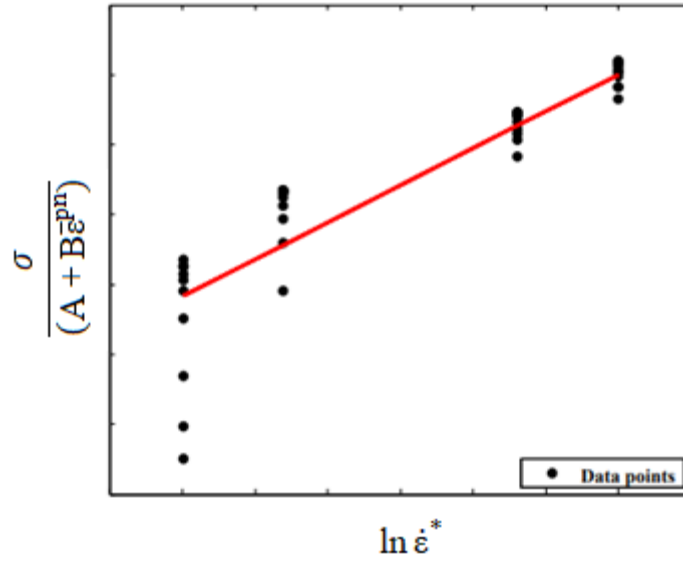


Figure 2.8 The Relationship between  $\frac{\sigma}{(A + B\bar{\epsilon}^{p^n})}$  and  $\ln \dot{\epsilon}^*$  [25]

**Determination of material constant, m:** This time only the strain rate is assumed to be at the reference state. Thus,

$$\sigma = (A + B\bar{\epsilon}^{p^n}) (1 - T^{*m}) \quad (45)$$

Then,

$$1 - \frac{\sigma}{(A + B\bar{\epsilon}^{p^n})} = T^{*m} \quad (46)$$

By taking natural logarithm of both sides of Equation 46:

$$\ln \left[ 1 - \frac{\sigma}{(A + B\bar{\epsilon}^{p^n})} \right] = m \ln T^* \quad (47)$$

The slope of the linear regression of datapoints gives the value of m, as shown in Figure 2.9.

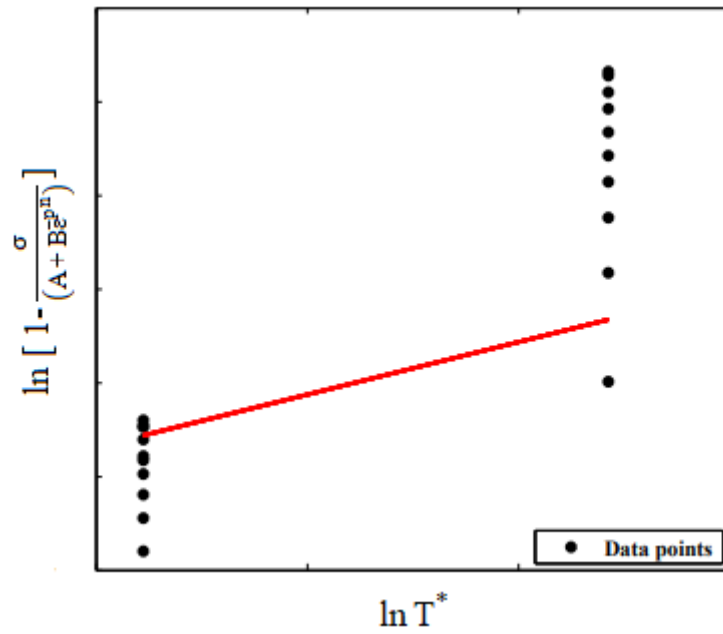


Figure 2.9 The Relationship between  $\ln \left[ 1 - \frac{\sigma_y}{(A + B\epsilon^p)} \right]$  and  $\ln T^*$  [25]



## CHAPTER 3

### LITERATURE REVIEW ON ADD-ON ARMOR SYSTEMS AND SCOPE OF THE RESEARCH

#### 3.1 Conventional Add-on Armor Systems Used on Armored Vehicles: Explosive Reactive Armors and Non-Explosive Reactive Armors

In order to meet the protection standards against a modern antitank warhead, the armor of a main battle tank today consists of a rolled homogeneous armor (RHA) and an add-on (applique) armor. While the RHA provides the tank standard protection and strong structural integrity, the add-on armor enhances its protection level for defeating modern antitank warheads. Add-on armor generally has two types, namely reactive armor (explosive reactive armor) and inert (non-explosive reactive) armor [26].

**Explosive reactive armor (ERA)** is made of a slab of high explosive embedded between two metal plates. The explosive detonates when a shaped charge jet penetrates it and creates a disturbance to the jet. Hence, the jet loses its coherency, linearity, and penetration power [26], as shown in Figure 3.1 and Figure 3.2. However, the detonation may harm surrounding personnel, limiting its usage.

Figure 3.1 shows the jet penetration through the ERA at different obliquity angles. The disturbance on the jet is more noticeable when the impact angle is  $30^\circ$  (Picture on the RH side) [27].

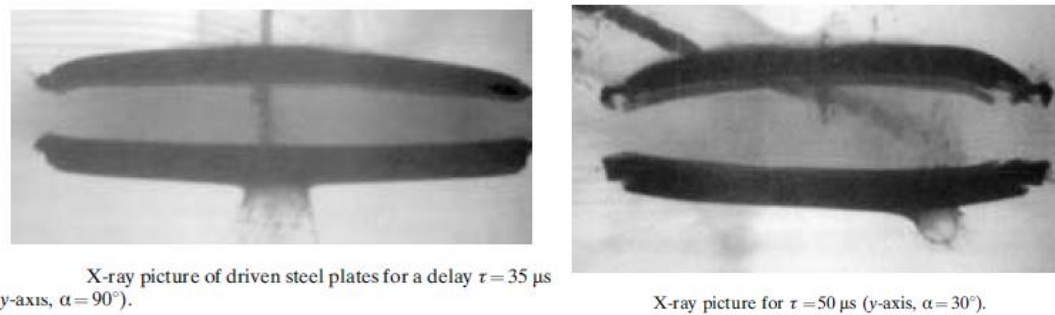


Figure 3.1 The X-ray Pictures of the Shaped Charged Jet Disturbance by Explosive Reactive Armor at Different Impact Angles [27]

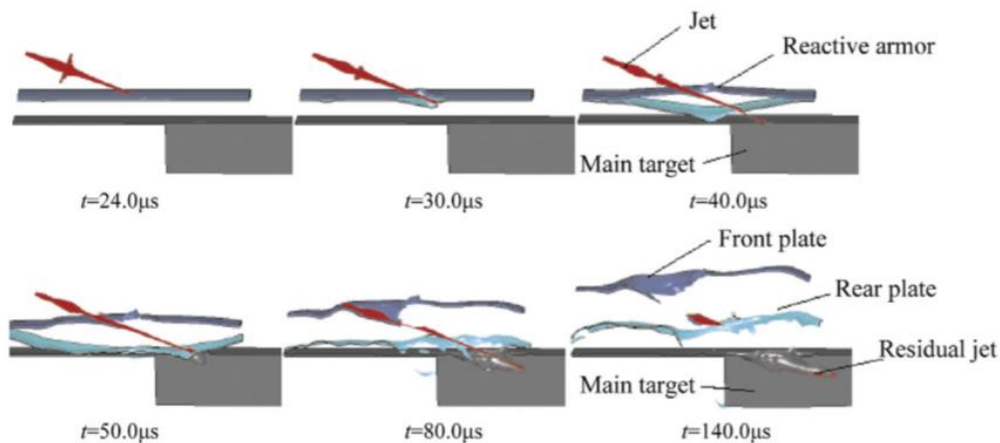


Figure 3.2 The Numerical Simulation of the Disturbance of the Shaped Charged Jet by Explosive Reactive Armor [23]

**Non-explosive reactive armor (NERA)** operates similarly to explosive reactive armor. However, there is no explosive layer. An inert material, such as rubber or composite materials, is embedded between two metal layers. When it is impacted by a shaped charge's metal jet, it dissipates the impact energy.

In this study, pure water, a lightweight and easy-to-find liquid material is used as an inert layer, and its effectiveness against a shaped charge jet is investigated.

### 3.2 The Mechanism of Jet Dispersion in the Liquid Filled Chamber

The liquid filled structure target affects the shaped charge jet stability by reflecting shock waves from the cylindrical sidewalls and bottom plate of the chamber.

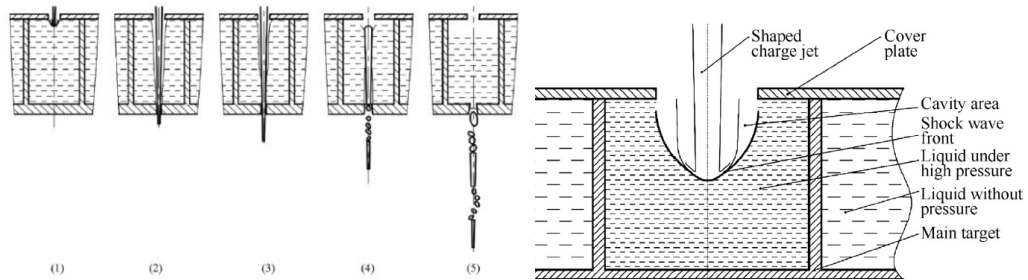


Figure 3.3 Steps of Penetration of the Shaped Charge Jet through a Liquid-Filled Structure [28]

Figure 3.3 shows the shaped charge jet penetration process through the filled-liquid structure target. The process is as follows:

- (1) The shaped charge jet penetrates the liquid that is inside the target's compartment. The shock wave is formed at the tip of the shaped charge jet. The shock wave translates through the liquid at an approximate velocity of 1500 m/s. A cavity is formed at the tip of the penetrating jet in the liquid.
- (2) The shock wave, which is translated through water, reflects from the side and bottom walls.
- (3) The shaped charge jet tip pierces the bottom plate of the main target body. The tip part of the shaped charge jet escapes before shock wave reflection from the sidewalls can reach the jet.
- (4) The reflected shock wave from the side and bottom walls comes across the jet's portions behind the tip. By applying pressure in the radial direction, it causes instabilities and particulations within the jet.

(6) The particulated shaped charge jet leaves the liquid-filled structure target. The disturbed portions lose their effectiveness in penetrating the witness target [28].

### 3.3 The Recent Research

In the reference [28], the liquid-filled target is comprised of several components: the main target body, a cover plate, a seal ring, and bolts. As shown in the left part of Figure 3.4, the main target body is made from #45 carbon steel with a minimum wall thickness of 5 mm between cavities. Water is injected into these cavities. The seal ring is placed in a groove to ensure a tight seal, and the cover plate, made of Q235 steel, is fastened to the main target body with screws.

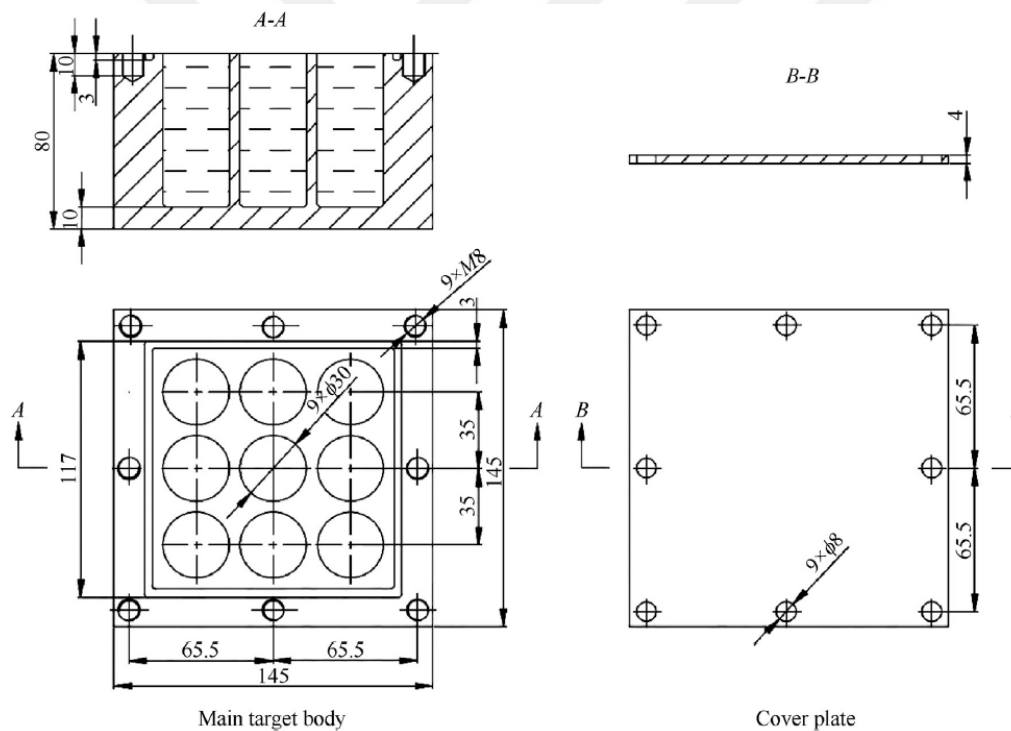


Figure 3.4 The Design of the Liquid-Filled Structure Armor [28]

Firstly, the  $\phi 56$  mm shaped charge is detonated at 80mm and 254mm standoff distances to witness target without liquid-structure armor. The penetration depths are given in Table 3.1. The witness target is made of #45 steel.

Table 3.1 The Penetration Depths without Liquid Structure Armor [28]

Results of the shaped charge performance experiment.

Number	Standoff/mm	Velocity of jet tip/(m·s <sup>-1</sup> )	DOP/mm
1	80	6510	199
2	80	6510	203
Average	80	6510	201
3	254	6510	254
4	254	6510	258
Average	254	6510	256

In the latter case, liquid-filled structure is placed between shaped charge and witness target as shown in Figure 3.5 below. The structure is placed at an 80 mm standoff distance, and the total gap between witness target and the shaped charge is 254 mm. The penetration depth results are as given in Table 3.2.

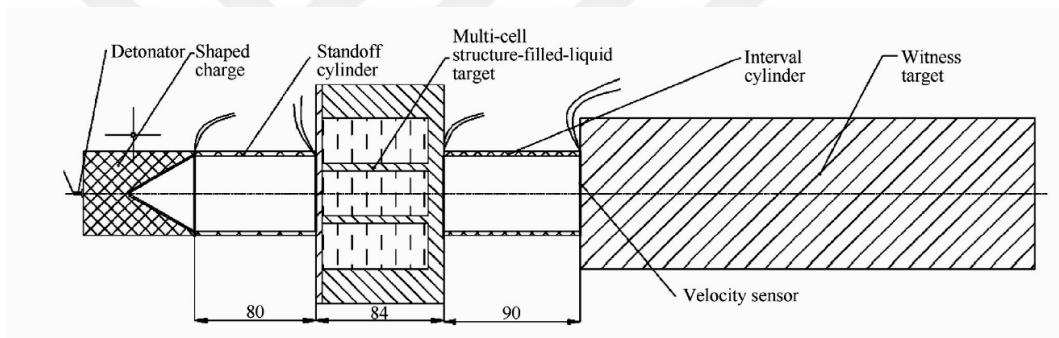


Figure 3.5 The Schematic Representation of the Liquid-Filled Structure, Shaped Charge Jet Penetration Experiment [28]

Table 3.2 The Penetration Depths with Liquid-Structure Armor [28]

Velocity of SCJ that penetrated the liquid-filled structure target and residual penetration.

Number	$v_{j0}/(\text{m}\cdot\text{s}^{-1})$	$v_{je}/(\text{m}\cdot\text{s}^{-1})$	Hour/mm
1	6510	5375.0	78.0
2	6510	5318.0	81.0
Average	6510	5346.5	79.5

Note:  $v_{j0}$  is the velocity of the SCJ tip,  $v_{je}$  is the velocity of the tip of the escaped SCJ, and  $h_r$  is the residual penetration.

In conclusion, the liquid-filled structure reduces penetration depth at the witness target from 199-256 mm to 78-81 mm, which is a remarkable effect.

In the reference [29], a liquid-filled structure similar to the previous research, consisting of a bulk steel plate with matrix of blind holes filled with liquid and closed with a steel front plate, is investigated at different obliquity angles. The design of the structure is as given in Figure 3.6 LH side. In this research, the materials of the main target body and the front plate are #45 and Q235 steels, respectively, and diesel oil is injected into the holes.

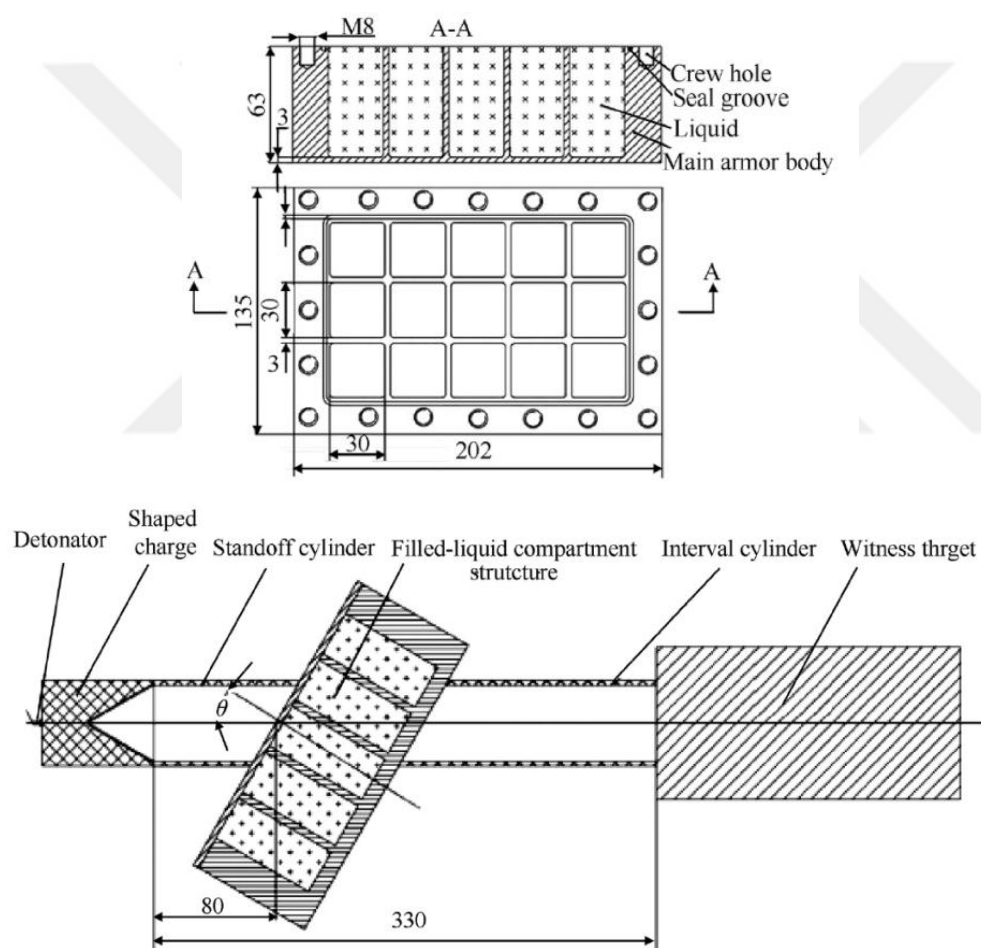


Figure 3.6 The Schematic Representation of Liquid Filled Structure, Shaped Charge Jet Penetration Experiment [29]

The liquid-filled compartment structure target is placed as shown in Figure 3.6. The standoff distance from the charge to the armor module is 80 mm. The impact angle (i.e., Nato angle)  $\theta$  is defined by the angle between the normal on the structure and the shotline of the shaped charge jet. The standoff from the base of the shaped charge to the witness target is 330 mm.

The liquid-filled structure and shaped charge jet interaction are the same as explained at the beginning. The shock waves reflecting from the bottom plate and compartment walls, as shown in Figure 3.7, disturb the jet. In this case, the liquid-filled structure has an inclination angle, and the shape charge jet needs to perforate more than one compartment wall which may affect penetration depth at the witness target.

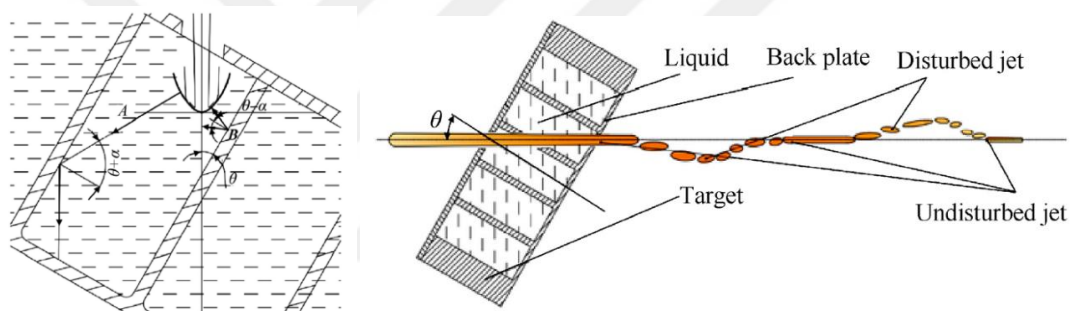


Figure 3.7 The Schematic of the Propagation Path of the Shock Wave (LH Side),  
The Representation of Liquid-Filled Structure Shaped Charge Jet Penetration  
Experiment [29]

The residual penetration and crater diameters in the witness target, as well as those of the front and back plates of the liquid-filled structure, were measured after each firing at various impact angles, as detailed in Table 3.3. The results indicate that the crater diameters ( $D_{ti}$  and  $D_{to}$ ) on the liquid-filled compartment target increase with the impact angle, whereas the crater diameter ( $D_{wi}$ ) of the witness target decreases as the impact angle rises. Additionally, the radial scatter of the particulated jet elements grows with the impact angle. Penetration depth into the witness target varies non-monotonically with impact angle, reaching a minimum at an impact angle of  $0^\circ$ .

Table 3.3 The Penetration Depths at Different Impact Angles [29]

Experimental results.

No.	$\theta/^\circ$	$P/\text{mm}$	$D_{wi}/\text{mm}$	$D_B/\text{mm}$	$D_{to}/\text{mm}$
1	0	59	18 × 24	21 × 21	103 × 42
2	0	62	18.5 × 24.5	20 × 21	98 × 42
3	20	108	15 × 15	16.5 × 26	108 × 53
4	20	116	16 × 10	22 × 22	112 × 55
5	30	89	14 × 10	24 × 20	125 × 60
6	30	83	15 × 9.5	21 × 22	122 × 63
7	45	69	18 × 21	18 × 21	136 × 55
8	45	64	18 × 25	18.5 × 24	134 × 53
9	60	76	10 × 16	55 × 25	149 × 42
10	60	77	10 × 16	54 × 23	143 × 42

In conclusion, the protection provided by the liquid-filled structure reaches its peak when the impact angle is at  $0^\circ$ , which is an unexpected result compared to conventional armor plates. This result is obtained even when the jet needs to penetrate more metal plates and liquids at higher angles, as shown in Figure 3.8, which may indicate that the structure material strength may not play a vital role in protection.

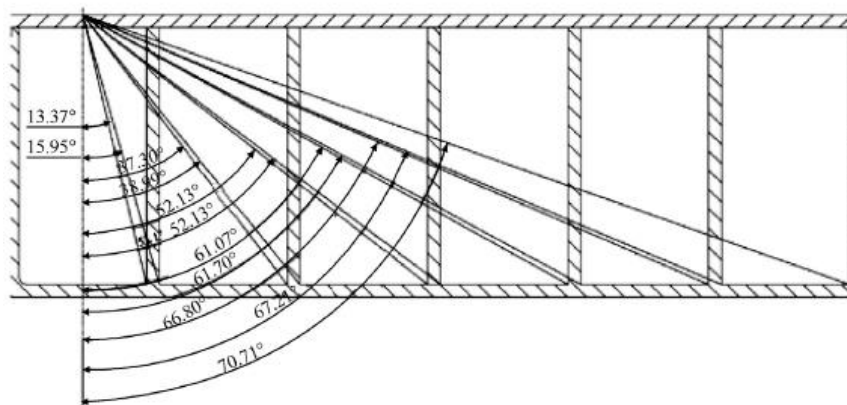


Figure 3.8 Penetration Channel Geometry of the Shaped Charge Jet Under Different Impact Angles [29]

In the reference [30], the effects of the chamber radius of the air-tight diesel fuel-filled structure, as shown in Figure 3.9, on the depth of penetration on the witness

plate are investigated. The  $\phi 56$  mm shaped charge is placed at an 80 mm standoff distance (from the base of the shaped charge) from diesel oil-filled structure and 330 mm from the witness plate.



Figure 3.9 Schematic View of Shock Wave Propagation in the Diesel Fuel (LH Side), Air-tight Diesel Fuel Filled Structure (Middle), Experimental Setup (RH Side) [30]

The analytical solutions show that the penetration depth increased with the increasing chamber radius. However, the penetration depth ceased to increase after the chamber radius exceeded a certain value, as shown in Figure 3.10 [30].

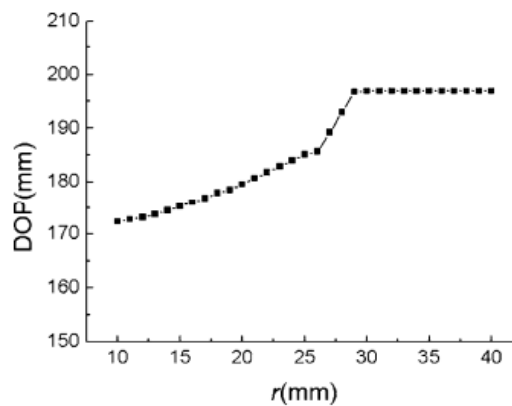


Figure 3.10 The Depth of Penetration – Chamber Radius Graph [30]

These research show that the steel chambers filled with liquids are effective against shaped charge jets by causing instability and particulation. A detailed test survey and numerical analysis supporting the test results are intended to show the protection capability of liquid-filled structures at different chamber parameters, such as different diameters, lengths, and sidewall thicknesses. It aims to provide knowledge to make an optimal armor design with minimum weight and maximum protection by using this concept, see if this mechanism works the same with different parameters, and make a detailed investigation on the particulation of shaped charge jets when penetrating through the liquid with the help of numerical analysis software.

### **3.4 The Scope of the Research**

The main objective of this study is to investigate the effects of water-filled chamber parameters on the penetration depth of the shape charge jet in the witness plate, as schematically shown in Figure 3.11. The numerical simulations that use time-dependent, explicit FEM are conducted in order to see how changing parameters affect the resultant depth of penetration (DOP). The numerical simulation results are correlated with tests. The parameters to be tested are given in the list below:

- Chamber diameter ( $d$ )
- Depth of the liquid chamber ( $L$ )
- Sidewall thickness ( $t_w$ )

The rest of the parameters, such as standoff distances,  $S$  and  $S_1$ , upper and lower plate thicknesses,  $t_p$  and  $t_b$ , and the munition (shaped charge) parameters, are kept constant.

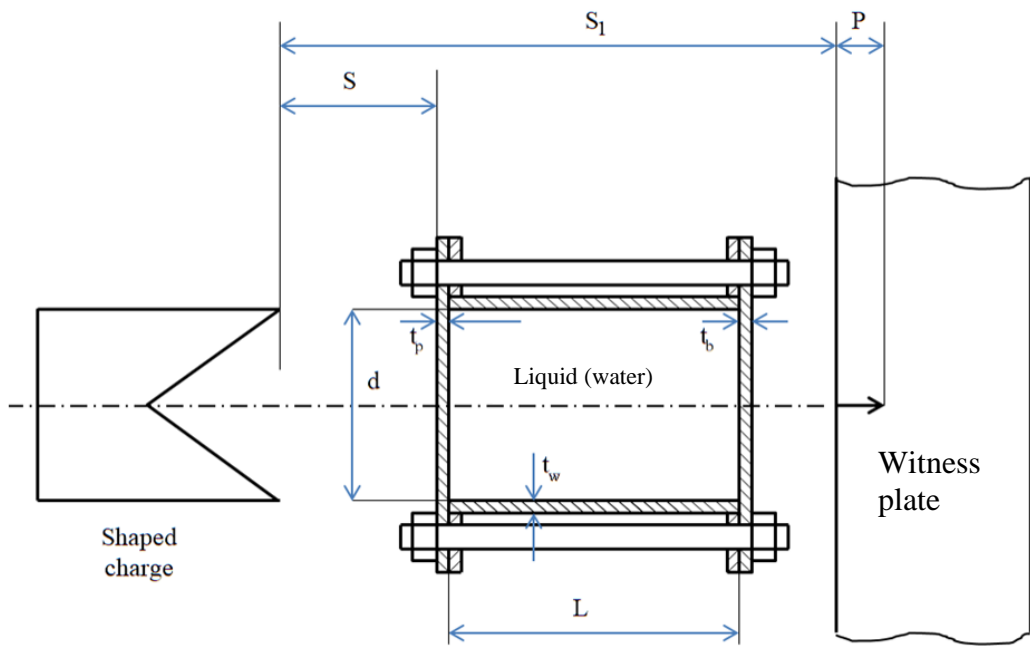


Figure 3.11 The Schematic View of the Experimental Setup



## CHAPTER 4

### NUMERICAL ANALYSIS

#### 4.1 The Geometry and the Parameters of the Shaped Charge

M85 bomblets are used in this research, as shown in Figure 4.1. The semi-product is used in the tests; the fuse assembly (a trigger mechanism that is activated when the munition impacts the ground) and ribbon are not installed. Thus, the munition can be detonated at a standalone position with a detonator. It has a 42.1 mm outer diameter and a 62 mm total length. 14.3 mm gap between the cone edge and open end provides the standoff distance to the munition in normal operation.



Figure 4.1 The Cross Section of M85 Bomblet [31]

The available alternatives to this shaped charge munition have much larger charge diameters and penetration capabilities, which increase the test setup costs and reduce the chances of conducting a large number of tests in a limited interval of time. The test survey was done with the support of the company Mechanical and Chemical Industry Corporation (MKE), which provided the munition, test area, and personnel to conduct the tests.

In the numerical analysis, the geometry of the casing is simplified so as to be cylindrical with no step at the upper corner. The casing is assumed to be made of a single piece of 4140 steel. The liner is oxygen-free high thermal conductivity copper (OFHC). The liner geometry is not a simple cone. Thus, an RTV2 mold silicone is used to obtain its geometry. The cone shape is molded with silicone rubber. This molded rubber geometry is 3D scanned and modeled to be used in numerical analysis, as shown in Figure 4.2. The copper liner thickness is taken as 0.4 mm. The total wall thickness is taken as 4.7 mm and is assumed to be constant at all surfaces. The spaces between the copper liner and casing are filled with RDX explosive. The detonation starts from the center of the circular surface where the booster is located.

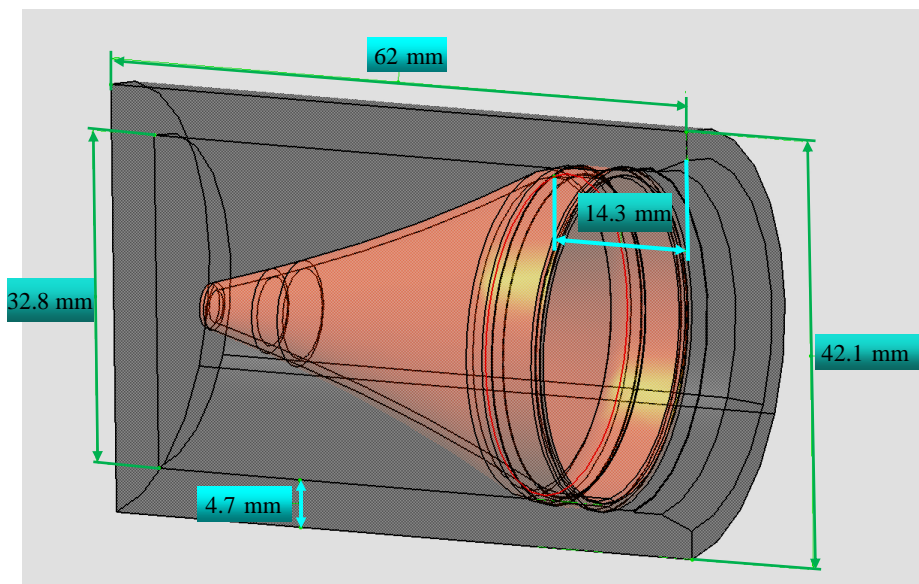


Figure 4.2 The Simplified 3D Model Geometry of the Shaped Charge

## 4.2 Modeling and Material Parameters

The geometric models of the munition and the test setup were created with computer-aided design software (Figure 4.2 & Figure 4.3). The 3D model of the test setup was transferred to pre-processing software to create the finite element model. The finite element model was transferred to LS-prepost (Figure 4.4) in order to define the ALE solution algorithm, constraints, equation of states, and material models. 2D MMALE (Multi-Material Arbitrary Lagrange Euler) code was implemented by using LS-DYNA software. Then, the analysis is carried out with the LS-DYNA solver. Wu et al., 2019 [32] show that the ALE algorithm gives accurate results regarding the impact of a shaped charge jet on ductile materials, such as medium carbon steel.

The CAD and FEM models of the test setup are shown in Figure 4.3 and Figure 4.4. 0.5 mm square quad meshes are used apart from the liner and the zones that are close to the liner. 0.4 mm thick liner is divided into three layers of mesh. Thus, mesh sizes are reduced to 0.13 mm around the liner. The water is assumed to be an inviscid fluid ( $\mu=0$ ). There are also assumed to be no phase changes within the water (due to cavitation or evaporation).

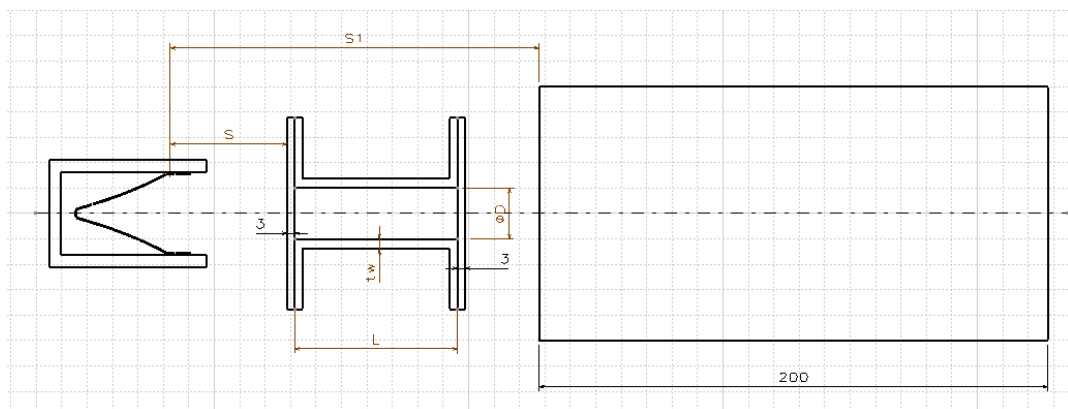


Figure 4.3 The Dimensions of the Setup: The Munition is at the LH Side, the Water-filled Chamber is in the Middle, the Target is at the RH Side

The standoff distances  $S$  (distance between SC and Chamber), and  $S_1$  (distance between SC and witness plate) values are constant at each case. Their proportions are taken the same as the case in the article [28], which are  $1.43 \times \text{Charge Diameter (CD)} = 46 \text{ mm}$  for  $S$  and  $4.53 \times \text{CD} = 145 \text{ mm}$  for  $S_1$ . The charge diameter (CD) is taken as 32 mm.

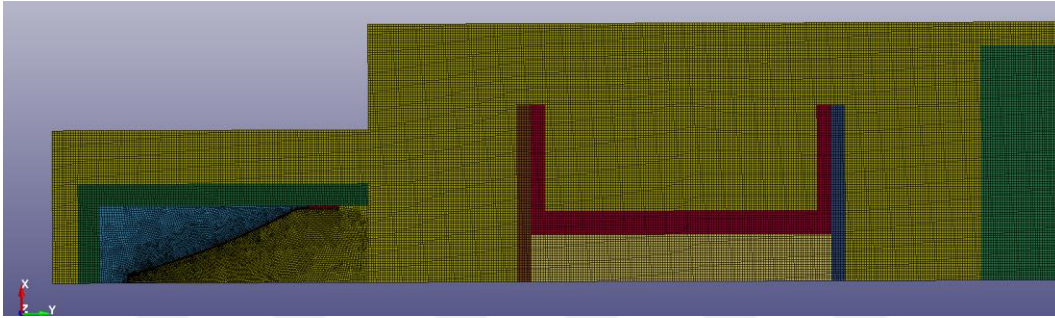


Figure 4.4 2D Axisymmetric ALE FEM Model

The Null material model is used to define the behavior of fluid materials, such as water and air. In LS-DYNA, the Null material model (MAT\_NULL, Material Type 009) is primarily used to model materials that do not have any specific material stiffness, such as fluids, gases, or void regions, where structural strength or resistance to deformation is not a concern. It also assumes the material has no resistance to shear forces. Therefore, it does not compute any shear stresses, making it ideal for materials that behave like fluids or gases, where shear resistance is negligible. However, this model can still handle pressure transmission if coupled with other elements, using Equation of State (EOS) models, which define the pressure-volume relationship. The Null material is often employed with an EOS to represent interactions like explosions and fluid-structure interaction [14], [33], [34].

The key parameters for the Null model include density and damping coefficients. Since the Null material itself does not carry any mechanical properties, its utility lies in its ability to allow LS-DYNA to simulate the effects of phenomena like fluid flow or large deformations without causing numerical instabilities in regions where material stiffness is not required, such as surrounding elements subjected to high-pressure conditions in fluid simulations. This model is essential in problems involving multi-material interactions where different constitutive behaviors need to be represented without stiffness and yield stress. In the case of dynamic viscosity applied, the governing equations are as follows [14], [33], [34]:

$$\sigma_{ij} = 2\mu\dot{\epsilon}_{ij} \quad (48)$$

$\dot{\epsilon}_{ij}$  is the deviatoric strain rate and  $\mu$  is the dynamic viscosity.

**Mesh Convergence Analysis** ensures that the numerical solution of a problem becomes stable and accurate as the mesh is refined. It occurs when further mesh refinement leads to negligible changes in the solution, indicating that the result is close to the true solution. This analysis is applied to the FEM model of the test setup that is mentioned above to check the selected element size. The chamber length (L) and diameter (D) are 64mm and 20 mm, respectively.

The mesh size around the munition is kept constant since these elements are fine enough (0.13mm), and smaller sizes require smaller time steps, which cause an unfeasibly long analysis time for a home computer.

The mesh convergence evaluation criterion is the depth of penetration (DOP) and checked for the mesh sizes, as shown in Table 4.1 and Figure 4.5.

Table 4.1 The Resultant DOP in the Witness Target with Different Element Sizes when  $D=20$  mm,  $L=64$  mm, and  $t_w=5$  mm

Element Size [mm]	Depth of Penetration in the Witness Target (DOP) [mm]
1	19
0.7	45
0.5	57.5
0.4	59

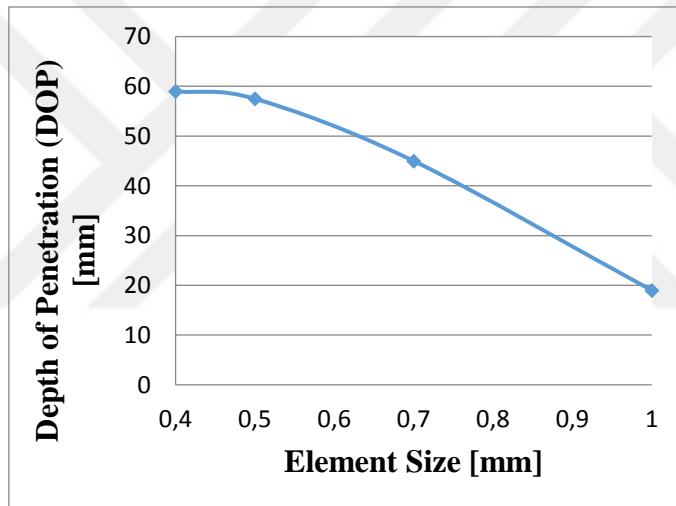


Figure 4.5 Element Size vs DOP when  $D=20$  mm,  $L=64$  mm, and  $t_w=5$  mm

The mesh convergence study reveals that a 0.5 mm element size is very near the optimal size. Since the effect of using finer meshes on DOP is minor. They cause an increase in the computation times due to the increased number of elements.

**The time step size** in LS-DYNA explicit simulations is determined by the Courant-Friedrichs-Lewy (CFL) condition, which ensures numerical stability. The time step is influenced by the size of the smallest element in the mesh and the speed of wave propagation through the material (sound speed).

The CFL condition states that, for a stable numerical solution, the time step  $\Delta t$  must be small enough so that waves propagating through the domain do not travel more than one element or grid cell in a single time step. Mathematically, the CFL condition is expressed as:

$$\Delta t \leq \frac{h}{c} \quad (49)$$

Where:

- $\Delta t$  is the time step.
- $h$  is the characteristic element size or the distance between nodes
- $c$  is the wave propagation speed (the speed of sound).

The CFL condition ensures that during each time step, the stress waves travel only within a small region of the mesh, preventing instabilities that could occur if the wave travels too far in one step. To sum up, it prevents the numerical solution from leaping over elements or grid cells, which would lead to inaccuracies and numerical instabilities.

In LS-DYNA, the critical time step is calculated for each element using  $\Delta t_e = h / c$ . Then, the next time step of the calculation is determined by the smallest element such that,

$$\Delta t^{n+1} = a \cdot \min\{\Delta t_1, \Delta t_2, \Delta t_3, \dots, \Delta t_N\} \quad (50)$$

Where  $N$  is the number of elements, there is a scale factor “ $a$ ” to provide stability. This factor is known as the Time Step Scale Factor (TSSFAC) and is typically set to 0.90 as default. In the case of a blast loading, this recommended default value is lowered to 0.67. Infact, having a lower value for this factor increases the accuracy of the solution. Within the context of this study, the shaped charge jet has a velocity much higher than the speed of sound of all materials. It is likely that due to this reason, the value of this factor is reduced to 0.04 so that the analysis can continue without a stop due to errors caused by instability [35], [36].

The equation of state (EOS) and material flow parameters used in the numerical simulations are given as follows:

Mie-Gruneisen EOS, as stated in Equation 34 in Section 2.3.1, is used mainly for solid materials such as copper, steel, and aluminum [29]. Zhang et al., 2017 [37] and Steinberg, 1987 [38] claim that Mie-Gruneisen EOS is also applicable to water. The Mie-Gruneisen EOS parameters of the copper liner (oxygen-free high conductivity), upper and lower caps (1006), steel casing (4140), witness plate and chamber (4340), and water that are used in the survey are given in Table 4.2.

Table 4.2 Mie-Gruneisen EOS Parameters of Copper Liner, Steel Casing, Upper and Lower Caps, Water, Chamber and Witness Plate [21], [39], [40]

	Intercept $C_0$ (m/s)	$S_1$	$S_2$	$S_3$	Gruneisen Parameter $\gamma_0$	b	E (J/kg)
Copper	3940	1.49	0.6	0	1.99	0.47	0
4340 steel	4578	1.33	0	0	1.67	0	0
4140 steel*	4578	1.33	0	0	1.67	0	0
1006 steel	4569	1.49	0	0	2.17	0.46	0
Water	1480	2.56	1.986	1.2268	0.5	0	0

\*The steel materials with similar alloys are assumed to have the same EOS parameters.

The JWL equation of state, as stated in Equation 36, has been used to accurately describe the pressure-volume-energy behavior of the detonation products of explosives in metal acceleration applications. The JWL EOS parameters of RDX explosive are given in Table 4.3.

Table 4.3 JWL EOS Parameters of RDX Explosive [41]

	$\rho$ [kg/m <sup>3</sup> ]	A [GPa]	B [GPa]	R <sub>1</sub>	R <sub>2</sub>	$\omega$	E [J/mm <sup>3</sup> ]
RDX	1836	801.8	52.64	5	2.1	0.340	8.5

The linear polynomial equation of state, as stated in Equation 37, is used to model gases [19]. The linear polynomial EOS parameters of air are given in Table 4.4. The parameters, which are not mentioned are equal to zero ( $C_{0,1,2,3,6} = 0$ ).

Table 4.4 Linear Polynomial EOS Parameters for the Air [21]

	$\rho$ [kg/m <sup>3</sup> ]	$\gamma$	C <sub>4</sub>	C <sub>5</sub>	Energy per unit volume E [J/m <sup>3</sup> ]
Air	1.025	1.403	0.403	0.403	2.5 x 10 <sup>5</sup>

The Johnson-Cook material model is a function of Von Mises tensile flow stress, which is characterized by strain hardening, strain rate hardening, and thermal softening. Johnson-Cook's formulation of the flow stress is expressed by Equation 38. Johnson-Cook flow parameters of the copper liner, steel casing, and steel target that are used in the survey are given in Table 4.5. Johnson-Cook fracture parameters of the copper liner and steel target are given in Table 4.6.

Table 4.5 Johnson Cook Flow Parameters of the Copper Liner, Steel Casing, Upper and Lower Caps, Chamber and Witness Plate [24], [42]

	$\rho$ [kg/m <sup>3</sup> ]	A [MPa] Yield Strength	B [MPa] Hardening Modulus	n Hardening Coef.	c Strain Rate Sensitivity Coef.	m Thermal Softening Coef.	T <sub>melt</sub> [°K]	T <sub>room</sub> [°K]
Copper	8960	90	292	0.31	0.025	1.09	1356	293
4340 Steel	7830	792	510	0.26	0.014	1.03	1793	293
1006 Steel	7890	350	275	0.36	0.022	1.00	1811	293
4140 Steel	7850	1450	910	0.45	0.034	0.328	1809	293

Table 4.6 Johnson Cook Fracture Parameters of the Copper Liner, Chamber and Witness Plate [43]

	D <sub>1</sub>	D <sub>2</sub>	D <sub>3</sub>	D <sub>4</sub>	D <sub>5</sub>
Copper	0.54	4.89	-3.03	0.014	1.12
4340 Steel	0.05	3.44	-2.12	0.002	0.61

### 4.3 Simulation of Standalone Shaped Charge Jet Formation

The jet formation is observed before the impact analysis to see if the jet is formed properly. At 24  $\mu$ s instant after the initiation of the detonation, a thin jet is created with a raindrop-shaped tip, as shown in Figure 4.6. The velocity gradient is shown in Figure 4.7.

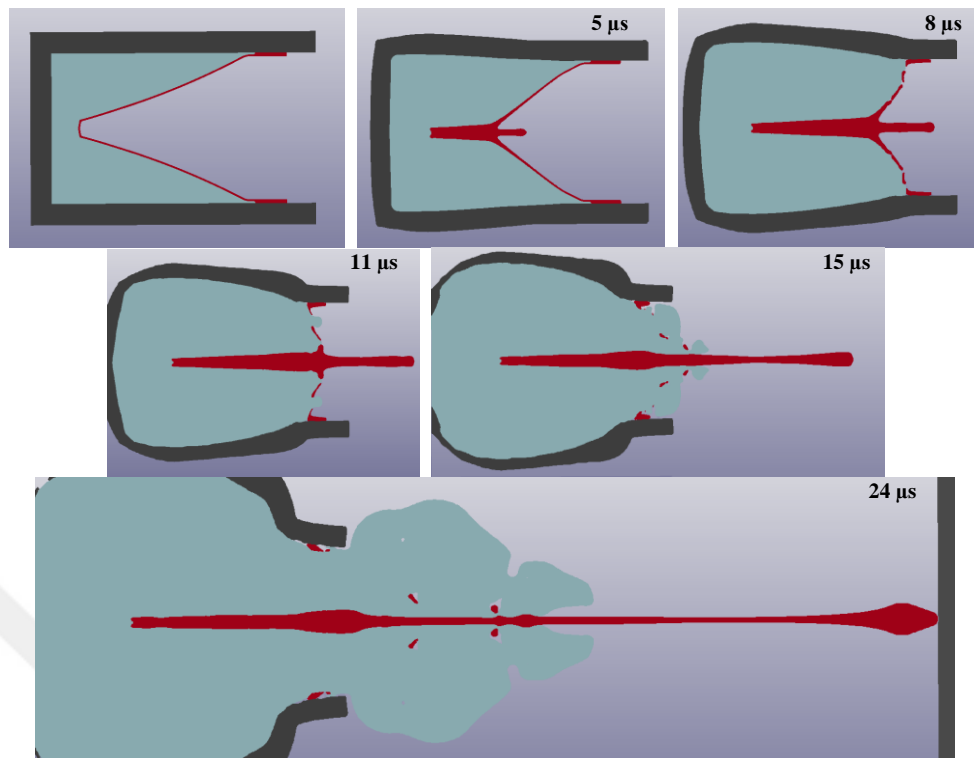


Figure 4.6 The Formation of SC Jet; Copper is Shown in Red, Steel Casing and Target Material is Dark Grey, and Explosive/Detonation Products are Shown in Turquoise

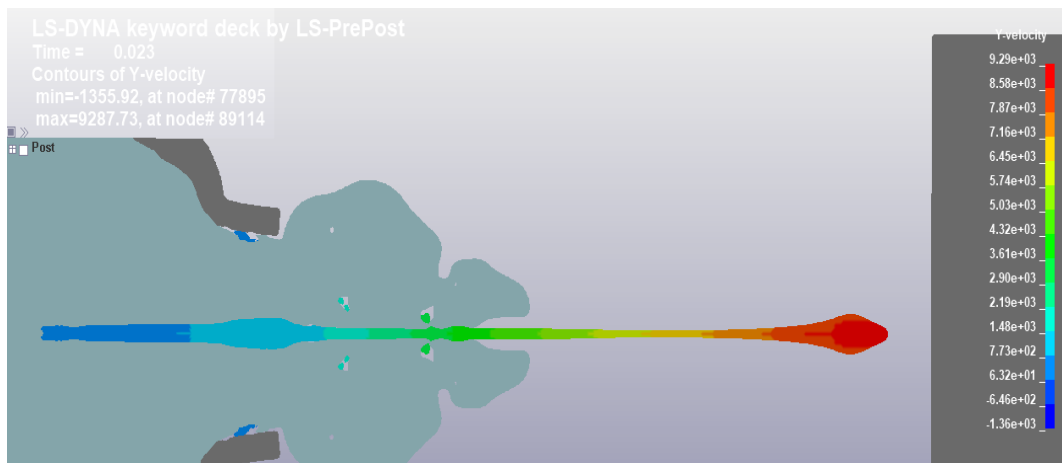


Figure 4.7 The Velocity Gradient (m/s) of the Jet in Axial Direction; The Jet Tip Velocity Reaches up to 9.3 km/s

The variable velocity of the liner particles due to the decreasing thickness of the explosive in the steel casing creates a jet with a high tip and low tail velocity. It constantly stretches, as shown in Figure 4.6 and Figure 4.7. The simulation result of a jet formation matches with the variable collapse velocity theory defined by PER theory, explained in Chapter 1. The jet tip velocity can reach the magnitude of 9.3 km/s, which is close to the value given by Walters et al.,1989 [1] that claims the jet tip velocity can exceed 10 km/s. Thus, the jet that is created in the simulation matches with the theory of the shaped charge jet formation. As a next step, its collision with the standalone witness target and the combination of water-filled targets with different parameters can be simulated.

## CHAPTER 5

### TEST SETUP

#### 5.1 The Design of the Test Setup

The test setup comprises the munition, alignment part, water-filled chamber, and a target, as shown in Figure 5.1. All the chamber and the witness targets were made of the same Ø110 mm diameter 4340 steel rod during the whole survey. An alignment part is placed between the munition and the chamber to maintain the concentricity and a certain distance between these two components. The open end of the alignment part is designed to be clearance fit with the munition. A maximum 0.2 mm gap between the munition's outer surface and the alignment part's inner surface is filled with sellotape that is wrapped around the munition so that these parts can be precisely centered. A steel pipe with a 4 mm wall thickness provides the gap between the chamber and the target. All the test parts, including the chamber, pipe, target, and alignment parts, are machined for good geometric accuracy instead of welding ( $\pm 0.2$  mm dimensional accuracy and Ra 3.2  $\mu\text{m}$  surface roughness). Four Ø6 mm holes on the flanges of alignment parts and chambers are drilled with a CNC vertical machining center to obtain the highest concentricity between the alignment part and the chamber at reasonable costs. The upper and lower caps are made of 3 mm thick St37 sheet metal with 0.06% carbon content, which is the equivalent of 1006 steel, and are cut as square plates (97 mm x 97 mm) from the same sheet and kept as standard whatever the test parameters are selected. Pure water is taken from the same bottle and has exactly the same properties throughout the survey. The rubber material is used as gaskets between the upper and lower caps and the chamber. Four M6 steel rods, cut from Standard 1 m stud bolts, fix all alignment parts, upper and lower caps, and the chamber. These

parts are as long as the chamber itself so that they can absorb the shock load and keep the chamber components together without failure.

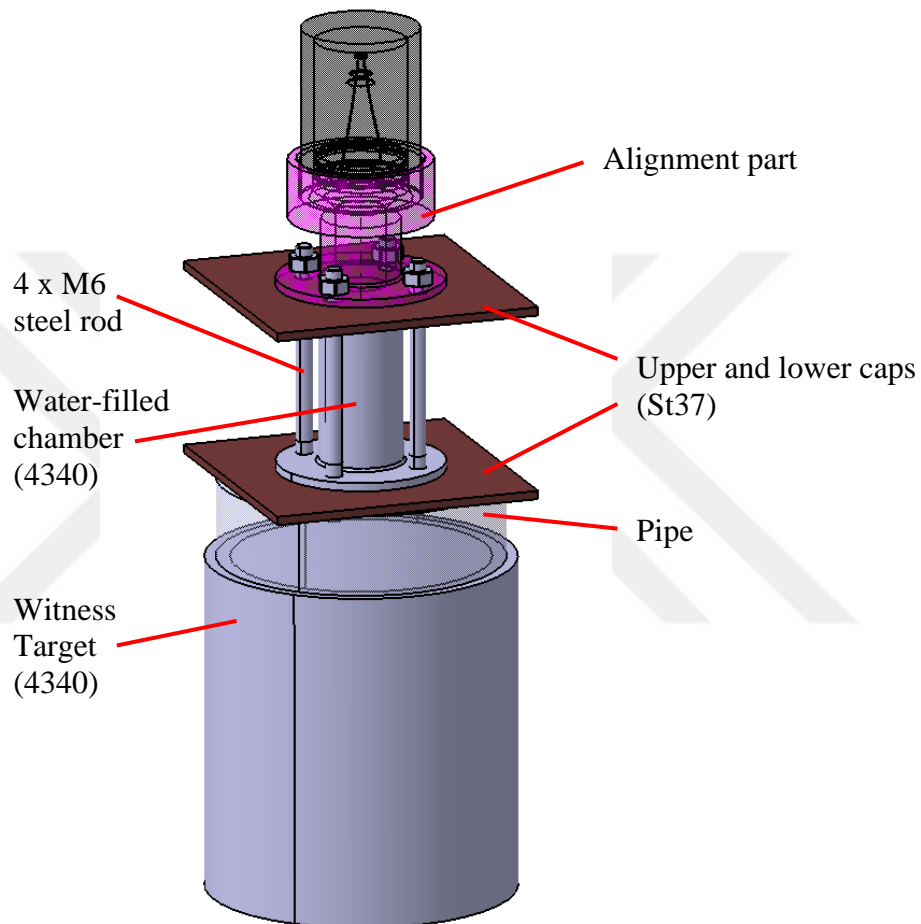


Figure 5.1 The Design of the Test Setup

The tests without chamber and without water (water-free chamber) are done with sheet plates and spacer pipes, as shown in Figure 5.2. The distances between the munition and the target (SO distance), munition, and upper caps are the same as those in water-filled chamber experiments (Figure 5.3) and are always kept constant. The water-free chamber test is conducted for a length of only 64 mm.



Figure 5.2 Test Setups that Represent the Cases without Chamber (LH Side), with Chamber w/o Water (RH Side)



Figure 5.3 Test Setups with  $\text{\O}50$  mm Diameter and 64 mm Length Chamber (LH Side), with  $\text{\O}20$  mm Diameter and 64 mm Length Chamber (RH Side)



## CHAPTER 6

### RESULTS AND EVALUATION

The effects of different diameter, length, and sidewall thickness parameters are investigated with simulations and tests. The simulation and test results for different lengths, diameters and sidewall thicknesses are shown in Table 6.1, Table 6.2, and Table 6.3 respectively. The graphical demonstrations are shown in Figure 6.1, Figure 6.14, and Figure 6.18.

Table 6.1 Effect of Chamber Diameter and Length on Penetration Depth  
Simulation Results

Simulation Results (Side wall thickness $t_w = 5$ mm)		Diameter (D) [mm]								w/o chamber	with chamber, w/o water	
		10	15	20	24	27	35	43	50			70
Length (L) [mm]	32			73							118	97
	48			68								98
	64	67	59	57.5	63.5	65.5	68	71.5	77	76		102
	88			66								108

Table 6.2 Effect of Chamber Diameter and Length on Penetration Depth Test Results

Test Results (Side wall thickness $t_w = 5$ mm)		Diameter (D) [mm]					w/o chamber	with chamber w/o water
		10	20	35	50	70		
Length (L) [mm]	32		59 (55.7, 62, 57)				109 (125, 93)	
	48		63.5 (66.9, 60.1, 63)					
	64	62, 55*	49 (45, 48, 54)	70.5 (65.5, 75,5)	76.7 (98, 55.3)	75		95 (104, 86)
	88		57,7					

The values are averages of the test results that are given in paranthesis.

\*The test is re-done with 15 mm sidewalled chamber, since the chamber fails with 5 mm sidewall thickness.

### 6.1 Effect of Chamber Diameter (D) on Depth of Penetration

Firstly, the effect of the chamber diameter is evaluated when the other parameters are kept constant (except for  $D=10$  mm due to the explosion of the chamber). Figure 6.1 shows the depth of penetration in witness targets versus different diameters of water-filled chambers, which are shown in Figure 6.2. The cases of the water-free chamber and without chamber (Figure 5.2) are also shown in the same graph for comparison. The test results (DOP) are determined by facing the witness target on a lathe from the bottom surface (opposite the shot surface). The machining stops when the copper liner or the hole is reached. Figure 6.3 and Figure 6.4 below show the SC jet penetrated test setups with water-filled chambers that have different diameters, however, with standard length and sidewall thicknesses, 64 mm and 5 mm, respectively (except second test with 10 mm chamber diameter, but 15 mm sidewall thickness in Figure 6.4 LH side). The remaining heights of the

witness plates indicate the penetration of the shaped charge jet into these targets after penetrating the chamber above the witness plate.

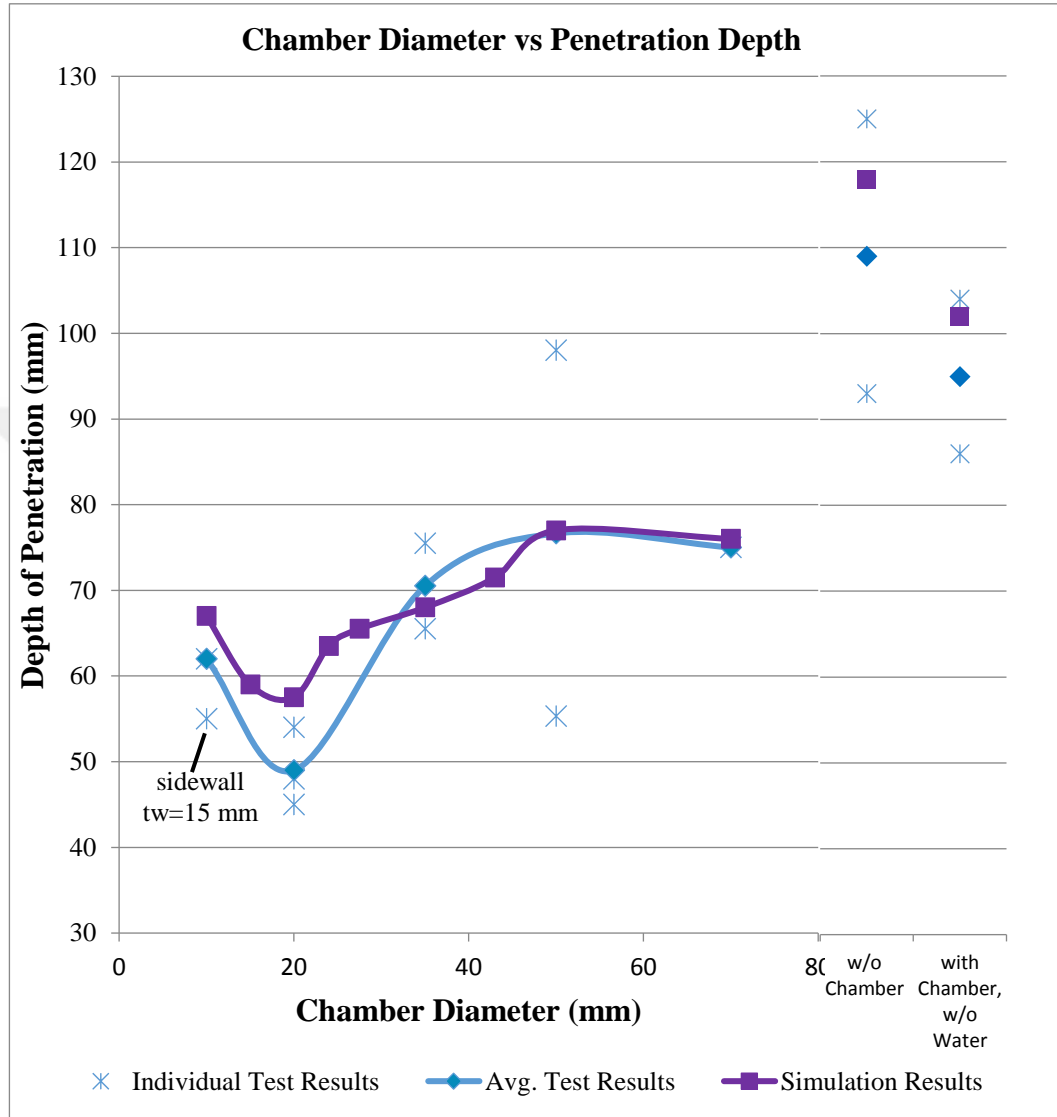


Figure 6.1 Depth of Penetration vs Diameter (D) Graph when the Chamber Length (L) is 64 mm and the Sidewall Thickness ( $t_w$ ) is 5 mm



Figure 6.2 Test Setups with  $\text{Ø}10$ , 20, 35, 50 mm Diameter Chambers (LH Side Picture),  $\text{Ø}10$  Diameter, 15 mm Sidewall Chamber and a  $\text{Ø}70$  mm Diameter Chamber (RH Side Picture) from Left to Right, Respectively with a Standard 5 mm Sidewall Thickness (Except Mentioned) and 64 mm Length

The number of tests for each parameter varies between one and three. (For instance, one for  $D=10$  mm –for both sidewall values-, three for  $D=20$  mm, two for  $D=35$  mm, two for  $D=50$  mm, and one for  $D=70$  mm). Due to the non-precise nature of the explosion process, up to about 20% deviation is expected to occur between the maximum and minimum values of the results of the same parameter. That deviation may also increase due to environmental factors, such as the munitions being kept for many years. Thus, five or more tests are ideally required to obtain reliable results. However, doing so many tests is too costly and not feasible due to the availability of the test facility. The numerical simulations are used to support the test results. If both the test average and simulation results are consistent within about 10% deviation, no more tests are done for this parameter, and available resources are used for the other parameters, which have inconsistencies between the test average and the simulation result.



Figure 6.3 Test Results with Different Diameters;  $\text{\O}10$  mm, 20 mm, 35 mm and 50 mm, the DOP of the Witness Targets (the Height of the Machined Targets from the Bottom) are 62 mm, 48 mm, 75.5 mm, 98 mm from Left to Right, Respectively



Figure 6.4 Test Results with Different Diameters;  $\text{\O}10$  mm (15 mm sidewall thickness), 20 mm, 50 mm and 70 mm, the DOP of the Witness Targets (the Height of the Machined Target from the Bottom) are 55 mm, 48 mm, 55.3 mm, 75 mm from Left to Right, Respectively

At large diameters such as 35 mm and 70 mm, in the cases without chamber and chamber without water, the average of the test results matches well with numerical analysis (less than a 10% deviation). Test results without chamber, which are 125 mm and 93 mm, also match well with King et al. [31], who claim the munition is capable of penetrating 100-120 mm steel armor. At 50 mm diameter, the test average is also very close to the simulation result. However, the scatter of the test results is relatively high, such as 53 and 98 mm. The test results at small diameters, such as  $D=10$  mm and 20 mm, tend to be lower than the simulation results. That deviation reaches up to 15% at  $D=20$  mm and is thought to occur due to very tiny non-concentricity (less than 1 mm) between the munition and chamber, which is caused by geometric inaccuracies of the test setup. While the jet is passing through the chamber, the pressure wave reflections, which are mentioned in the preceding sections, are not returning back to the jet with a perfect balance as it is simulated. This imbalance is causing the jet material to spread sideways, as can also be realized from the bottom surface of the  $\text{Ø}20$  mm chamber, which is covered with copper particles, as shown in Figure 6.3 and Figure 6.4, second from the left, and causing the DOP to be lower than expected from simulations. This effect becomes much more obvious at this diameter, which causes more particulation than other parameters.

The optimum value for the chamber diameter to minimize the depth of penetration is 20 mm, as shown in Figure 6.1. When the diameter increases from 20 to 50 mm, the effect of the pressure wave reflections in the chamber diminishes gradually and remains constant when it is greater than 50 mm. There is a transition region between these diameter values. As the chamber diameter increases from 20 to 50 mm, the longer section of the fastest and the most effective part of the jet leaves the chamber unharmed since the disturbed region of the jet gradually shifts backward (Figure 6.5). The pressure wave reflections affect the medium velocity regions (between 2.8 - 4 km/s) in the middle of the jet with less disturbance and particulations compared to lower-chamber diameters such as 20 and 15 mm. Thus, the jet's penetration capability on the witness plate increases.

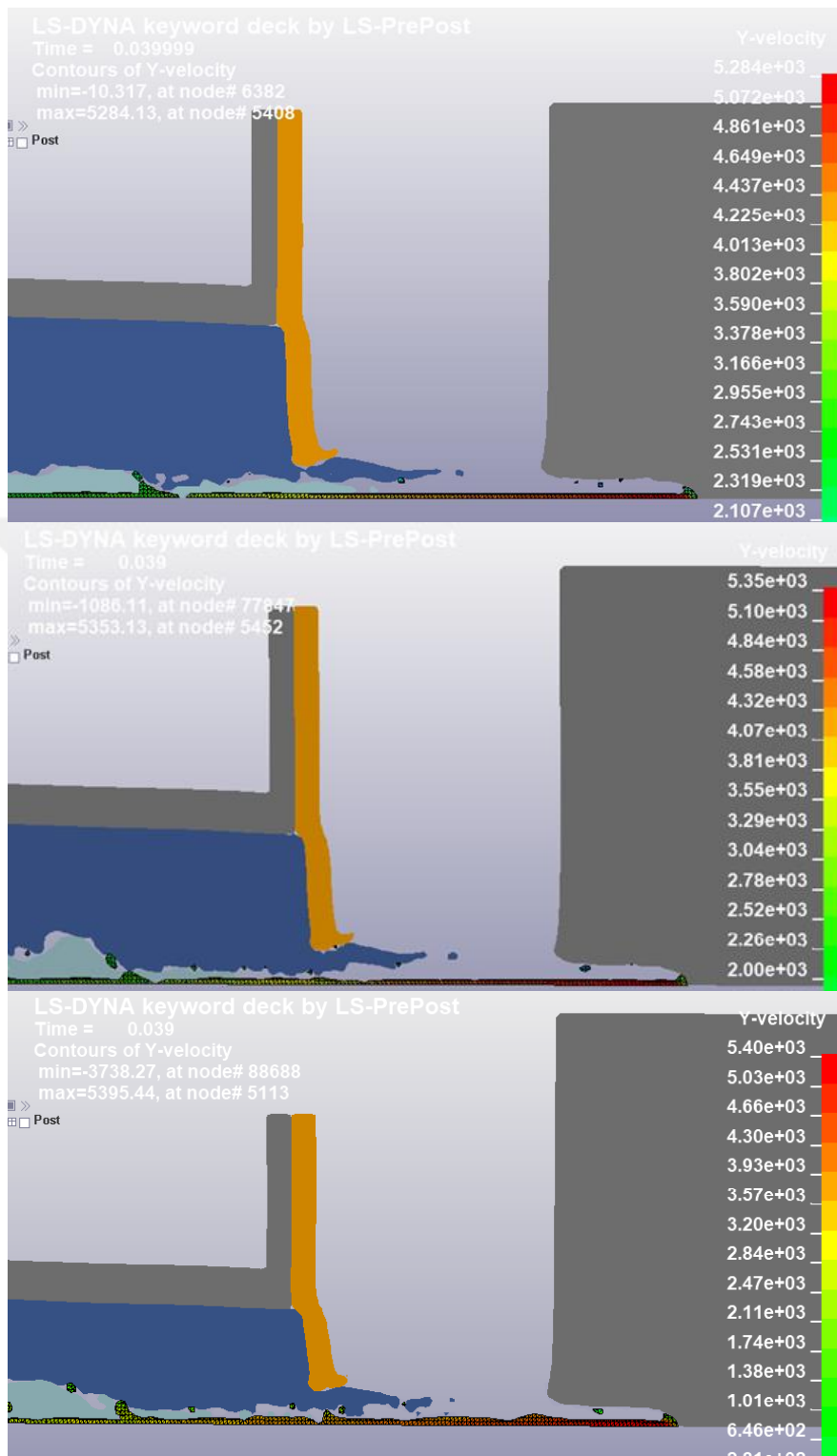


Figure 6.5 The Jet Velocity Distribution (m/s) and the Disturbances Created on Jets Leaving D=43 mm (Upper), D=35 mm (Middle) and D=27 mm (Lower) Chambers

The reduction of diameter from 20 to 10 mm also increases the penetration depth of the copper jet. The failure/explosion of the chamber occurs with the pressurized water created at the jet tip, as shown in Figure 6.6 LH side. The simulation and the test are done for the D=10 mm chamber when the wall thickness is increased to 15 mm (Figure 6.6 RH side) to see if lower DOP can be obtained without failure of the chamber. The simulation results dropped from 67 to 61 mm. The test result dropped from 62 to 55 mm, which is closer to the results for D=20 mm (57.5 mm simulation, 49 mm test average results). However, the test and simulation results for D=10 mm are still slightly higher than those for D=20 mm, even when the sidewall thickness is very high (Figure 6.1).



Figure 6.6 Test Specimens and Witness Plates for D=10 mm Chamber Diameter,  $t_w=5$  mm Sidewall Thickness (LH Side),  $t_w=15$  mm (RH Side)

The effect of the wave reflections on the jet disappears at large diameters such as  $D=50$  and  $70$  mm since it takes such a long time for the reflecting wave to come back and hit the jet, as shown in Figure 6.7. In the meantime, the fast and the effective part of the jet exits from the chamber without getting particulated.

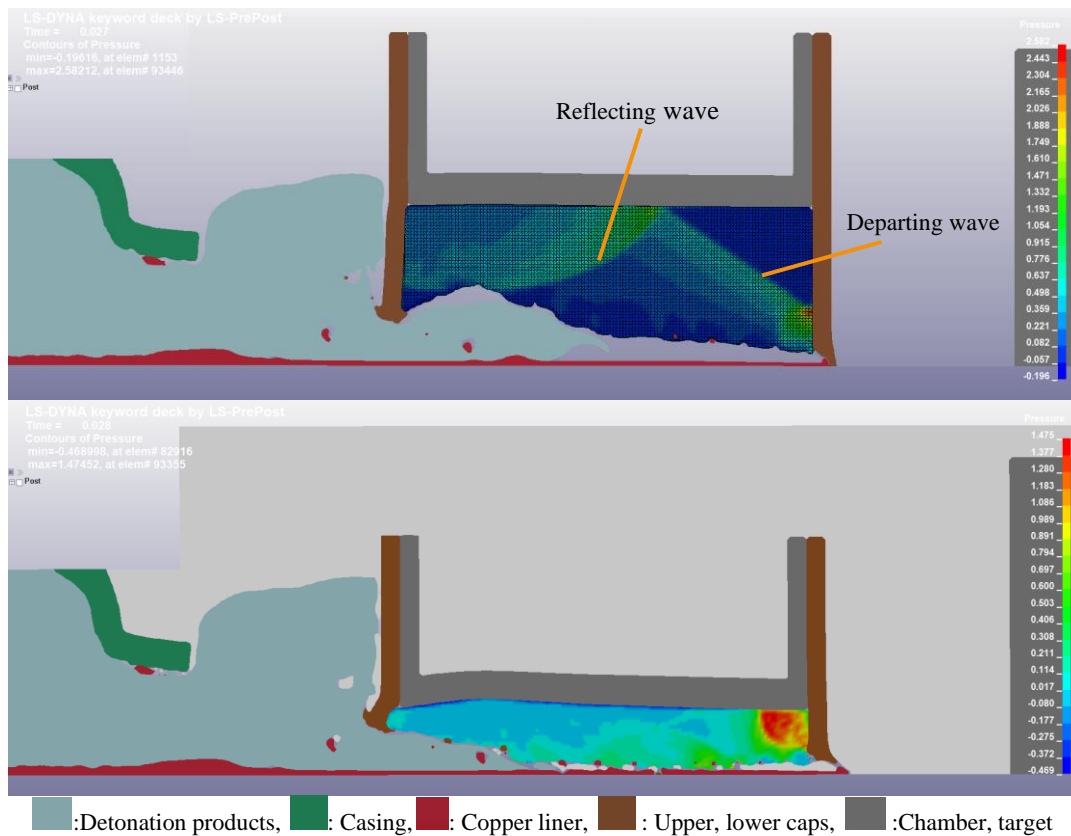


Figure 6.7 The Reflecting Pressure Waves (GPa) in Water at 27, 28 $\mu$ s after Detonation when the Chamber Diameters  $D=50$  (Upper Figure), 20 mm (Lower Figure)

With small diameters such as  $D=20$  mm, pressure wave reflections from the chamber bottom and sidewalls can reach the jet and cause the particulation after the tip of the jet leaves the chamber, as shown in Figure 6.8. However, there is no particulation in 50 mm diameter chamber. Besides, at large diameters, the detonation gases also leak through the open hole made by the jet and create an additional protective layer before the reflecting wave reaches the jet.

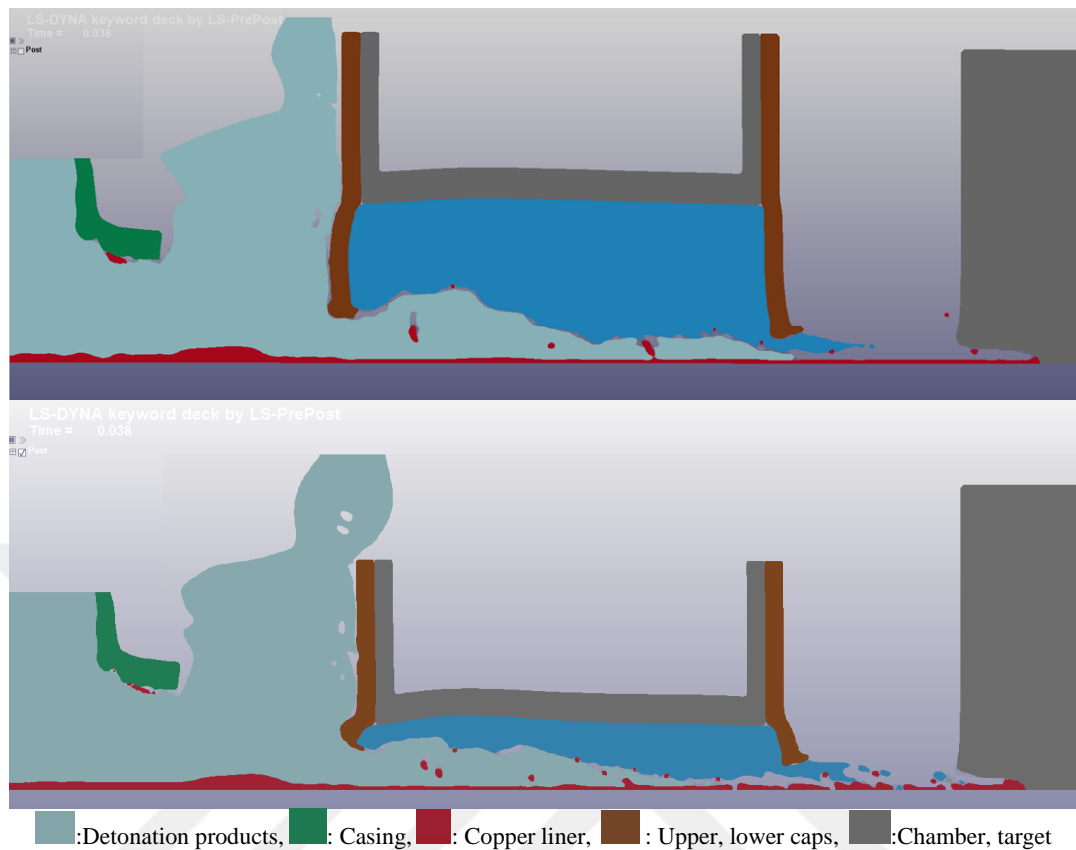


Figure 6.8 The Difference of Jet Particulations between 20 mm (Lower Figure) and 50 mm (Upper Figure) Diameter Chambers ( $L=64$  mm) at Instance  $t=38\mu\text{s}$  after the Start of Detonation

When the diameter is small, such as 10 mm, the jet pushes the water through the chamber like a piston as it passes through. The water particles move with the jet tip and compress to very high pressures, such as 4-5 GPa in front of the jet, as shown in Figure 6.9 middle and lower pictures for both  $t_w=5$  mm and 15 mm sidewall chambers. Thus, the jet leaves the chamber with an explosion of the bottom cap due to compressed water at extreme pressure. After the explosion of the bottom cap, pressure relief causes some portion of the jet tip, with a high velocity, to shatter into small pieces and to scatter in the radial direction (Figure 6.12 middle and lower pictures). It causes material loss from the fastest and the most effective part of the jet. This effect becomes much more apparent when the sidewall thickness ( $t_w$ ) of the 10 mm diameter chamber is increased to 15 mm (Figure 6.12

lower picture). These scattered jet particles hit the upper surface of the witness target. Their marks on the upper surfaces can be seen in Figure 6.6 and Figure 6.11 LH side. Copper jet material is spread to a relatively larger surface, regardless of the sidewall thickness. It creates larger dents than the other diameters on the upper surface of the witness plates, as shown in Figure 6.3 and Figure 6.4 LH side specimens. Figure 6.11 shows two chambers in Figure 6.4 LH side and the difference of their jet exit holes closer from two angles. The case for  $D=10$  mm,  $t_w=15$  mm is shown on the LH side in each picture, whereas  $D=20$  mm is shown on the RH side. For the  $D=10$  mm case, the jet punches quite a large hole in the bottom cap during the jet's exit due to the high pressure created at the jet tip. However, when  $D=20$  mm, the bottom cap keeps its shape for a while. Thus, pressure wave reflections from the bottom cap and then the sidewall causes additional particulations when the jet leaves the chamber and starts penetrating the target  $36\mu\text{s}$  after the detonation starts, as shown in Figure 6.13. As a result, the particulations spread to a longer part of the jet when  $D=20$  mm.

While the jet passes through the chamber, the pressure wave created in the water travels to the side of the chamber. When  $D=10$  mm and sidewall thickness  $t_w=15$  mm, it reflects earlier, which causes particulations at the portions closer to the tip (Figure 6.9, Figure 6.10 red circles in the lower pictures –Figure 6.10 is the same as Figure 6.9, high pressure zones at the jet tip are masked to make pressure wave reflections visible-, and Figure 6.13 lower picture). The reflected pressure levels are above 1 GPa, higher than  $D=10, 20$  mm cases with  $t_w=5$  mm sidewall thickness (0.4-0.5 GPa) (Figure 6.9, Figure 6.10 red circles in the upper and middle picture).

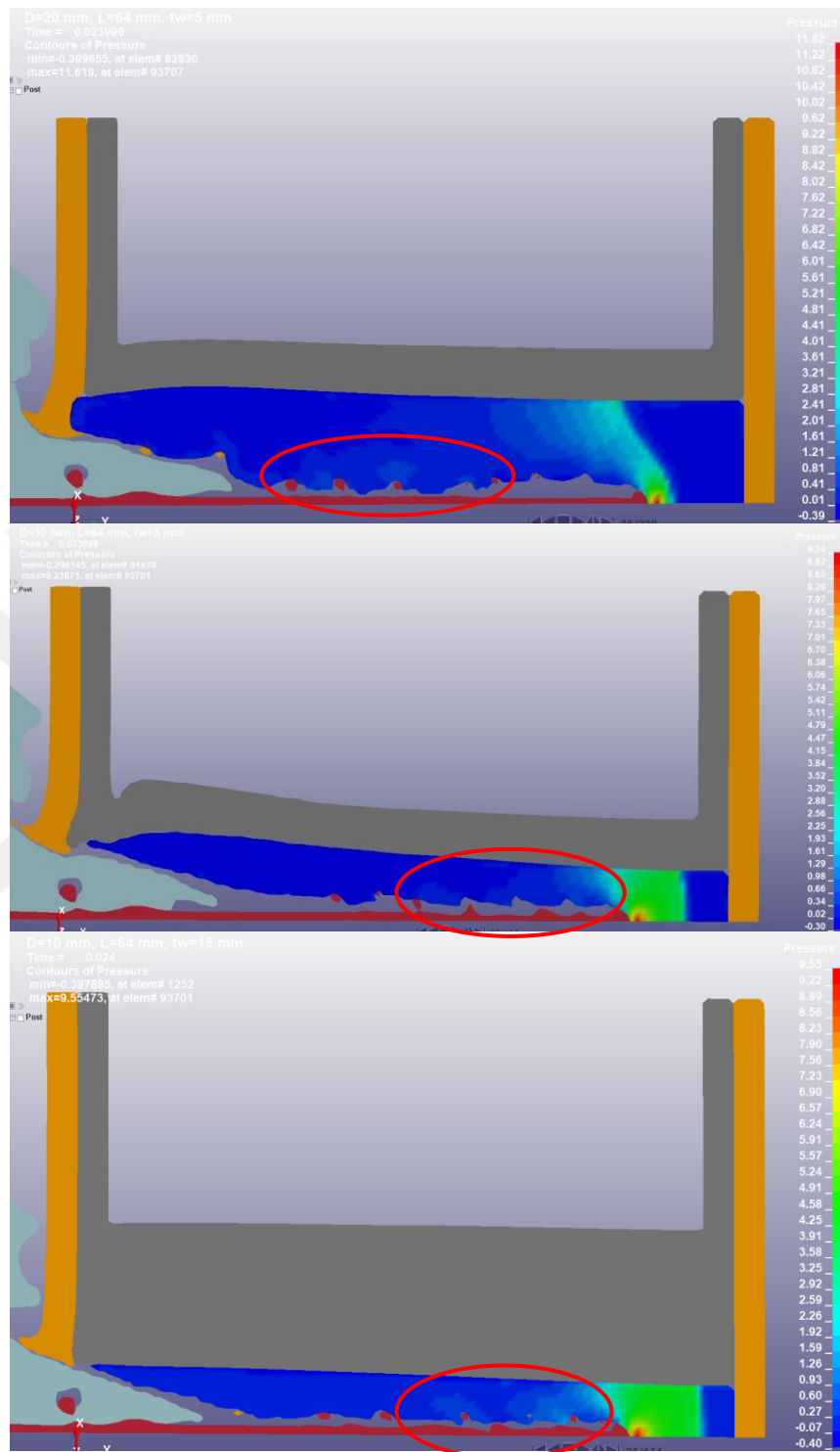


Figure 6.9 The Difference of Pressure Distributions in Water between 20 mm (Upper Figure) and 10 mm (Middle and Lower Figure) Diameter Chambers at  $t=24\mu\text{s}$

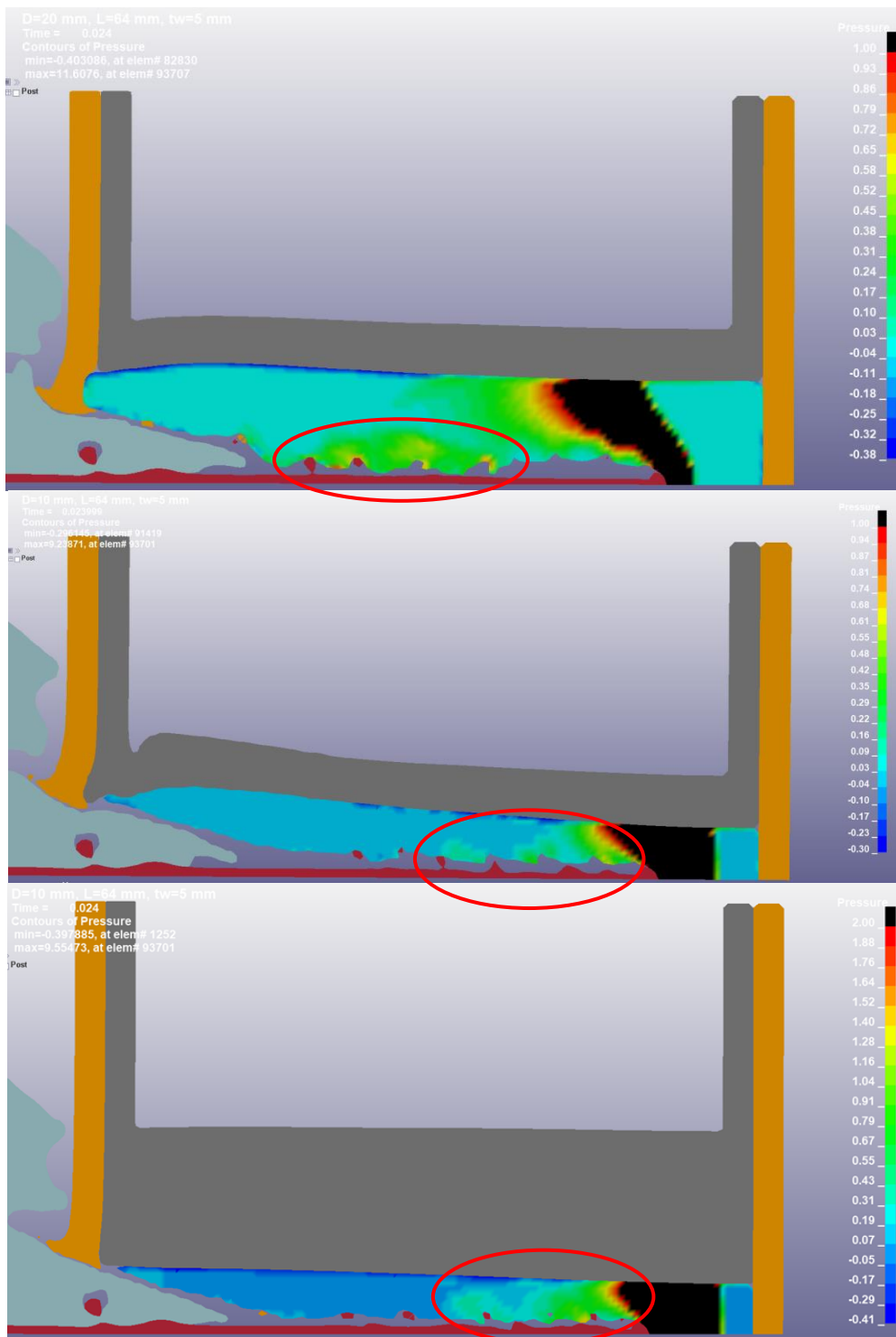
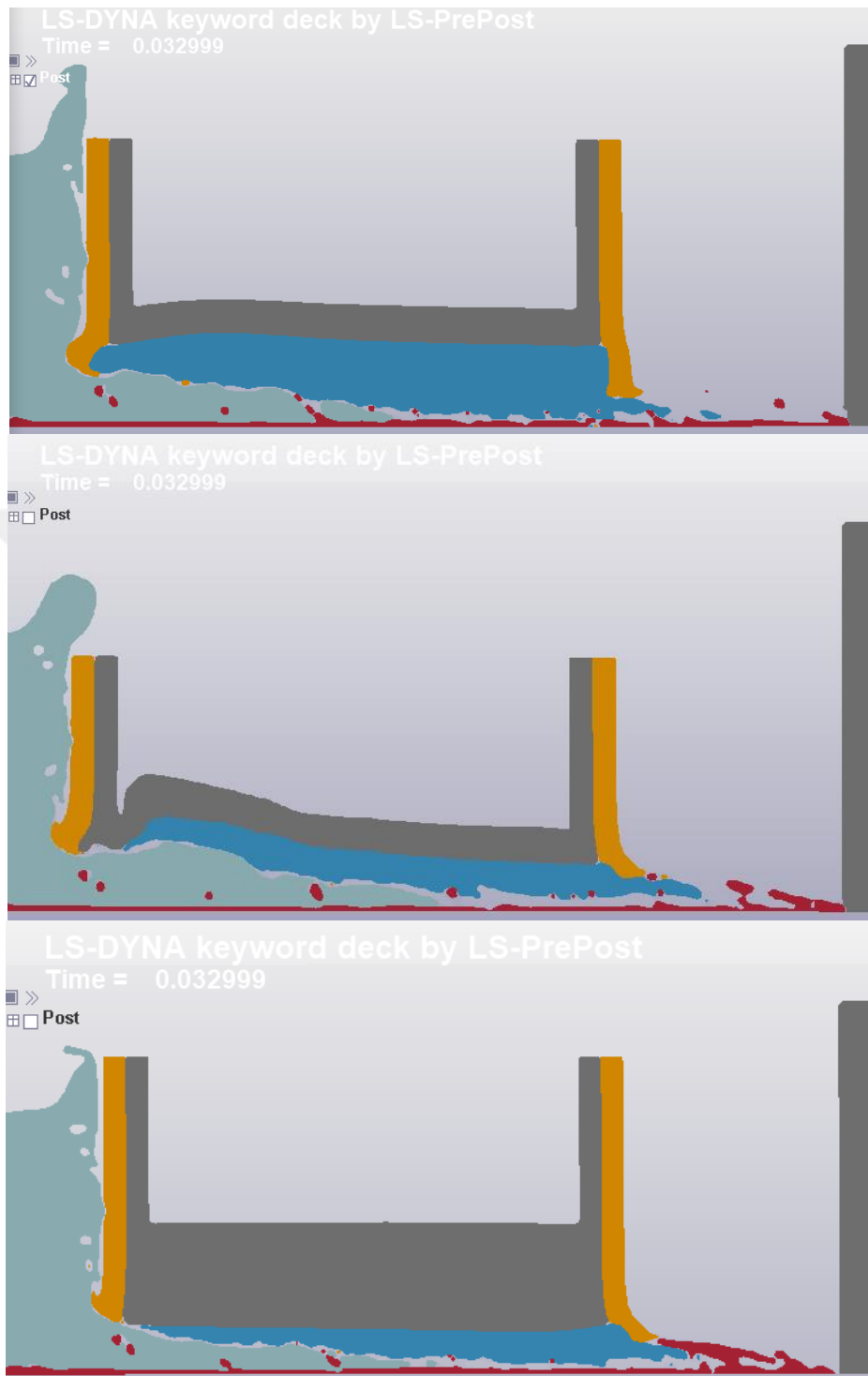


Figure 6.10 The Difference of Pressure Distributions in Water between 20 mm (Upper Figure) and 10 mm (Middle and Lower Figure) Diameter Chambers at  $t=24\mu\text{s}$  (Same as Figure 6.9. However, High Pressure Regions are Masked)



Figure 6.11 The Difference of Exit Holes between  $D=10$  mm,  $t_w=15$  mm (LH side Specimen in Each Picture) and  $D=20$  mm,  $t_w=5$  mm (RH Side Specimen in Each Picture) Diameter Chambers from Two Different Angles



■: Detonation products, 
 ■: Casing, 
 ■: Copper liner, 
 ■: Upper, lower caps, 
 ■: Chamber, target

Figure 6.12 The Difference of Jet Tip Scatter after Leaving 20 mm (Upper Figure ) and 10 mm (Middle and Lower Figure) Diameter Chambers at  $t=33\mu\text{s}$

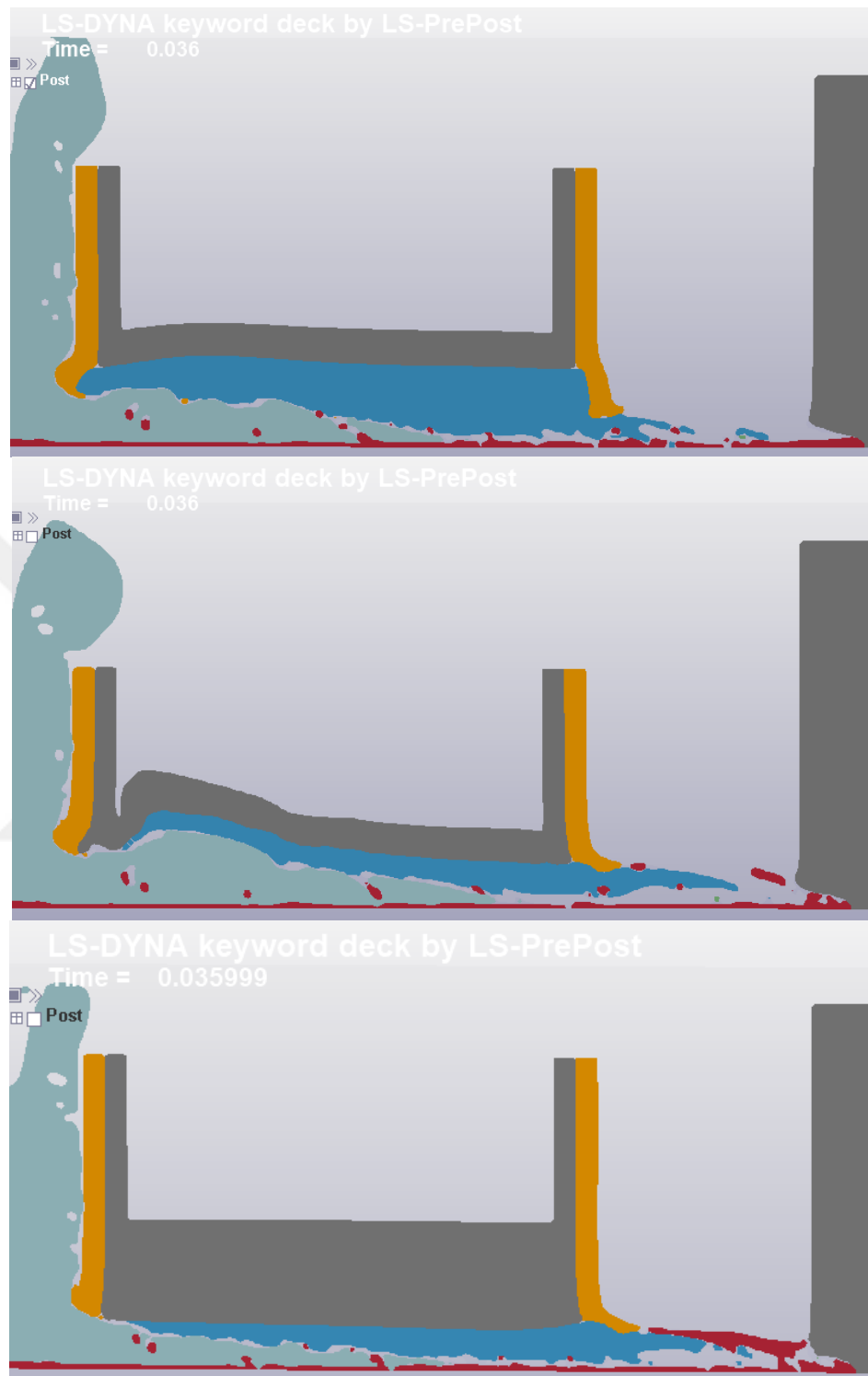


Figure 6.13 The Difference of Jet Particulation after Leaving 10 mm (Middle and Lower Figure ) and 20 mm (Upper Figure) Diameter Chambers at  $t=36\mu s$

## 6.2 Effect of Chamber Length (L) on Depth of Penetration

Figure 6.14 shows the depth of penetration in witness targets with respect to different lengths of water-filled chambers when the other parameters are kept constant. The test parts are shown in Figure 6.15. The cases of the water-free chamber and without chamber (Figure 5.2) are also shown in the same graph for comparison. Similar to the diameter tests, the test results (DOP) are determined by facing the witness target on a lathe from the bottom surface (opposite the shot surface). The machining stops when the copper liner or the hole is reached. Figure 6.16 shows the SC jet penetrated test setups with water-filled chambers that have different lengths, however, with a standard diameter of 20 mm and sidewall thicknesses of 5 mm. The remaining heights of the witness plates indicate the penetration of the shaped charge jet into these targets after passing through the water-filled chambers above the witness plates.

In Figure 6.14, the simulations with a water-filled chamber show that the increase in the chamber length reduces the depth of penetration between 32 mm and 64 mm, as expected. However, an increase in chamber length between 64 mm and 88 mm does not reduce DOP since the lower cap is very close to the witness target (5 mm gap). An enough distance between the chamber and the witness target is required for the jet to particulate after leaving the chamber. Thus, it is harder for the jet that is leaving 88 mm long chamber to particulate, as shown in Figure 6.17, which increases the resultant depth of penetration on the target compared to 64 mm long chamber.

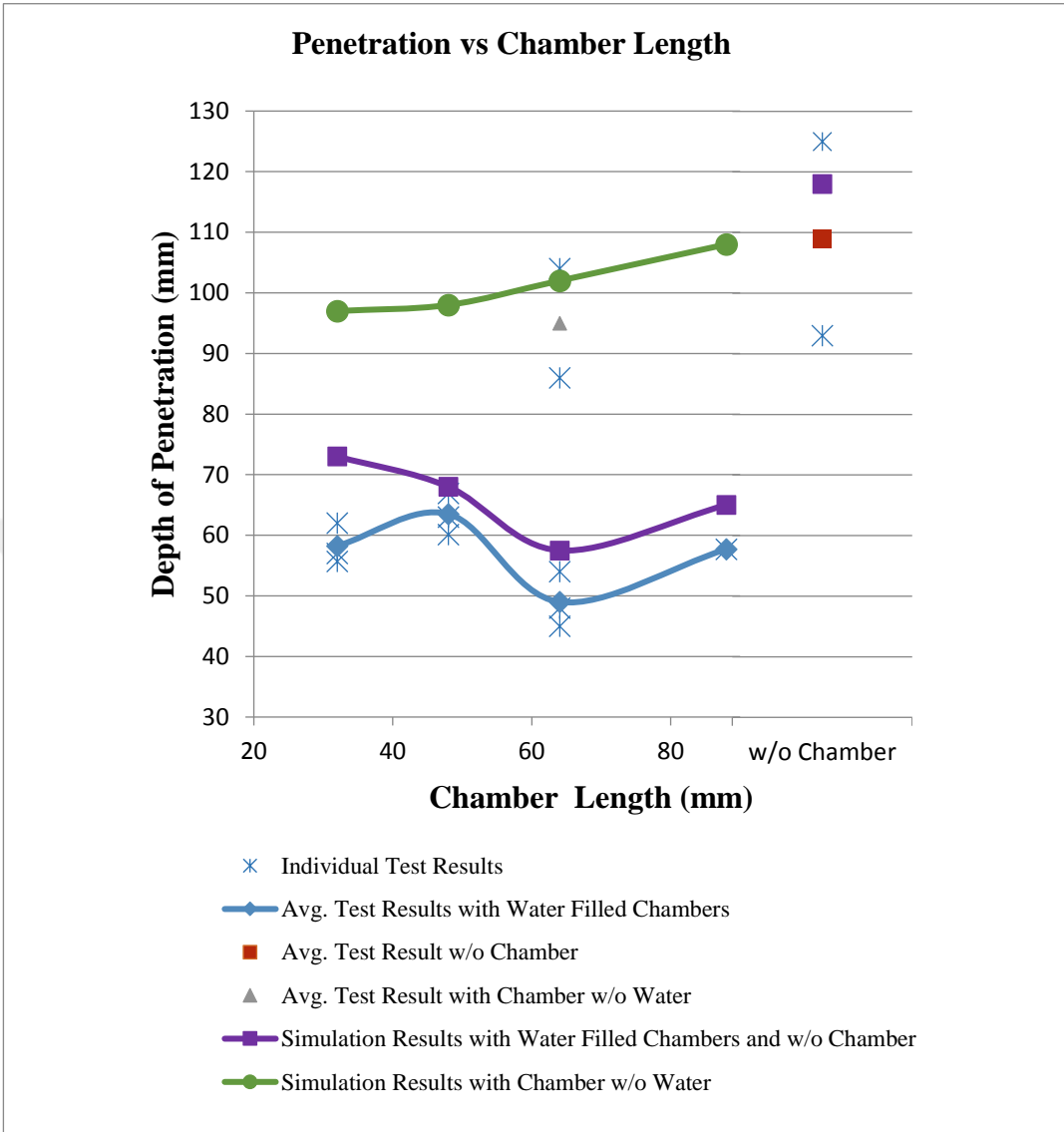


Figure 6.14 The Depth of Penetration vs Length when the Diameter is 20 mm and Sidewall Thickness is 5 mm



Figure 6.15 Test Setups with Different Length Chambers; 32 mm, 48 mm and 88 mm from Left to Right, Respectively with a Standard 5 mm Sidewall Thickness and  $\text{Ø}20$  mm Diameter

The increase in length of the water-free chamber reduces its protection (or increases the DOP), as shown in Figure 6.14 with the green graph, since the gap reduces between the witness plate and the chamber bottom plate. When this gap becomes larger (the chamber becomes shorter), the shattered pieces of the jet, after it penetrates through the bottom cap, scatter to a wider area on the witness plate. Thus, the jet's energy is dissipated, causing a reduction in DOP.



Figure 6.16 Test Results with Different Length Chambers; 32 mm, 48 mm, 64 mm and 88 mm, the DOP of the Witness Targets are 57 mm, 63 mm, 45 mm, 57,7 mm from Left to Right, Respectively

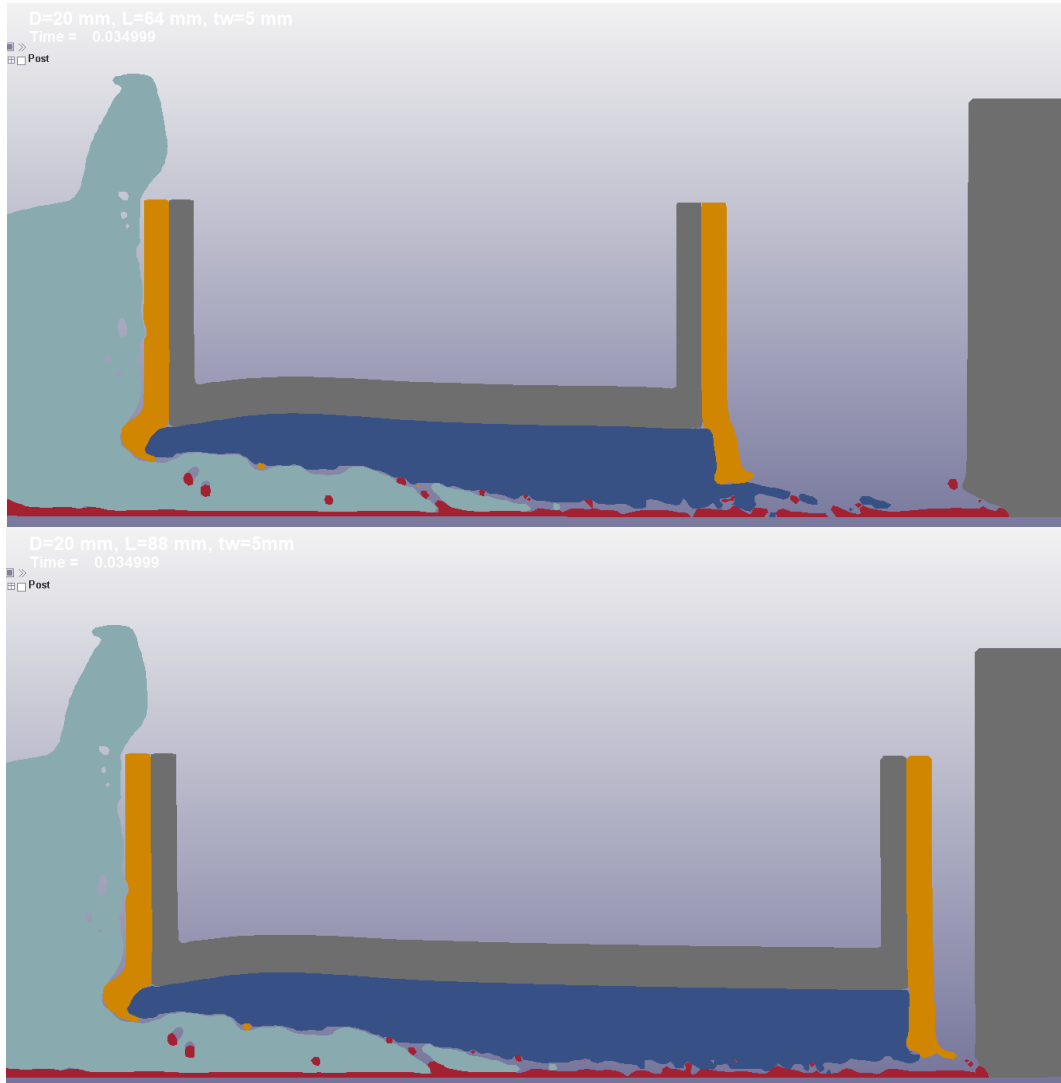


Figure 6.17 The Jet that is Leaving the Chamber of Different Lengths, L= 64 mm and 88 mm at  $t=35\mu\text{s}$

At 32 mm length, the difference between average test and simulation results (59 and 73 mm, respectively) of water-filled chambers is relatively larger than other chamber lengths. This large deviation between the simulation and test results is likely due to a strong interaction between geometric inaccuracies of the test setup and the gap between the chamber and the witness plate. The 32 mm long chamber has the largest distance to the witness plate. A very tiny non-concentricity between the munition and the chamber causes the wave reflections not to return to the jet

with a perfect balance as it is simulated. That imbalance and the large gap between the chamber and the witness plate may be causing the jet particles to spread around more and also causing the DOP to be less than 48 mm long chamber.

### 6.3 Effect of Sidewall Thickness ( $t_w$ ) on Depth of Penetration

Table 6.3 Effect of Sidewall Thickness on Penetration Depth when the Diameter (D) is 20 mm, and the Chamber Length (L) is 64 mm

	Sidewall Thickness ( $t_w$ ) [mm]						7,5	10
	1	3	5					
<b>Test Results</b> (Diameter 20 mm, Length 64 mm)	83	68	Test I	Test II	Test III	Avg.	42.8	43
			45	48	54	49		
<b>Simulation Results</b>	72	65	57.5				58	58

Figure 6.18 shows the depth of penetration in witness targets with respect to different sidewall thicknesses of water-filled chambers when the other parameters are kept constant. The test setups are shown in Figure 6.19. Figure 6.20 below shows the SC jet penetrated test setups with water-filled chambers that have different sidewall thicknesses, however, with the same length and internal diameter, 64 mm and 20 mm, respectively. The remaining heights of the witness plates indicate the penetration of the shaped charge jet into these targets after penetrating the chamber above the witness plate.

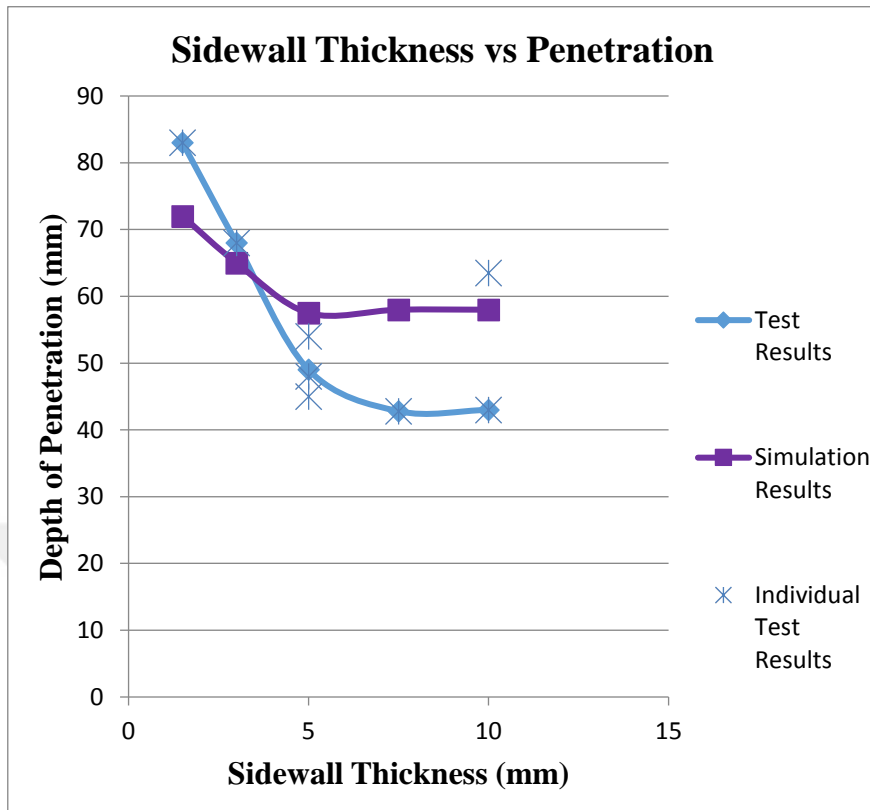


Figure 6.18 The Depth of Penetration vs Sidewall Thickness (D=20 mm and L=64 mm)



Figure 6.19 Test Setups with Different Sidewall Thickness Chambers; 1.5, 3, 7.5, and 10 mm from Left to Right, Respectively with a Standard 64 mm Length and Ø20 mm Diameter



Figure 6.20 Test Results with Different Sidewall Thickness Chambers; 1.5, 3, 5, 7.5, and 10 mm, the DOP of the Witness Targets are 83, 68, 54, 42.8, and 43 mm from Left to Right, Respectively

An increase in the sidewall thickness from 1.5 mm to 5 mm causes a reduction in the penetration depth, as shown in Figure 6.18. As the wall thickness increases, the incoming pressure waves cause less plastic deformation at the chamber walls. Therefore, a smaller portion of the energy is absorbed by the chamber sidewalls. Therefore, it reflects more energy back to the jet. However, the thickness has no remarkable effect when it is higher than 5 mm, which shows that 5 mm thickness is able to reflect enough amount of energy for the maximum possible particulation, so the increase in thickness above this value has no remarkable effect on the result.

The size of the high-pressure areas indicated with green zones ( $>400$  MPa) in Figure 6.21 is larger when the wall is thicker. These results show that the reflected amount of energy from the walls is higher when  $t=5$  mm compared to  $t=1.5$  and 3 mm. It causes more particulations when the jet leaves the chamber, as shown in Figure 6.22.

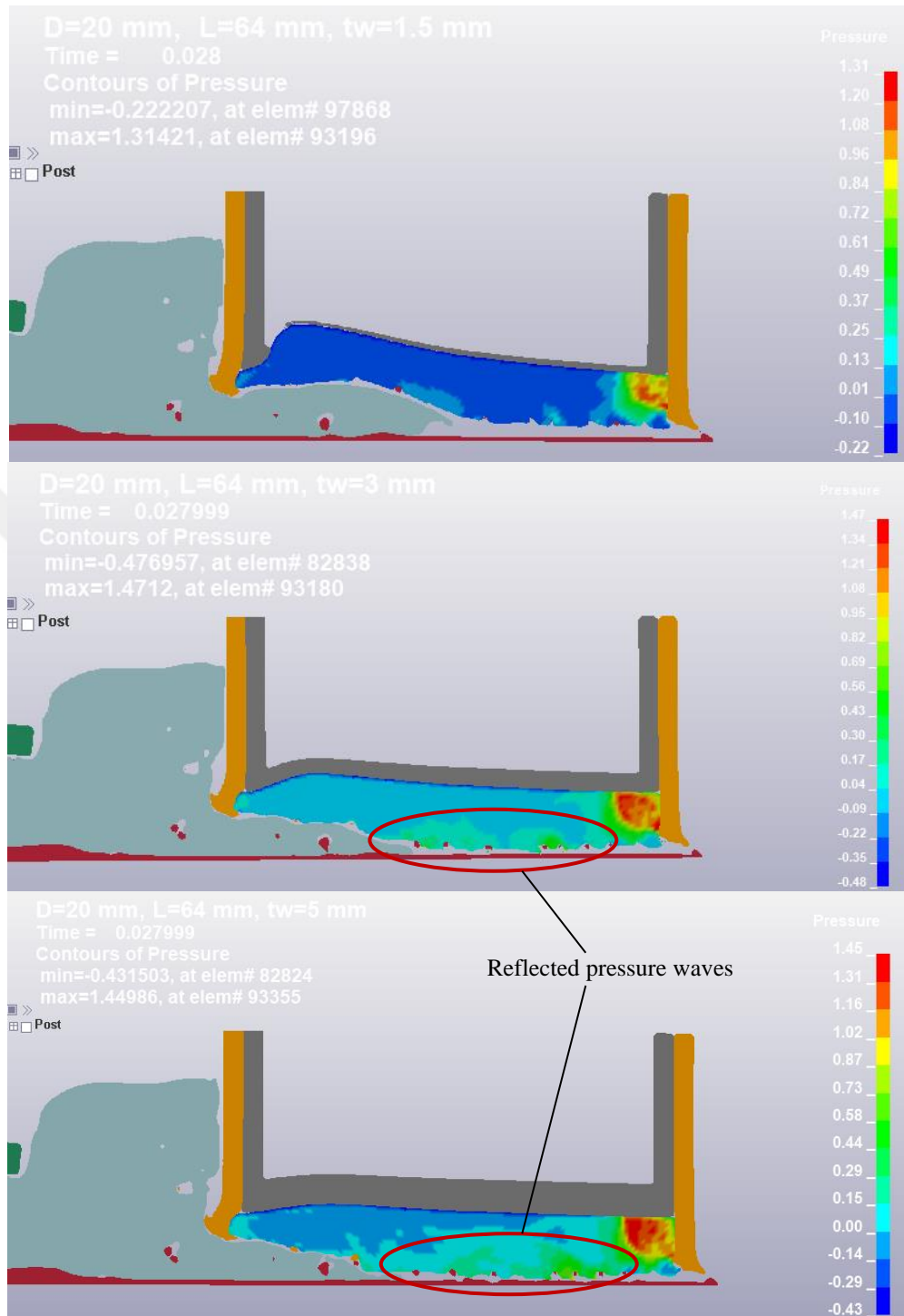


Figure 6.21 The Difference of Pressure Distributions (GPa) in Water between 1.5 mm (Upper Figure), 3 mm (Middle Figure), and 5 mm (Lower Figure) Sidewall Thicknesses at  $t=28\mu\text{s}$  ( $D=20$  mm and  $L=64$  mm)

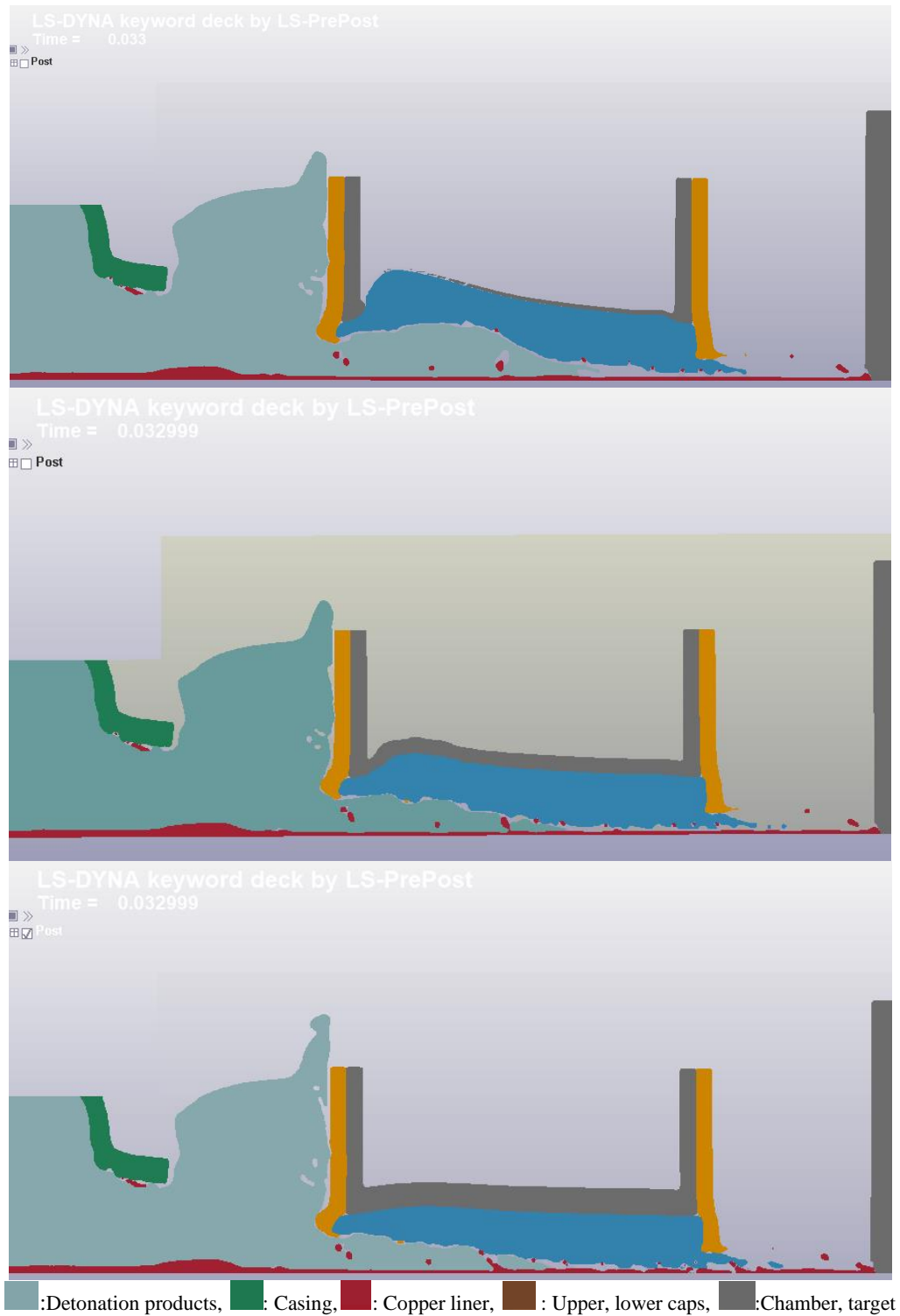


Figure 6.22 The Difference of Jet Particulation and Disturbances between 1.5, 3 and 5 mm Sidewall Thicknesses at  $t=33\mu\text{s}$  ( $D=20\text{ mm}$  and  $L=64\text{ mm}$ )

## CHAPTER 7

### CONCLUSIONS

#### 7.1 Summary and Conclusions

This thesis evaluates the protective capability of the water-filled cylindrical chamber made of 4340 steel with different diameters, lengths, and sidewall thicknesses against M85-shaped charge ammunition. The effects of these parameters on the penetration depth in the 4340 steel witness plate placed behind this chamber are investigated by conducting numerical FEM analysis and tests for the critical parameters.

The shaped charge jet is formed by the collapse of the conical copper liner with the detonation of the explosive with a wave from the tip of the cone to the bottom. The nature of this collapse process causes a velocity gradient within the jet from the tip to the tail. This velocity gradient results in the jet stretching and eventually particulate, an important phenomenon affecting its penetration capability. The liquid media can transmit the energy to the chamber side and bottom walls by pressure waves. The reflection of these pressure waves causes disturbances and particulations when radial pressure is applied to the jet. Within the scope of this thesis, the main aim is to observe how the different chamber parameters affect these particulations and the resultant DOP on the witness plate.

The numerical FEM simulations are carried out with 2D Multi-Material ALE algorithm, which usually gives consistent results with the tests. This verifies that the method is convenient to use with the shape charge jet impact with a liquid media such as water, liquid-solid interactions, and the behavior of ductile materials under hypervelocity impact, such as 4340 steel and OFHC copper, as also claimed by Wu et al., 2019 [32].

The effect of the diameter is investigated between 10 mm and 70 mm when the chamber length and sidewall thickness are kept constant, 64 mm and 5 mm, respectively. The optimum value for the chamber diameter to minimize the depth of penetration is 20 mm. When the diameter increases from 20 to 50 mm, the effect of the pressure wave reflections in the chamber diminishes gradually since the jet's affected regions from pressure wave reflections shift towards the tail of the jet. Thus, the disturbances and particulations on the jet occur in relatively lower velocity regions, whereas higher velocity regions keep their integrity. The DOP remains constant when the chamber diameter is greater than 50 mm since it takes such a long time for the pressure waves to reflect and return to the jet. All the effective part of the jet hits the target without any disturbance or particulations at these diameters.

With small diameters such as 10 mm, there is too little gap around the jet for the water to flow to the back side of the jet tip. Thus, the water particles move with the jet tip and compress to high pressures, around 4-5 GPa. This extreme pressure causes failure of the 5 mm thick chamber sidewalls. Thus, another test was also done with 15 mm sidewalls of the same diameter and length. The highly pressurized water at the jet tip causes the bottom cap to open with an explosion when the jet leaves the chamber. This pressure relief causes some jet particles at the tip to scatter in the radial direction. The hole is so large that the bottom cap can not reflect any pressure waves to the sidewalls and then to the jet as a 20 mm diameter chamber. Thus, the particulations occur only at a small region close to the tip and can not spread to the wider region as done in a 20 mm diameter chamber. Thus, the resultant DOP is higher than those for 20 mm diameter in both tests and simulations, even with a very high thickness.

At small diameters, such as 10 and 20 mm, the test results tend to be lower than the simulation results. This deviation enlarges up to 15% at 20 mm diameter and is thought to occur due to very tiny non-concentricity (less than 1 mm) between the munition and chamber, which is caused by geometric inaccuracies of the test setup.

While the jet is passing through the chamber, the pressure wave reflections are not returning back to the jet with a perfect balance as it is simulated. This imbalance is causing the jet material to spread sideways and causing the DOP to be lower than expected from simulations.

The effect of chamber length is investigated between 32 mm (approximately 1 x CD) and 88 mm, for which there remains only 5 mm gap to the witness plate; when the chamber diameter and sidewall thickness are kept constant, 20 mm and 5 mm, respectively. The simulations show that the increase in the chamber length reduces the depth of penetration between 32 mm and 64 mm, as expected. However, an increase in chamber length between 64 mm and 88 mm does not reduce DOP since the lower cap is very close to the witness target. A enough distance between the chamber and the witness target is required for the jet to particulate after leaving the chamber. Thus, it is harder for the jet that is leaving 88 mm long chamber to particulate, which increases the resultant depth of penetration on the target compared to the 64 mm long chamber.

The effect of sidewall thickness is also investigated between 1.5 mm to 10 mm. An increase in the sidewall thickness from 1.5 mm to 5 mm causes a reduction in the penetration depth. As the wall thickness increases, the incoming pressure waves cause less plastic deformation at the chamber walls. Therefore, a smaller portion of the energy is absorbed by the chamber sidewalls. Therefore, it reflects more energy back to the jet, causing more particulation. However, the thickness has no remarkable effect when it is higher than 5 mm, which shows that 5 mm thickness is able to reflect enough amount of energy for the maximum possible particulation, which can minimize the DOP.

## 7.2 Future Work

This thesis shows that the water-filled structures are a new type of armor that can be effective against SC munitions. It also provides some basic knowledge and experience to create a water-filled armor system against this type of munitions. However, there are a lot more studies/investigations to be done to develop an effective armor system in various operational conditions.

A small warhead diameter SC munition is used in this investigation due to the costs and availability of the test facility. However, the threats of armored vehicles are not limited to this kind of shaped charge. A larger munition such as LAW or RPG munitions may be studied.

This investigation is done in an axisymmetric condition. However, the munition does not have to be concentric and perpendicular to the chamber in an actual armor application. The cases considering the eccentricity and inclination angle of the munition to the chamber and the combination of both scenarios should be investigated to develop an armor. These cases can not be modeled with 2D, axisymmetric FEM algorithms. A 3D model is to be used. These cases may also be studied with combinations of different chamber diameters and lengths as well.

The different standoff distances between the chamber, munition, and the witness target and munition, as well as the different combinations of these parameters, may be studied to optimize the effectiveness of this kind of armor system. Furthermore, different liquid materials, chamber materials, and chamber shapes and their combination may also be evaluated.

## REFERENCES

- [1] Walters, W. P. & Zukas, J. A. 1989. Fundamentals of Shaped Charges, John Wiley & Sons, 2-6, 8, 45-48, 63, 64, 72-79, 118-124.
- [2] Bohanek, V., Dobrilović, M., Škrlec, V. 2014. The Efficiency of Linear Shaped Charges, Tehnicki vjesnik - Technical Gazette, 525.
- [3] Zhang, X., Xiong, W. 2022. Application of MESMs, Shock Compression and Chemical Reaction of Multifunctional Energetic Structural Materials, Elsevier Series in Mechanics of Advanced Materials, 194.
- [4] Saran, S., Ayışit, O., Yavuz, M. S. 2013. Experimental Investigations on Aluminum Shaped Charge Liners, The Scientific and Technological Research Council of Turkey - Defense Industries Research and Development Institute (TÜBİTAK SAGE), PK 16 Mamak, Ankara, 06261, Turkey , 480.
- [5] Xu, X., Ma, T., Nin J. 2016. The damage and failure mechanism of the concrete subjected to shaped charge loading, Engineering Failure Analysis, 742.
- [6] Kaplowitz, S. 1964. Technical Memorandum 1330 Description of LAW System and Control of Erosion in Rocket Motor, Defense Documentation Center for Scientific and Technical Information, Cameron Station Alexandria, Virginia, 13.
- [7] Baykara, T., Günay, V., Demirural, A. 2021. Structural Evolution and Microstructural Features of the Hydrodynamically Penetrating Copper Jet of a Shaped Charge, ASM International Journal of Materials Engineering and Performance, 1863.
- [8] Bohanek, V., Dobrilović, M., Škrlec, V. 2013. Application of Explosive Energy in Metalworking, Rudarsko-geološko-naftni zbornik Vol 26, 34 p.

- [9] Anastacio, A., Braithwaite, C. H., Kucera, J., Schmidová, E., Pachman, J. 2020. Shock Response of Polymer-bonded Copper Powder, Springer-Verlag GmbH Germany, *Shock Waves* (2020) 30, 373-384.
- [10] Jahsmann, H. E., Hopwood, K. M. 1999. Aircraft Canopy Fracture System, United States Patent, 4.
- [11] Walters, W. P., Flis, W. J., Chou, P. C. 1988. A Survey of Shaped Charge Jet Penetration Models, *Journal of Impact Engineering*, 308-321.
- [12] Zukas, J. A. 2004. Introduction to Hydrocodes (Studies in Applied Mechanics 49), Elsevier Science, 85, 95, 206, 235-237.
- [13] Souli, M., Ouahsine, A., Lewin, L. 2000. ALE Formulation for Fluid-Structure Interaction Problems, *Computer Methods in Applied Mechanics and Engineering*, 659-675.
- [14] Aquelet N., Souli M. 2008. 2D to 3D ALE Mapping, 10<sup>th</sup> International LS-DYNA Users Conference
- [15] Liu, G.R., Liu, M.B. 2003. Smoothed Particle Hydrodynamics, A Meshfree Particle Method-World Scientific Publishing Company, 11, 26, 27, 309, 310. 15-23 – 15- 31.
- [16] Wang, G., Cheng, H.D., Starzewski, M., Al-Ostaz, A., Radziszewski, P. 2010. Hybrid Lattice Particle Modelling Approach for Polymeric Materials Subject to High Strain Rate Loads, *Polymers*, 6.
- [17] Grady, D. 2017. Physics of Shock and Impact, Materials and Shock Response 2, IOP Publishing, 10-2.
- [18] Zhang, Z., Wang, L., Ming, F., Silberschmidt, V. V., Chen, H. 2017. Application of Smoothed Particle Hydrodynamics in Analysis of Shaped-

Charge Jet Penetration Caused by Underwater Explosion, Ocean Engineering, 179.

- [19] Steinberg, D. J. 1987. Spherical Explosions and the Equation of State of Water, Lawrence Livermore National Laboratory, 3.
- [20] Fredenburg, D.A., Aslam, T.D., Bennett, L.S. 2015. A Grüneisen Equation of State for TPX , Los Alamos National Laboratory, 1-3.
- [21] Wu, H., Hu, F. Fang, Q. 2019. A comparative study for the impact performance of shaped charge jet on UHPC targets, Defense Technology, 513, 514.
- [22] Otsuka, M., Matsui, Y., Murata, K., Kato, Y., Itoh, S., A study on Shock Wave Propagation Process in the Smooth Blasting Technique, 8<sup>th</sup> International LS-DYNA Users Conference, 7-9, 7-10.
- [23] Li, X., Yang, Y., LV, S. 2013. A Numerical Study on the Disturbance of Explosive Reactive Armors to Jet Penetration, Defence Technology, 68, 71.
- [24] Johnson, G. R., Cook, W. H. 1983. A Constitutive Model and Data for Metals Subjected to Large Strains, High Strain Rates and High Temperatures, Proceedings of the 7th International Symposium on Ballistics, The Hague, The Netherlands, 544.
- [25] Murugesan M., Jung D. W. 2019. Johnson Cook Material and Failure Model Parameters Estimation of AISI-1045 Medium Carbon Steel for Metal Forming Applications, MPDI Materials, 1-18.
- [26] Yadav, H.S., Bohra, B.M., Joshi, G.D., Sundaram S.G., Kamat, P.V. 1995. Study on Basic Mechanism of Reactive Armour, Defence Science Journal, 207, 208.

- [27] Trzcinski, W.A., Trebinski, R., Cudzilo, S. 2003. Study of the Reaction of model Reactive Armour to Jet Attack, Propellants, Explosives, Pyrotechnics, 90.
- [28] Guo, M., Zu, X., Shen, X., Huang, Z. 2019. Study on Liquid-filled Structure Target with Shaped Charge Vertical Penetration, Defense Technology, 863-866.
- [29] Zu, X.D., Huang, Z.X., Guan, Z.W., Yin, X.C., Zheng, Y.M. 2020. Influence of a Liquid-filled Compartment Structure on the Incoming Shaped Charge Jet Stability, Defense Technology, 3,4,10.
- [30] Gao, Z., Huang Z., Guo, M., Zu, X., Xiao, Q., Jia, X. 2016. Theoretical study of a diesel-filled airtight structure unit subjected to shaped charge jet impact. Propellants, Explos., Pyrotech, 65-68.
- [31] King, C., Dullum, O., Ostern, G. 2007. M85 An Analysis of Reliability, Norwegian People's Aid, 11, 24.
- [32] Wu, H., Hu, F., Fang, Q. 2019. A Comparative Study for the Impact Performance of Shaped Charge Jet on UHPC Targets, Defense Technology, 506-518.
- [33] Horta, L., G., Manson., H., Lyle K., H. 2009. A Computational Approach for Probabilistic Analysis of Water Impact Simulations, Langley Research Center, 1-15.
- [34] LS-DYNA Users Manual Volume II Material Models. 2008. LS-DYNA R11 Livermore Software Technology Corporation (LSTC), 2-126, 2-127.
- [35] Courant, R., Friedrichs, K., Lewy, H. 1928. Über die Partiellen Differenzgleichungen der Mathematischen Physik, Mathematische Annalen (in German), 32-74 .

- [36] Hallquist J. O. 2006. LS-DYNA Theory Manual. Livermore Software Technology Corporation (LSTC), 22.1-22.6.
- [37] Zhang, Z., Wang, L., Ming, F., Silberschmidt, V. V., Chen, H. 2017. Application of Smoothed Particle Hydrodynamics in Analysis of Shaped-Charge Jet Penetration Caused by Underwater Explosion, *Ocean Engineering*, 177-187.
- [38] Steinberg, D. J. 1987. Spherical Explosions and the Equation of State of Water, 3-7.
- [39] Vardhan, V., Pajjuri, K. 2017. Penetration Resistance of 4340 Steel/Polyurea Laminate (MSc. Thesis), 20.
- [40] Shi, J., Huang Z., Zu X., Xiao Q. 2022. Experimental and Numerical Investigation of Jet Performance Based on Johnson-Cook Model of Liner Material, *International Journal of Impact Engineering*, 5.
- [41] Liu, Y., Yin, J., Wang, Z., Zhang, X., Bi, G. 2020. The EFP Formation and Penetration Capability of Double Layer Shaped Charge with Wave Shaper, *MDPI*, 5.
- [42] Vovk, A., Sölter, J., Karpuschewski, B. 2020. Finite Element Simulations of the Material Loads and Residual Stresses in Milling utilizing the CEL Method, Elsevier, 541.
- [43] Johnson, G. R., Cook, W. H. 1985. Fracture Characteristics of Three Materials Subjected to Various Strains, Strain Rates, Temperatures, and Pressures, *Engineering Fracture Mechanics*, Vol. 21 No. 1, 32.



## APPENDICES

### A. The Photos of The Test Setups, Tested with Different Diameter Chambers



Figure A.1 Test Setups Tested with Chambers that have 10, 20, 35 (Above), 50, and 75 mm (Below) Diameter and 64 mm Length



Figure A.2 Test Setups Tested with 10 mm Diameter Chambers that have 5 mm (LH Side) and 15 mm (RH Side) Sidewall Thickness and 64 mm Length



Figure A.3 Test Setups Tested with 20 mm Diameter Chambers that have 5 mm Sidewall Thickness and 64 mm Length (Three Replicates)



Figure A.4 Test Setups Tested with 35 mm Diameter Chambers that have 5 mm Sidewall Thickness and 64 mm Length (Two Replicates)



Figure A.5 Test Setups Tested with 50 mm Diameter Chambers that have 5 mm Sidewall Thickness and 64 mm Length (Two Replicates)



Figure A.6 Test Setup Tested with 70 mm Diameter Chamber that has 5 mm Sidewall Thickness and 64 mm Length

**B. The Photos of The Test Setups, Tested with Different Length Chambers**



Figure B.1 Test Setups Tested with 32, 48 (Above), 64, and 88 mm (Below) Long Chambers that have 20 mm Diameter and 5 mm Sidewall Thickness



Figure B.2 Test Setups Tested with 32 mm Long Chambers that have 5 mm Sidewall Thickness and 20 mm Diameter (Three Replicates)



Figure B.3 Test Setups Tested with 48 mm Long Chambers that have 5 mm Sidewall Thickness and 20 mm Diameter (Three Replicates)

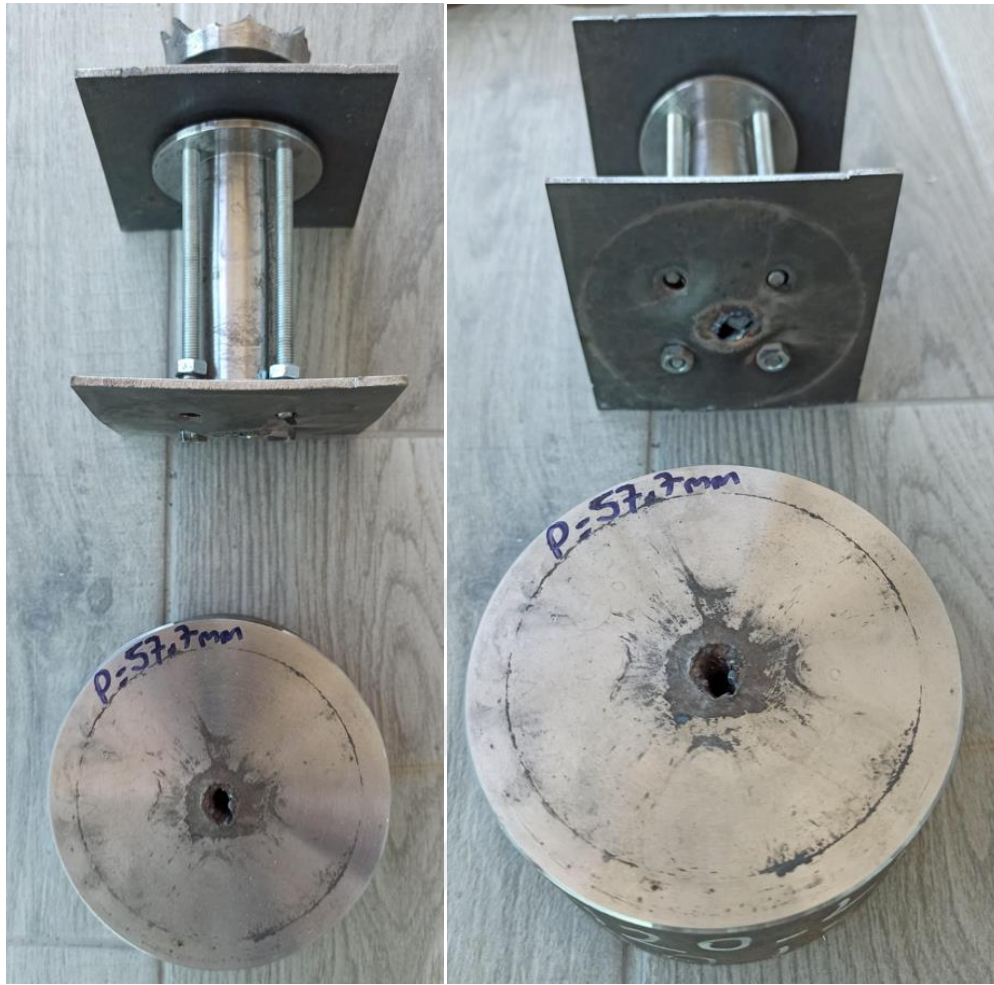


Figure B.4 Test Setup Tested with 88 mm Long Chamber that has 5 mm Sidewall Thickness and 20 mm Diameter

**C. The Photos of The Test Setups, Tested with Different Sidewall Thickness Chambers**



Figure C.1 Test Setups Tested with 1.5 (LH Side in Each Picture) and 3 mm (RH Side in Each Picture) Sidewall Thickness Chambers that have 20 mm Diameter and 64 mm Length

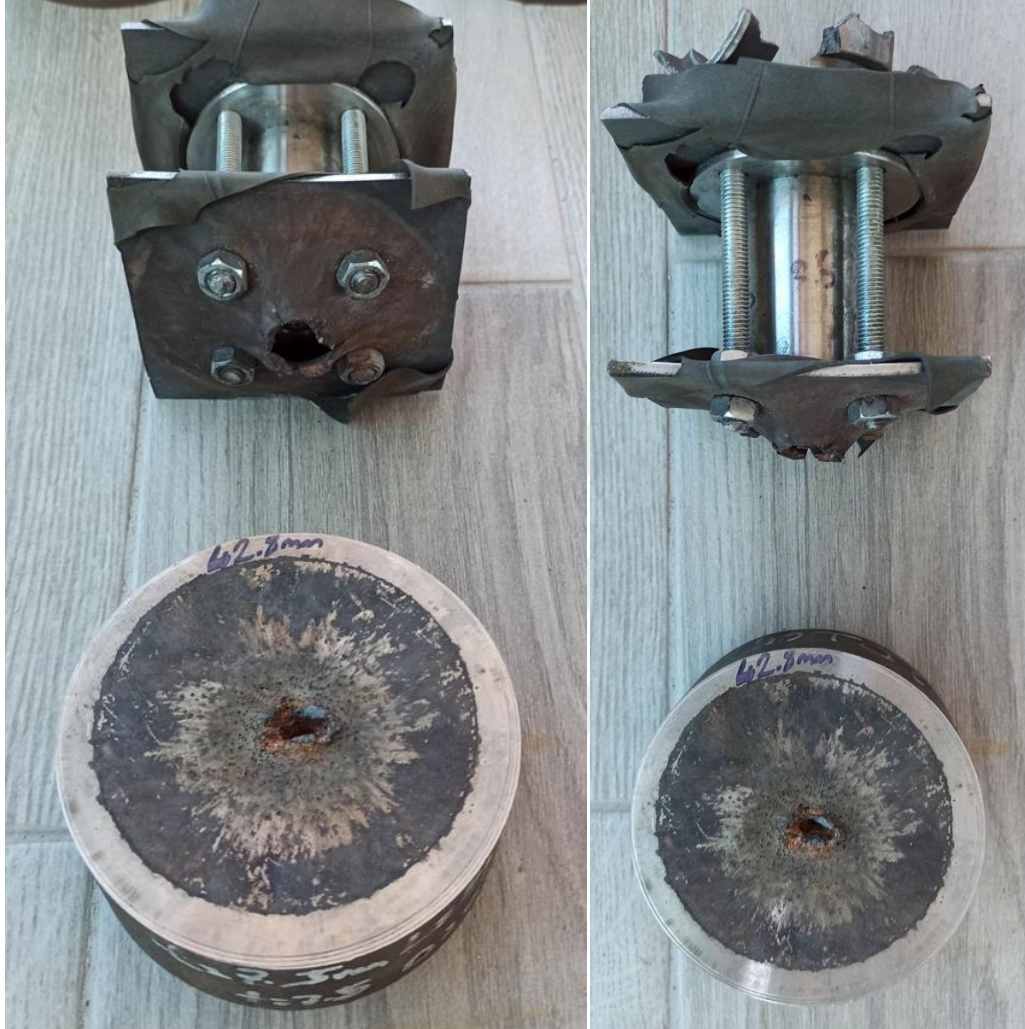


Figure C.2 Test Setup Tested with 7.5 mm Sidewall Thickness Chamber that has 20 mm Diameter and 64 mm Length



Figure C.3 Test Setups Tested with 10 mm Sidewall Thickness Chambers that have 20 mm Diameter and 64 mm Length (Two Replicates)

**D. The Photos of The Witness Targets, Tested with 64 mm Long Water-Free Chambers and without Chambers**



Figure D.1 Witness Targets Tested with 64 mm Long Water-Free Chambers



Figure D.2 Witness Targets Tested without Chamber

## CURRICULUM VITAE

Surname, Name: Gülyaşar, Fuat

### EDUCATION

<b>Degree</b>	<b>Institution</b>	<b>Year of Graduation</b>
MS	İTÜ Mechanical Engineering	2010
BS	İTÜ Mechanical Engineering	2008
High School	Ö.Ç. Bilfen Fen Lisesi	2004

### FOREIGN LANGUAGES

Advanced English, Intermediate German